BRNO UNIVERSITY OF TECHNOLOGY

VYSOKÉ UČENÍ TECHNICKÉ V BRNĚ

FACULTY OF MECHANICAL ENGINEERING

FAKULTA STROJNÍHO INŽENÝRSTVÍ

INSTITUTE OF PHYSICAL ENGINEERING

ÚSTAV FYZIKÁLNÍHO INŽENÝRSTVÍ

NOISE REDUCTION IN HIGH RESOLUTION COMPUTED TOMOGRAPHY DATA

REDUKCE ŠUMU V TOMOGRAFICKÝCH DATECH S VYSOKÝM ROZLIŠENÍM

MASTER'S THESIS

DIPLOMOVÁ PRÁCE

AUTHOR — Bc. Markéta Tkadlecová

AUTOR PRÁCE

SUPERVISOR — doc. Ing. Tomáš Zikmund, Ph.D.

VEDOUCÍ PRÁCE

BRNO 2022

BRNO UNIVERSITY OF TECHNOLOGY
FACULTY OF MECHANICAL ENGINEERING

Assignment Master's Thesis

Institut:	Institute of Physical Engineering
Student:	**Bc. Markéta Tkadlecová**
Degree programm:	Precise Mechanics and Optics
Branch:	no specialisation
Supervisor:	**doc. Ing. Tomáš Zikmund, Ph.D.**
Academic year:	2022/23

As provided for by the Act No. 111/98 Coll. on higher education institutions and the BUT Study and Examination Regulations, the director of the Institute hereby assigns the following topic of Master's Thesis:

Noise reduction in high resolution computed tomography data

Brief Description:

Noise is an inevitable part of computed tomography data and can be described as undesirable variations of detected signal that result in non–exact representation of the original scene. Noise presence in CT (Computed Tomography) data distorts acquired information and negatively affects data interpretation. Therefore, denoising has become important pre–processing step of CT data analysis. Until today many efforts have been done regarding noise reduction in field of medical CT but no complex denoising methodology and noise properties knowledge exist for high resolution computed tomography.

Master's Thesis goals:

• Get acquainted with methods of noise reduction in computed tomography data.
• Characterise the noise properties in high–resolution computed tomography data.
• Propose a suitable method for the noise reduction and implement it.
• Evaluate the noise reduction performance of the proposed method in high–resolution computed tomography according to selected image quality metrics.

Recommended bibliography:

HANSEN, Per Christian, Jakob JØRGENSEN a William R.B. LIONHEART. Computed Tomography: Algorithms, Insight, and Just Enough Theory. Philadelphia, PA: Society for Industrial and Applied Mathematics, 2021. ISBN 978-1-61197-666-3.

STOCK, Stuart R. MicroComputed Tomography: Methodology and Applications [online]. 2nd edition. Boca Raton: CRC Press, 2019 [cit. 2022-11-22]. ISBN 9780429186745. Dostupné z: https://doi.org/10.1201/9780429186745

KIM, Ji Hye, Yongjin CHANG a Jong Beom RA. Denoising of polychromatic CT images based on their own noise properties. Medical Physics [online]. 2016, 43(5), 2251-2260 [cit. 2022-11-22]. ISSN 00942405. Dostupné z: doi:10.1118/1.4945022

DING, Qiaoqiao, Yong LONG, Xiaoqun ZHANG a Jeffrey A. FESSLER. Modeling mixed Poisson-Gaussian noise in statistical image reconstruction for X-ray CT. Bamberg, Germany: The 4th International Conference on Image Formation in X-Ray Computed Tomography, 2016.

Deadline for submission Master's Thesis is given by the Schedule of the Academic year 2022/23

In Brno,

L. S.

prof. RNDr. Tomáš Šikola, CSc. Director of the Institute	doc. Ing. Jiří Hlinka, Ph.D. FME dean

Summary
Due to the complexity of the computed tomography (CT) data acquisition process, the noise in captured X-ray images is inevitable and can distort acquired information. Therefore, the noise should be controlled. Noise reduction in CT data has primarily been studied in low-dose medical CT, and there is little known about the properties of noise in sub-micron CT and its suppression. The denoising strategies can take place in the X-ray images, CT slices, or during the reconstruction process. This work primarily focuses on the reduction of noise in X-ray images and CT slices. The first step to finding a complex denoising methodology is to determine the distribution and mathematical model of the noise in the X-ray images. The model was established using bright field images taken under different exposure times. With the estimated model, the artificial noise in a phantom dataset could be simulated. Selected algorithms were tested in the X-ray images and the tomogram slices of the phantom and compared subjectively and objectively, through visual inspection and image quality metrics. The denoising strategies with the best outcomes were further evaluated on measured submicron CT datasets from the CT system Rigaku nano3DX, and their advantages, limitations, and possible usage were described.

Abstrakt
Vzhledem ke komplexnosti procesu akvizice dat výpočetní tomografie (CT) je šum v rentgenových snímcích nevyhnutelný a může vést ke zkreslení získané informace. Proto by měl být co nejvíce potlačen. Dosud se výzkum zaměřoval především na redukci šumu v CT datech u lékařských CT s nízkými dávkami, zatímco o šumu a jeho potlačení v CT datech s vysokým rozlišením je známo jen málo. Tato redukce může probíhat v oblasti rentgenových snímků, v průběhu tomografické rekonstrukce nebo v oblasti tomografických řezů. Tato práce se zabývá především redukcí šumu v rentgenových snímcích a tomografických řezech. Prvním krokem k nalezení komplexní metodiky je určení rozdělení a matematického modelu šumu přítomného v rentgenových snímcích. Tento model byl určen pomocí snímků bez přítomného vzorku, které byly pořízeny s různými expozičními časy. Pomocí stanoveného modelu byl simulován šum ve fantomovém datasetu. Vybrané algoritmy byly testovány na projekčních snímcích a tomografických řezech fantomu a porovnávány jak subjektivně, tak objektivně pomocí metrik kvality obrazu. Strategie s nejlepšími výsledky byly dále testovány na naměřených CT datech z CT systému Rigaku nano3DX s vysokým rozlišením a byly popsány jejich výhody, omezení a možnosti využití.

Keywords
X-ray radiation, computed tomography, tomographic reconstruction, projection domain, tomogram domain, denoising, noise

Klíčová slova
rentgenové záření, výpočetní tomografie, tomografická rekonstrukce, projekční doména, tomografická doména, redukce šumu, šum

TKADLECOVÁ, M. *Noise reduction in high resolution computed tomography data.* Brno University of Technology, Faculty of Mechanical Engineering, 2023. 83 s. Supervised by doc. Ing. Tomáš Zikmund, Ph.D.

Rozšířený abstrakt

Naše vnímání okolního světa je omezeno na rozsah vlnových délek elektromagnetického záření, které jsou naše oči schopny zachytit. Toto elektromagnetické záření nazýváme viditelným světlem. Vzhledem k úzkému spektru viditelného světla však získáváme o světě a objektech v něm pouze omezené a povrchové informace. Toto omezení lze jednoduše překonat pomocí kratších vlnových délek, které dokážou díky vyšší energii proniknout skrz materiál neprostupný pro lidský zrak, a tím přinést nové poznatky. Do této kategorie patří i rentgenové záření.

Rentgenové záření představovalo revoluční objev, jehož uplatnění se brzy rozšířilo do mnoha oborů. Na základě myšlenky, že se pomocí rentgenového záření dá zrekonstruovat celá vnitřní struktura objektu, vznikla technika výpočetní tomografie (anglicky computed tomography – CT). CT se rychle stalo populárním a efektivním nástrojem pro nedestruktivní zobrazování v mnoha různých odvětvích, od medicíny až po materiálové vědy. Díky této technice dokážeme zobrazit jak vnější, tak vnitřní struktury reálných 3D objektů na základě retgenových snímků zachycených ze sekvence úhlů. Tyto rentgenové snímky nazýváme projekcemi. Rekonstrukčním algoritmem jsme schopni z projekcí vypočítat tomografické řezy a následně zrekonstruovat celý objem objektu. Pomocí mikro a nano CT systémů lze získat snímky s vysokým rozlišením, které nám umožňují analyzovat strukturní změny, materiálové charakteristiky nebo odhalit vady, trhliny a póry, které se mohou v objektu vyskytnout v brzkých stádiích výrobního procesu. Tato analýza se hojně využívá ve výrobě mikroelektroniky, baterií nebo kompozitních materiálů.

Proces výpočetní tomografie od projekcí k finálnímu 3D zrekonstruovanému objektu je však velmi složitý a kvalitu výstupu může ovlivnit mnoho faktorů. Jeden z nejvýraznějších faktorů je šum. Šum může způsobit významné zkreslení získaných informací, nebo i snížení kvality a prostorového rozlišení rekonstruovaných řezů. Proto by měl být šum v procesu CT zobrazování co nejvíce potlačen. Do dnešního dne se mnoho autorů v odborných publikacích zabývalo redukcí šumu v CT datech, ale především ve spojitosti s medicínským CT při nízkých radiačních dávkách, a není mnoho známo o šumu v CT datech s vysokým rozlišením a o možnostech jeho redukce. Pro volbu vhodných metod redukce šumu je proto klíčové nejprve provést charakterizaci tohoto šumu a určit jeho rozdělení. Samotná redukce může být provedena ve třech stádiích – v oblasti projekcí, v průběhu tomografické rekonstrukce nebo v tomografických řezech po rekonstrukci. Hlavním cílem této práce je porovnat přístupy potlačení šumu, a to v projekčních datech a tomografických řezech, a navrhnout vhodnou metodiku.

Tato práce je rozdělena do několika kapitol. Kapitoly 1 a 2 jsou teoretické a dávají čtenáři vhled do problematiky výpočetní tomografie a šumu. Experimentální část práce začíná statistickou analýzou šumu v kapitole 3. Samotné testování algoritmů pro redukci šumu je popsáno v kapitole 4.

První kapitola poskytuje základní informace o rentgenovém záření a o jeho chování při průchodu vzorkem. Dále jsou stručně popsány zdroje rentgenového záření a detektory pro jeho zaznamenání, možnosti geometrie CT systému a princip tomografické rekonstrukce. Důraz v této kapitole je kladen na popsání aspektů v průběhu CT zobrazování, které mohou mít vliv na výsledný šum, a to jak negativní, tak pozitivní. Těchto aspektů je celá řada. Diskutovány jsou faktory ovlivňující počet detekovaných fotonů, faktory spojené se strategií v průběhu měření, vliv detektoru a samotné tomografické rekonstrukce. Počet detekovaných fotonů můžeme ovlivnit pomocí proudu a napětí zdroje, expozičního času

nebo filtrací spektra energií vycházejícího ze zdroje. Strategie měření zahrnuje zejména počet projekcí, průměrování projekčních snímků a pozici objektu při měření. Velký vliv na výsledný šum v rekonstrukčních řezech má i volba rekonstrukčního algoritmu.

Jelikož je zaznamenaný šum v projekčních datech kombinací všech vlivů (kromě tomografické rekonstrukce), jeho rozdělení je neznámé. Určením tohoto rozdělení a následně i modelu šumu v projekčních snímcích se věnuje kapitola 3. Pro statistickou analýzu byly použity projekční snímky bez přítomného vzorku zachycené CT systémem Rigaku nano3DX. Celkově bylo analyzováno devět souborů o 10 snímcích, kdy každý soubor byl naměřen při rozdílné expozici (1 s – 45 s). Z každého souboru byl vypočítán průměrný snímek, který se následně od souboru odečetl. Před určením průměrného snímku se ze souboru nejdříve musely eliminovat odlehlé hodnoty způsobené impulsním šumem. Pro detekci těchto pixelů byla použita metoda na základě percentilů. Po odečtení průměrného snímku zůstaly matice obsahující informaci pouze o přítomném šumu. Statistická analýza spočívala především ve vizuálním posouzení rozdělení šumových hodnot, kdy byly vykresleny Q-Q grafy a histogramy. Dále byly spočítány statistické momenty – střední hodnota, rozptyl a špičatost. Na základě této analýzy byl určen model šumu v projekčních datech, který byl následně popsán i teoreticky. Ověření tohoto modelu spočívalo v simulování šumu a jeho vizuálním porovnáním s reálným naměřeným šumem.

S využitím tohoto modelu bylo možné simulovat šum v projekcích umělého fantomu, který byl zvolen pro testování metod redukce šumu. Pro důkladné posouzení robustnosti metod byl šum simulován ve dvou intenzitách. Díky skutečnosti, že při testování na umělém fantomu máme k dispozici i zlatý standard – tedy výsledek, ke kterému se chceme přiblížit, je možné výsledky objektivně zhodnotit pomocí vhodných metrik kvality obrazu. Byly použity tři metriky, a to peak signal-to-noise ratio (PSNR), střední kvadratická odchylka (MSE) a Structural Similarity Index (SSIM). Celkově bylo testováno 7 metod pro redukci šumu na 2D snímcích a 4 metody pro 3D data. V první fázi byly metody použity na projekčních datech, kde je rozptyl simulovaného šumu známý z popsaného modelu. Výsledky metod byly porovnávány až po následné rekonstrukci, a to jak subjektivně, tak objektivně pomocí metrik. Dále byla hodnocena i kvalita automatické segmentace pomocí Diceova koeficientu podobnosti. Následně byly vybrané metody použity i na tomografických snímcích a proces vyhodnocení byl zopakován. Metody byly porovnány i na základě jejich výpočetního času. Po tomto testování byla provedena diskuze obou strategií redukce šumu.

Jako nejúčinnější přístupy byly vyhodnoceny použití metody BM3D na projekcích, metody BM4D na projekcích a metody BM4D na tomografických řezech. Jelikož jsou ale všechny tyto strategie časově náročné, byla k nim vybrána možnost rychlé redukce šumu, a to non-local means filtr jak na projekcích, tak v řezech. Všechny metody byly otestovány na třech reálných CT měřeních s vysokým rozlišením. Porovnání výsledků bylo provedeno jak subjektivně, tak objektivně pomocí dvou metrik kvality obrazu, a to prostřednictvím poměru signálu k šumu (signal-to-noise ratio SNR) a poměru kontrastu a signálu (contrast-to-noise ratio CNR). Byla porovnána i časová náročnost těchto metod. Výsledky byly popsány a následně proběhla diskuze jejich předností a omezení. Na základě této diskuze byly určeny optimální metodiky redukce šumu pro různá kritéria a vzorky.

Prohlašuji, že jsem diplomovou práci Redukce šumu v tomografických datech s vysokým rozlišením vypracovala samostatně pod vedením doc. Ing. Tomáše Zikmunda, Ph.D., s použitím materiálů uvedených v seznamu literatury.

I declare that I have elaborated my master's thesis Noise reduction in high resolution computed tomography data independently, under the supervision of doc. Ing. Tomáš Zikmund, Ph.D. All sources used or excerpted during the elaboration of this work are properly cited and listed in the references.

Bc. Markéta Tkadlecová

Na tomto místě bych ráda poděkovala mému vedoucímu práce doc. Ing. Tomášovi Zikmundovi, Ph.D. za jeho vedení, cenné rady, konstruktivní kritiku a podporu při vypracovávání této práce. Dále bych chtěla velmi poděkovat Ing. Janu Matulovi, Ing. Jakubovi Šalplachtovi, PhD. a Ing. Markovi Zemkovi za jejich čas, nápady a cenné rady. Ing. Janu Matulovi patří speciální dík za technickou podporu při psaní této práce. Dále bych chtěla poděkovat celému CTLabu za vytvoření příjemné atmosféry.
Speciální poděkování patří i mé rodině a blízkým, kteří mě podporovali v průběhu celého studia a i při psaní této práce. Bez Vás bych nebyla tam, kde jsem.

At this place, I would like to thank my thesis supervisor doc. Ing. Tomáš Zikmund, Ph.D. for his guidance, valuable advises, constructive criticism and support throughout the work on this thesis. I would also like to thank Ing. Jan Matula, Ing. Jakub Šalplachta, PhD., and Ing. Marek Zemek for their time, ideas and valuable advises. My sincere thanks go out to Ing. Jan Matula for providing technical support during the writing of this thesis. I am also grateful to the entire team at the CTLab for creating a welcoming environment. Special thanks go to my family and close ones, who have supported me throughout my studies and during the writing of this thesis. Without you, I would not be where I am today.

Bc. Markéta Tkadlecová

Contents

Introduction 3

1 X-ray computed tomography 5
1.1 Principle of measurement . . . 5
1.2 X-ray sources and detectors . . . 6
1.3 Scan geometries . . . 8
1.4 Tomographic reconstruction . . . 9
1.4.1 Analytic reconstruction algorithms . . . 9
1.4.2 Iterative reconstruction algorithms . . . 13
1.5 Aspects in the CT measurement affecting the noise . . . 15
1.5.1 Number of detected photons . . . 16
1.5.2 Measurement strategy . . . 17
1.5.3 Detector . . . 19
1.5.4 Tomographic reconstruction . . . 19

2 Noise in digital images and its reduction 21
2.1 Digital image . . . 21
2.2 Types of noise . . . 22
2.2.1 Gaussian noise . . . 22
2.2.2 Impulse noise . . . 23
2.2.3 Speckle noise . . . 23
2.2.4 Shot noise . . . 23
2.3 Denoising algorithms review . . . 24

3 Estimation of the noise model in the projection domain 28
3.1 Statistical analysis of noise in bright frames . . . 28
3.2 Theoretical model . . . 33

4 Noise reduction approaches in computed tomography 37
4.1 Introduction to selected denoising algorithms . . . 38
4.2 Software packages for tomographic reconstruction . . . 40
4.3 Metrics used for evaluation . . . 41
4.3.1 Full-reference metrics . . . 41
4.4 Phantom denoising . . . 43
4.4.1 Denoising in the projection domain . . . 44
4.4.2 Denoising in the tomogram domain . . . 50
4.4.3 Time duration . . . 54
4.4.4 Discussion of the phantom denoising results . . . 55
4.5 Measured dataset denoising . . . 57
4.5.1 Time duration . . . 64
4.5.2 Discussion of the results of measured datasets denoising . . . 64
4.6 Proposed denoising strategies . . . 65

Conclusion 67

List of abbreviations 75

A Statistical analysis of noise in bright frames with Mo target 79

B Selected parameters for denoising of simulated dataset 82

C Selected parameters for denoising of measured dataset 83

Introduction

As humans, our perception of the world is limited by the range of wavelengths of electromagnetic radiation that our eyes can detect. This range is called visible light. However, the narrow spectrum of visible light provides only a partial and superficial picture of the world. One way to overcome these limitations is to use radiation with shorter wavelengths and higher energies. These types of electromagnetic radiation can penetrate materials that are not transparent to our eyes and reveal new information about the object. X-rays are an important representative of this group.

X-ray radiation discovered by Wilhelm Conrad Roentgen in 1895 was a revolutionary breakthrough and instantly changed the fields of physics and medicine [1]. Based on the motivation, that the whole internal structure of an object can be reconstructed using X-rays, computed tomography (CT) was developed. Since its invention, the CT become a very popular and highly successful non-destructive diagnostic tool in many fields – from medicine to material sciences. It is a powerful technique in which the external, as well as the internal structure of a 3D object is reconstructed based on its X-ray images captured from a sequence of angles. These X-ray images are called projections. By using the reconstruction algorithm to the projections, the cross-sectional images of the object can be calculated. Thanks to the micro CT and nano CT it is possible to produce high-resolution images and analyze structural changes, and material characteristics or reveal flaws, cracks, and pores present in the measured sample early in the production process. This analysis can be very useful for the manufacturing of microelectronics, batteries, and composite materials.

However, the process from projections to the final reconstructed volume is very complex and many influences can affect the quality of the outcome. One of the most serious influences is noise. Noise can cause significant distortions to the acquired information and downgrade the quality and spatial resolution of the reconstructed images. Therefore, effective noise reduction techniques play a crucial role in CT imaging. To this date, many papers have been focused on noise reduction in CT data, but mainly in connection with low-dose medical CT, and there is little known about the properties of noise in sub-micron CT and its suppression. That is why the analysis of noise characteristics and its distribution is crucial for understanding the noise and selecting suitable denoising methods. The denoising strategies can take place in the projections, reconstructed CT slices, or during the reconstruction process. This work aims to compare the denoising strategies in the projections and CT slices and design the optimal strategy for noise reduction.

This thesis is divided into several parts. In the first chapter, the principles of X-ray computed tomography and tomographic reconstruction are introduced. This chapter covers also a review of the factors that influence noise in CT measurements, both positively and negatively. The fundamentals of the digital image and the types of noise that can corrupt the digital image are described in the second chapter. Additionally, this chapter includes a comprehensive review of noise reduction algorithms and methods. To apply suitable denoising techniques to captured projection images, it is essential to determine the noise distribution in the projection domain. Chapter 3 deals with this problem. The focus is on the statistical analysis of the noise and noise model estimation. Finally, chapter 4 is devoted to the testing of selected denoising methods. First, noise reduction is performed on projections of a simulated phantom, where the noise is generated according to the noise model. Next, the same methods are tested on the CT slices and the outcomes are

compared using appropriate image quality metrics. Based on this comparison, the most promising methods are selected and tested on measured submicron CT datasets, and their advantages, limitations, and possible usage are described.

1. X-ray computed tomography

Non-destructive techniques are methods used for testing, inspecting, and evaluating the quality, integrity, and characteristics of materials, parts, and products. A large group of these techniques is based on X-ray imaging.

X-rays, like visible light, are a form of electromagnetic radiation that transports energy through space. This radiation can be defined by its energy E, that is proportional to its wavelength λ, such as [2]

$$E = \frac{hc}{\lambda} = h\nu, \tag{1.1}$$

where h is the Planck's constant, c is the speed of light and ν is the frequency of the radiation. The wavelengths of X-rays are in the range of a few picometers to a few nanometers – shorter than visible light. Hence, the energy is higher allowing them to penetrate the object and visualize its internal structure. When X-ray photons pass through matter, they can be absorbed, scattered, or transmitted depending on the photon's energy and the material's properties [2].

X-ray computed tomography (CT) is used to visualize the internal structure of an object in 3D including its density, shape, and material composition. It can detect internal defects such as cracks, porosity, voids, and inclusions that may not be visible from the outside. This makes it an essential tool for quality control and product development in a variety of industries.

1.1. Principle of measurement

Imaging using X-rays to visualize the internal structure of an object is called radiography. Because of their high energy, X-rays can easily penetrate an object. As the X-rays pass through a measured sample, they are absorbed or attenuated at different levels resulting in changes in the beam's intensity. The intensity I exiting the sample can be expressed with the *attenuation coefficient* μ [m^{-1}] as

$$I = I_0 e^{-\mu \Delta d}, \tag{1.2}$$

where I_0 is the entrance intensity of the beam generated by the source and Δd stands for the thickness of the material [2]. X-rays are attenuated exponentially. The attenuation coefficient μ determines, how easily the beam can penetrate the object and is specific for every material depending on its density. For example, the value of μ for air is nearly zero, so the entrance and detected intensity is unchanged. The equation (1.2) is known as the *Beer-Lambert law*, however, in this form, it is only valid for a uniform sample. When multiple materials (with different values of μ) are taken into account, the equation changes to

$$I = I_0 e^{-\int_0^{\Delta d} \mu(s)\,\mathrm{d}s}, \tag{1.3}$$

where s represents the beam direction [2]. By dividing the equation by I_0 and taking the negative logarithm, the attenuation coefficient in the exponent is isolated, and the equation (1.3) can be expressed as

$$p = -\ln\left(\frac{I}{I_0}\right) = \int_0^{\Delta d} \mu(s)\,\mathrm{d}s. \tag{1.4}$$

This equation determines the projection measurement p, which represents the absorption of the beam by the sample [2]. It is valid only for the assumption of the monoenergetic nature of the X-ray beam, which is rarely met in real life – an X-ray tube emits a rather broad spectrum of energies. In addition, the attenuation coefficient μ can vary with X-ray energy leading to beam hardening and related artifacts [2]. With polychromatic beam, spectral density j_0 and the energy spread of the X-ray spectra $\mathrm{d}E$ must be considered and the equation (1.4) changes to [3]

$$p = \int_0^{\Delta d} \mu(s)\,\mathrm{d}s = -\ln\left(\frac{\int_E j_0(E)\,\mathrm{e}^{-\int_0^{\Delta d}\mu(s)}\,\mathrm{d}E}{I_0}\right). \tag{1.5}$$

However, the fundamental problem behind the equations remains the same – to find the function p.

During the CT measurement, a series of projection images of an object is taken from different angles. The acquired projections define the space or representation known as the projection domain. Using a reconstruction algorithm to the set of projection images it is possible to reconstruct a stack of cross-sectional slices of the object [2]. The reconstructed slices define the tomogram domain and together create a 3D volume consisting of voxels – volume cubic elements, a 3D analogy of a pixel [4].

For a successful reconstruction with high quality, a large number of projection images is needed. The number can be theoretically determined from the Nyquist-Shannon sampling theorem – a unique reconstruction of an object can be obtained if the sampling frequency of the object is twice as high as the highest frequency of the object details. Generally, the number of projections should be in the same order as the number of pixels in the horizontal dimension of a single projection [5].

1.2. X-ray sources and detectors

X-ray source and detector are the core components of each CT system. They are positioned on each side of the scanner and in between there is a sample stage, where the sample is placed. Another crucial part of the whole system is the rotational mechanism. In industrial CT, the mechanism rotates the stage with the sample on it and the detector and source are static. The sample should be secured on the stage, so another movement besides rotation is minimized [4].

To provide the essential X-ray beam for the measurement, the X-ray source is needed. The principle of generating X-ray photons has stayed unchanged since its discovery in 1895. In every X-ray tube, there is usually the cathode – electron gun containing the heated filament, from where the electrons are emitting, and an anode providing a voltage difference for accelerating the electrons. A Wehnelt electrode and magnetic lenses are used for focusing the electron beam to a small spot on the target material. The shape and size of the spot can affect the quality of the measurement [2], [4].

X-ray photons are generated when the target is bombarded by high-speed electrons. The generation of X-ray photons in a typical tube is a very inefficient process – only about 1% of the input energy is used to produce photons, and the rest is changed to heat. The X-ray photons beam's intensity (flux) depends on the number of electrons hitting the target and on the target's atomic number. On the other hand, the beam's energy is influenced by the voltage difference between the cathode and anode. The target material (usually

Cu, Mo, or W) determines the shape of the radiation spectrum. Typical X-ray spectrum (see fig. 1.1) is consisting of the lines of characteristic radiation and Bremsstrahlung (also called braking radiation). The characteristic radiation is emitted in a process of deexcitation of electrons in the target's atoms. First, the accelerated electrons excite the electron in the inner shell and when the electron is deexcitated, it emits its energy and a photon of characteristic radiation. The Bremsstrahlung radiation is released when the incoming electrons are decelerated by the nucleus of the target's atoms. This radiation is continuous throughout the whole spectra [2], [4].

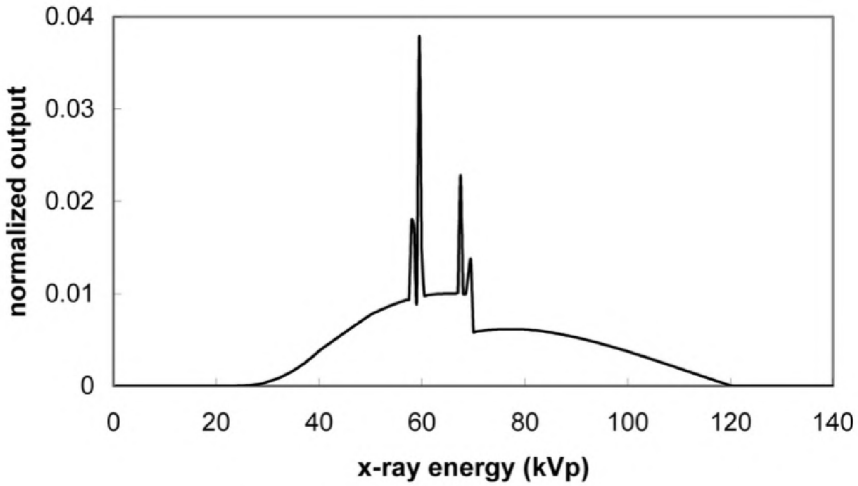

Figure 1.1: An example of a radiation spectrum of an X-ray tube at 120 kVp (peak kilovoltage). Image is taken from [2].

The detector is another key part of the CT system since it collects information about the sample's structure. It has a large impact on the final image quality – especially regarding the spatial resolution or the electronic noise. There are several ways, how to detect X-ray radiation. The two most common types of detectors are photon-counting detectors and scintillation-type detectors [6].

The scintillation-type detectors are used in a majority of all CT scanners. These detectors use the technology of indirect conversion – the X-ray photons are not detected directly, but a layer of scintillating material is used to change the photons into visible light. The light is then detected by a photodiode and converted into an electronic signal. This output signal is proportional to the total energy of the absorbed photons during the measurement period. Therefore, the detector does not provide information about the energy of individual photons. Modern detectors used in CT systems are usually 2D detectors – especially the CCD (charge-coupled device) or CMOS (complementary metal-oxide-semiconductor) technologies, but linear array detectors and 1D detectors exist and are beneficial in some special cases [4], [6]. The CCD and CMOS detectors differ mainly in the strategy of transporting the charge – in CMOS arrays, the charge of each pixel is handled independently and has its own transport line, whereas, in CCD detectors the charge of a row of pixels is transported through the same circuit and amplifier. CCD detectors have been widely used in many imaging applications, but in recent years, the popularity of CMOS sensors has increased mainly due to their lower power consumption, smaller size, and lower cost of production [7]. In the field of CT, CMOS detectors offer a significant advantage as they can achieve the same signal with lower exposure time,

enabling faster measurements. However, CMOS detectors are considered to be more sensitive to noise. It has been shown, that the CMOS detector has a higher noise level than the CCD sensor, given that an equivalent signal was detected [8]. This introduces another reason, why software-based noise reduction is an important topic and the solution to find methods for efficient reduction of noise independent on the detector needs to be implemented in order to improve the accuracy and quality of imaging data.

The photon-counting detectors (PCD) in CT systems are a quite new technology with great potential to improve their performance. The photon-counting detectors use direct conversion – every photon is counted individually and its energy is converted directly into the output signal. Every photon is absorbed in the semiconductor layer and generates an electric pulse. The strength of the pulse depends on the photon's energy. The photon-counting detectors showed some advantages over the scintillation-type detectors, especially when it comes to spatial resolution, reduction of electronic noise, or suppression of some artifacts. Despite their advantages, PCD detectors are not yet widely used in practice due to technical challenges that need to be overcome [6].

1.3. Scan geometries

The hardware of every CT scanner can be arranged in different ways determining the beam geometry. The choice of geometry depends on the specific application and the desired image quality and resolution. Each of the geometries, that are described in this section, has its advantages and disadvantages. The most common are parallel-beam, fan-beam, and cone-beam geometry [2].

When all the X-rays that form one projection are parallel to one another, the CT geometry is called parallel-beam (fig. 1.2 (a)). It is the simplest geometry. Parallel-beam geometry can be achieved by collimating the X-rays into a thin beam and detecting this thin beam to a single element on the detector. The beam needs to be moved in a linear motion to capture the whole projection. The advantage is that the scattered radiation is reduced, but the complex data acquisition results in long measurement times [9].

Fan-beam geometry uses a thin fan of X-rays. These rays are captured on a 1D detector array. The source is usually very small, ideally point-like. If the fan beam is wider than the measured sample, only rotation of the sample is performed. This leads to shorter measurement times. The detector elements can be arranged either in a line or in a circular arch with its center at the X-ray source (fig. 1.2 (b)) [9].

Cone beam geometry can be described as multiple fan-beam planes collecting the signal simultaneously (fig. 1.2 (c)). This approach needs a large two-dimensional planar detector in order to capture a 2D image. The advantage of cone-beam geometry is the fast measurement times, but the scattered radiation is not reduced. The fan beam planes have different incidence angles on the detector, which is a significant source of image artifacts [2].

When the beam is divergent from the source spot – in the case of the fan beam and cone beam – the effect of geometric magnification occurs. By this effect, the captured object can appear larger on the detector. In an ideal case, when the source can be approximated only with one point, the geometric magnification is defined as

$$M = \frac{|\mathrm{SD}|}{|\mathrm{SO}|}, \tag{1.6}$$

where |SD| stands for the distance between the source and detector and |SO| is the distance between the source and the measured object. In this case, a high magnification, therefore higher resolution, can be obtained either by a very low source-object distance |SO| or by a high value of |SD|. But in practice, the source's finite size introduces limits to this effect. Also, with a higher angle of the beam's cone, typical cone beam artifacts can occur [10].

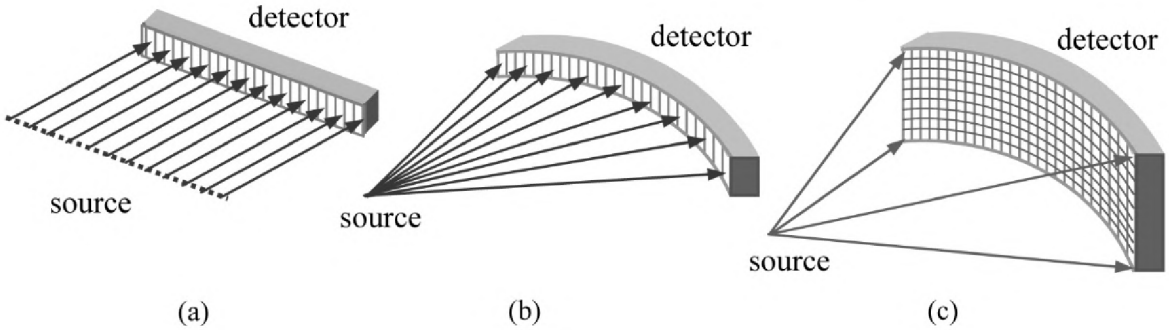

Figure 1.2: Illustration of different scan geometries: (a) parallel-beam geometry, (b) fan-beam geometry, (c) cone-beam geometry. Adapted from [2].

1.4. Tomographic reconstruction

Image reconstruction from projections is a mathematical process of producing an image from estimates of its line integrals. Let's consider a three-dimensional object $O(x, y, z)$. The object consists of n layers parallel to the plane (x, y) and perpendicular to the z axis. Each layer corresponds to one row of pixels on the detector and represents a tomographic slice of the object. The slice can be interpreted as a 2D function $f(x, y)$, representing the measured object's linear attenuation coefficients μ [5]. The goal of computed tomography is to reconstruct the slices, therefore the whole object, from its projections taken from a series of angles. The problem of CT reconstruction is a simple problem to formulate in theory, but the exact solution to this problem is still not known [11].

In this section, the two groups of algorithms will be discussed – analytic and iterative reconstruction methods. The analytic methods are based on mathematical models such as Fourier transform, Radon transform, and Fourier slice theorem. In contrast, iterative methods use the principle of linear algebra.

1.4.1. Analytic reconstruction algorithms

Radon transform and Fourier slice theorem

The mathematical basics for CT image reconstruction were formulated by J. Radon in 1917 [2]. He was the first to suggest a solution for the reconstruction of an object from its line integrals. Here, the theory behind analytical reconstructions based on his idea will be shortly discussed.

A line integral represents the integral of some object's characteristics along a line, for example, the attenuation of a ray passing through an object. A line integral may be

parametrized by the two spatial coordinates (x, y), but in the case of CT reconstruction it is more suitable to rewrite the line in coordinates (t, θ), such as

$$x \cos\theta + y \sin\theta = t, \tag{1.7}$$

where the θ stands for the angle of the line relative to the x axis. Using this formula, a line integral can be expressed as

$$P_\theta(t) = \int_{-\infty}^{\infty} \int_{-\infty}^{\infty} f(x, y)\, \delta(x \cos\theta + y \sin\theta - t)\, \mathrm{d}x\mathrm{d}y, \tag{1.8}$$

where δ is the delta function. This integral transform is called the *Radon transform* – it offers a solution for determining the total density (distribution of attenuation coefficient) of the function f. With this definition, a projection can be described as a set of line integrals for constant θ [2],[12].

The whole projection dataset can be represented in one 2D image called a sinogram (fig. 1.3). The sinogram image has on one axis the angle of the projection and on the other the distance of the projection ray to the center of rotation. A horizontal line in the sinogram represents each measured projection.

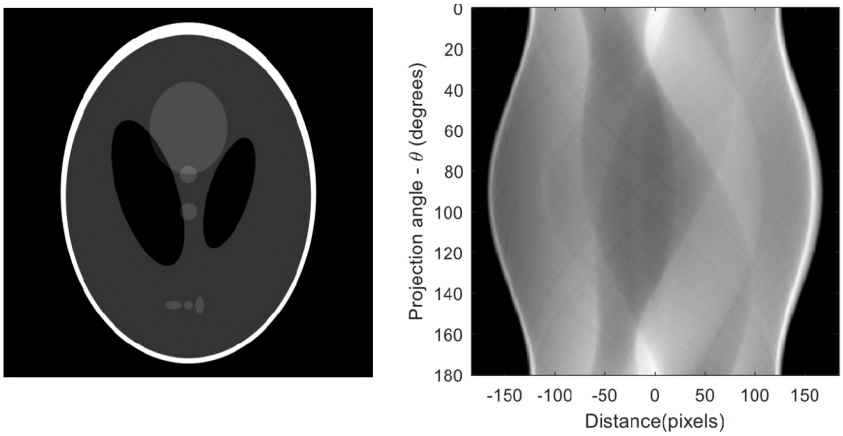

Figure 1.3: Shepp-Logan head phantom on the left and its sinogram consisting of projections from angles $\langle 0, 180 \rangle^\circ$ on the right.

The analytic reconstruction algorithms are built on the principle of the Fourier slice theorem, which connects the Radon transform of a 2D function with its Fourier transform. The Fourier transform is an integral transform, that converts the function f to its frequency spectrum F. It is generally a complex function and can be separated into two parts – amplitude and phase spectrum. Many important characteristics of the original function can be obtained from its spectrum. The 2D Fourier transform of a function f is defined as

$$F(u, v) = \int_{-\infty}^{\infty} \int_{-\infty}^{\infty} f(x, y)\, \mathrm{e}^{-\mathrm{i}2\pi(ux+vy)}\, \mathrm{d}x\mathrm{d}y, \tag{1.9}$$

where u and v represents spatial frequencies. More information about the Fourier transform can be found in [2] or [12]. The Fourier transform of a projection at an angle θ, $P_\theta(t)$ is defined as

$$S_\theta(\omega) = \int_{-\infty}^{\infty} P_\theta(t)\, \mathrm{e}^{-\mathrm{i}2\pi\omega t}\, \mathrm{d}t. \tag{1.10}$$

Now, let's consider a line in the frequency domain given by $v = 0$. The equation (1.9) will change to

$$F(u,0) = \int_{-\infty}^{\infty}\int_{-\infty}^{\infty} f(x,y)\,\mathrm{e}^{-\mathrm{i}2\pi ux}\,\mathrm{d}x\mathrm{d}y. \tag{1.11}$$

Since the exponent is not dependent on y, the integral can be split such as

$$F(u,0) = \int_{-\infty}^{\infty}\left[\int_{-\infty}^{\infty} f(x,y)\,\mathrm{d}y\right]\mathrm{e}^{-\mathrm{i}2\pi ux}\,\mathrm{d}x. \tag{1.12}$$

By substitution the inner integral with the equation (1.8) for a projection lines with constant x and $\theta = 0$, the equation changes to

$$F(u,0) = \int_{-\infty}^{\infty} P_{\theta=0}(x)\,\mathrm{e}^{-\mathrm{i}2\pi ux}\,\mathrm{d}x. \tag{1.13}$$

Thus, the relationship between the projection at angle $\theta = 0$ and the 2D Fourier transform of the function f of the object can be expressed as

$$F(u,0) = S_{\theta=0}(u). \tag{1.14}$$

This equation is the simplest representation of the *Fourier slice theorem* [12].

In words, the Fourier slice theorem states, that the 1D Fourier transform of the projection of an object f taken at an angle θ is equivalent to a slice going through the origin in a 2D Fourier transform of the object f under the same angle θ.

Now, with this theorem in place, the idea behind analytic reconstruction is straightforward. If a sufficient number of object projections is captured over the range from 0 to π, they can fill the whole 2D Fourier space. This Fourier spectrum represents the object being reconstructed, and with the inverse Fourier transform, the object can be recovered [2], [12].

The filtered back-projection method

Even though the Fourier slice theorem gives a simple solution to the reconstruction problem, it is not perfect and brings some challenging issues that need to be fixed. In practice, only a finite set of projections can be captured, so the Fourier spectrum will be known only along a finite number of lines going through the origin – the spectrum is sampled in polar coordinates. The density of points near the origin is large and is decreasing with a higher distance from the origin (see fig. 1.4) [12].

To apply the inverse Fourier transform, the data needs to be interpolated into a Cartesian grid. With the lower density of the point further away from the center – in the higher frequencies, the interpolation error is larger. The entire reconstructed image is affected by this error, resulting in a blurry appearance and suppressed edges, textures, and details. To overcome these issues, the *filtered back-projection algorithm* (FBP) was developed [12].

The FBP algorithm works in two steps, first is the filtering part – the projections are weighted in the frequency domain, and the second part is the back-projection, which can be interpreted as smearing or adding each filtered projection over the image plane in the corresponding angles. The two steps can be described mathematically easily. The filtering operation can be represented as

$$Q_\theta(t) = \int_{-\infty}^{\infty} S_\theta(\omega)|\omega|e^{\mathrm{i}2\pi\omega t}\,\mathrm{d}\omega, \tag{1.15}$$

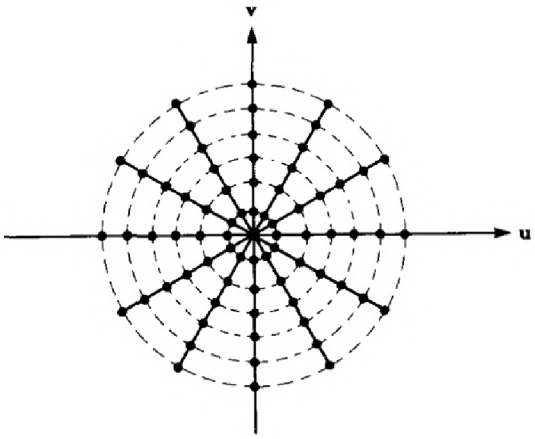

Figure 1.4: Sampling of the projections in the Fourier spectrum based on the Fourier slice theorem, adapted from [12].

and the back-projection can be expressed as

$$f(x,y) = \int_0^{\pi} Q_\theta(x\cos\theta + y\sin\theta)\,\mathrm{d}\theta. \tag{1.16}$$

The derivation of both of the equations can be found in [12], [2]. The term $|\omega|$ in the filtering operation (1.15) represents a frequency response of a filter function (also called the ramp filter), and the whole integral corresponds to the inverse Fourier transform of the quantity $S_\theta(\omega)|\omega|$. The Q_θ can be called the filtered projection. The back-projection equation (1.16) simply states that the reconstructed image f is a summation of all filtered projections over the interval $\langle 0, \pi\rangle$. It is the filtering process, which corrects the low-frequency blur of the data [12].

Note, that based on the important property of the Fourier transform the multiplication of two functions in the Fourier space is equivalent to the convolution of these functions in the spatial domain. The convolution may be expressed as

$$Q_\theta(t) = \int P_\theta(\alpha)\, p(t-\alpha)\,\mathrm{d}\alpha, \tag{1.17}$$

where P_θ is the measured projection and p is the inverse Fourier transform of the ramp filter [12]. The ramp filter controls the enhancement of higher frequencies and with that also the amount of noise present in the image, as well as spatial resolution. Therefore, by multiplication of the basic filter $|\omega|$ with a suitable function, the characteristics of the reconstructed image can be changed. Generally, the filter function can be written as

$$H(\omega) = |\omega| \cdot b(\omega), \tag{1.18}$$

where the function b can be one of the following functions [13]:

$$b(\omega) = \begin{cases} 1 & \text{Ram-Lak filter,} \\ \operatorname{sinc}\frac{\omega}{2} & \text{Shepp-Logan filter,} \\ \cos\frac{\omega}{2} & \text{Cosine filter,} \\ \alpha + (1-\alpha)\cos\omega & \text{Hann } (\alpha = 0.5) \text{ and Hamming } (\alpha = 0.54) \text{ filter.} \end{cases} \tag{1.19}$$

In figure 1.5 the different filter functions are shown.

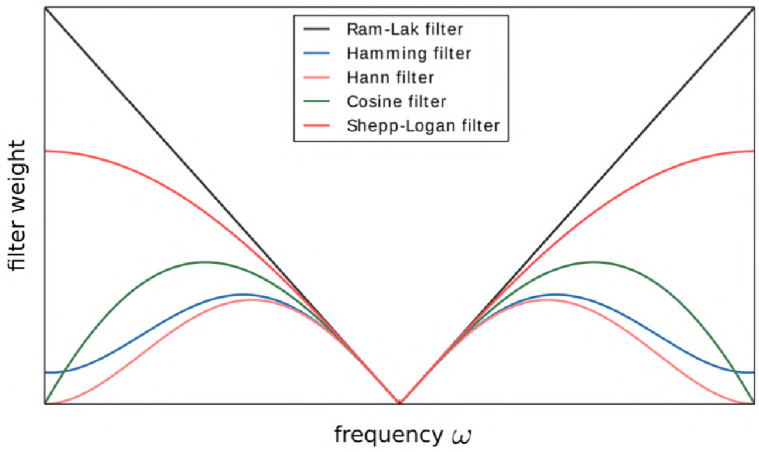

Figure 1.5: Frequency responses of described filters commonly used in the FBP algorithm. Adapted from [13].

It is important to say, that the FBP algorithm was derived only for the parallel-beam geometry. However, in practice, the fan-beam and cone-beam geometries are widely used. For fan-beam geometry, the simplest solution is straightforward – it is possible to convert fan-beam projections into parallel-beam ones, and then apply the FBP. This so-called rebinning of the fan-beam projections however results in non-uniform distances between the rays and can lead to more errors in the reconstruction. More information and derivation of the reconstruction for fan-beam geometry can be found in [12].

The cone-beam geometry reconstruction is much more complex since the three-dimensional dataset is being processed. One of the most famous algorithms, that has successfully solved the problem, is the *Feldkamp-Davis-Kress* (FDK) algorithm. It is empirically derived from the 2D fan-beam FBP – each cone-beam projection row is processed as a fan-beam one [14].

1.4.2. Iterative reconstruction algorithms

Another approach to the reconstruction process is based on linear algebra, and the methods in this group are called *iterative reconstruction techniques*. As well as in the previous section, the idea behind the methods will be described for the 2D object represented by an unknown vector $\boldsymbol{\mu}$ and the object's projections $\mathbf{p}$. It can be proved, that the two vectors can be linked in a simple formula [2]

$$\mathbf{p} = \mathbf{A}\boldsymbol{\mu}. \tag{1.20}$$

Let's consider, that the final reconstructed image is constructed of the total number of N cells. The one-dimensional vector $\boldsymbol{\mu} \in \mathbb{R}^N$ describes the image values in these cells and the vector $\mathbf{p} \in \mathbb{R}^M$ stands for the M rays in the measured projections. The $\mathbf{A} \in \mathbb{R}^{M \times N}$ is a weight matrix. Each weight factor a_{ij} in the matrix $\mathbf{A}$ represents, how the corresponding cell contributes to the measured value in the vector $\mathbf{p}$. From this definition, it is clear, that the matrix $\mathbf{A}$ is sparse due to the fact, that only a small number of cells in the object interact with the beam [12].

By determining the sparse matrix $\mathbf{A}$ the vector $\boldsymbol{\mu}$ can be calculated. For small values of M, N it would be possible to invert the system of equation (1.20) easily. But in practice, both M and N are large, so such inversion would be computationally demanding or

even impossible [12]. However, many solutions to this problem were developed, usually using iterative methods. These methods start with an initial guess of the solution $\boldsymbol{\mu}^{(0)}$ and produce a sequence of vectors $\boldsymbol{\mu}^{(0)}, \boldsymbol{\mu}^{(1)}, ..., \boldsymbol{\mu}^{(n)}$. Ideally, this sequence converges to $\boldsymbol{\mu}$. In each iteration, the projection vector $\mathbf{p}^{(j)}$ is calculated, and the difference between this projection and the measured projection $\mathbf{p}$ is determined. Based on the difference vector, the new vector $\mathbf{p}^{(j+1)}$ is estimated. This process is iteratively repeated till a certain criterion is fulfilled or a maximum number of iterations is reached. Also, specific constraints can be incorporated into the process for faster convergence, typically non-negativity of the $\boldsymbol{\mu}$ (the attenuation coefficient cannot be negative in transmission CT), etc [2].

The advantage of the iterative techniques is, that the model of the CT acquisition can be simulated and integrated into the reconstruction. Such models include the system geometry, the position of the rotational axis and its tilt, shape, and size of the focal spot as well as the photon statistics or the electronic noise [15].

The most well-known iterative methods are the *Algebraic Reconstruction Technique* (ART), *Simultaneous Algebraic Reconstruction Technique* (SART), or *Simultaneous Iterative Technique* (SIRT).

ART is the simplest and oldest of these techniques. The drawback of this method is that it updates the reconstruction only in single rays, thus single pixels. This approach usually does not provide very satisfying results, since the computed ray sums are not good approximations of measured rays. The SIRT algorithm on the other hand updates the reconstruction once after going through all ray sums. The change value, that is used for updating each cell is calculated as an average value of all changes in that cell during one iteration. The SIRT algorithm is slower in convergence than ART but results in better image quality. A compromise between the ART and SIRT algorithms is the SART algorithm – providing a good quality reconstruction with faster convergence than SIRT. It simultaneously updates all the rays in one projection and reduces errors in the ray's approximation. On the other hand, a relaxation factor is necessary for the stability of the algorithms and for noise reduction [12].

Other iterative approaches have been developed in addition to the discussed techniques – for example *Conjugate Gradient Least Square* (CGLS) algorithm, *Adaptive Statistical Iterative Reconstruction* (ASIR), *Sinogram-Affirmed Iterative Reconstruction* (SAFIRE) and others. The iterative reconstruction techniques are studied especially for the medical CT systems since they enable a significant dose reduction due to the incorporated acquisition modeling. Over the past years, it became clear, that iterative reconstruction techniques over-perform the analytical ones, mainly in terms of handling some degradation of image quality during reconstruction, such as artifacts and noise, and dealing with a sparsity of data. But the convergence speed of these algorithms is a serious disadvantage [16].

Arifacts

Even though such powerful techniques for CT reconstruction exist, the reconstructed slices are not exact representations of the measured volume. Theoretically, any difference between the object's actual attenuation coefficients and the estimated ones after reconstruction can be called *artifact*. However, this definition is rather broad, so in practice, only the artificial features in the reconstructed image, that are significant and downgrade the image clarity are considered artifacts [2].

Generally, the artifacts can be caused by many influences – the CT system, the object itself, or the limitations of the software. The most common artifacts are:

- beam-hardening,
- ring artifacts,
- motion artifacts,
- metal artifacts,
- scattered radiation-induced artifacts,
- noise.

The topic of CT artifacts, their causes, and reduction techniques is wide, but in this work, only the noise and noise-related artifacts will be discussed in detail. For more information about this topic see [2].

1.5. Aspects in the CT measurement affecting the noise

Noise can be defined as unwanted random variations of the detected signal and contributes to the uncertainty and distortion of acquired information. Due to the complexity of the entire CT process, noise in projection images is inevitable and consists mainly of electronic noise, structural noise, and quantum noise. Many quantities can affect the noise in the CT process (see fig. 1.6), especially related to the scan settings, the detector, the measured object, or the reconstruction algorithm used. In the following section, some of the most important influences are introduced.

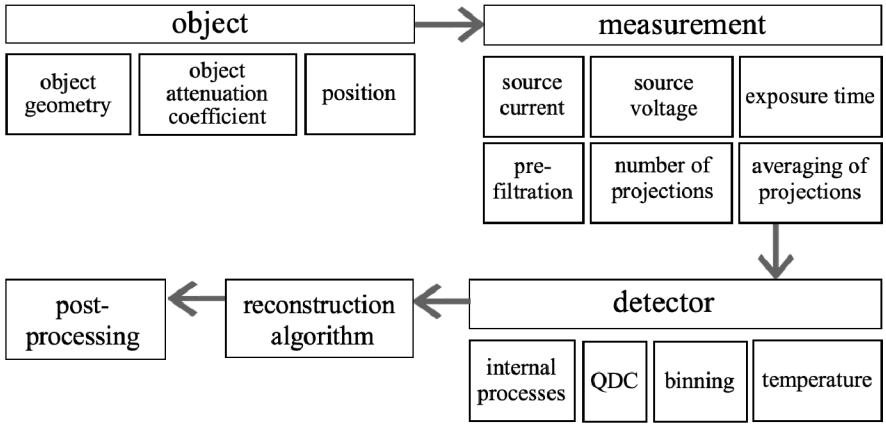

Figure 1.6: A schematic representation of influences affecting the noise in the whole CT process.

A lot of metrics have been proposed for measuring the noise in images. In this section, the influences will be discussed using one of the most frequent ones – signal-to-noise ratio (SNR). The signal-to-noise ratio is an important coefficient for evaluating the detectability of an object in a noisy background [17]. The SNR in a region of interest (ROI) is defined as the ratio between the mean value μ_o and the noise. The noise can be characterized by

many quantities, but usually, a standard deviation σ_o of the ROI is used. In that case, the SNR can be written as [17]

$$\text{SNR} = \frac{\mu_o}{\sigma_o}. \tag{1.21}$$

A low-SNR image has a noise level near the signal, resulting in a noisy image and low detectability of the measured object. The increase in the SNR is favorable to improving image quality. The very famous Rose criterion generally describes the values of SNR – the signal of the object must be at least five times the standard deviation of the background to be detectable [18].

1.5.1. Number of detected photons

The number of photons detected by the detector can have a direct impact on image quality, affecting not only the level of noise in the final image but also the overall intensity, signal, and contrast. The noise, that is related to photon statistics is called shot noise (or quantum noise). Shot noise in optical devices comes from the quantum nature of light and arises from statistical variations in the rate of photons emitted. This process can be modeled with signal-dependent Poisson distribution. From basics about Poisson distribution (see section 2.2.4), the SNR can be written as $\text{SNR} = \frac{N}{\sqrt{N}} = \sqrt{N}$, where N stands for counts of photons. Therefore, with a larger number of detected photons the SNR is increasing, so the shot noise has less power in the image. The factors that influence the detected photons are:

- *Source current:* The cathode in the X-ray tube must be heated by current to generate free electrons through the thermoelectric effect. Increasing the source current results in more electrons leaving the cathode and interacting with the anode, which leads to the generation of more photons. The number of detected photons N is linearly related to the source current I. With increasing source current, the number of emitted photos is also increasing with the relation $\sqrt{I}$ [19].

- *Source voltage:* The energy of electrons leaving the X-ray tube is determined by the voltage applied to it. This energy is linked to the energy of the generated photons, and photons with higher energy have a greater chance of reaching the detector after penetrating the object. Therefore, by increasing the voltage the number of detected photons is increasing. However, the relationship between the source voltage and detected noise is more complex. Determining the appropriate voltage and current settings can be challenging since the sample's material, density or geometry need to be considered [19].

- *Exposure time:* The relationship here is simple – with longer exposure time, more photons are detected per pixel, which results in a higher signal. The number of detected photons and exposure time are related linearly, so the SNR is increasing with $\sqrt{t}$, where t is the exposure time [19].

- *Pre-filtration:* A broad spectrum of energies is emitted from the X-ray source (see section 1.2). X-rays with lower energies are more likely to be absorbed by the object and thus have a smaller impact on the detected signal. So filtering of these rays is a good way to improve the beam quality [2]. Physical filters consisting of thin plates

of copper or aluminum are placed between the X-ray source and the object. The photons with lower energies are absorbed by these filters. This results in a lower number of detected photons, but the beam has improved quality and some artifacts such as beam hardening or cupping artifacts are reduced [19].

- *Object attenuation coefficient:* For each material the attenuation coefficient is known. With a higher attenuation coefficient, more photons are attenuated resulting in a lower detected signal, thus lower SNR. The attenuation coefficient not only depends on the material composition and density but is strongly related to the photon energy – with higher energy, the coefficient is decreasing. So, the noise can be suppressed with a higher source voltage, but the contrast of the captured image will be lower. The attenuation coefficient also sets a limit on the maximum accumulated material thickness that can be penetrated [19].

- *Object length:* Directly from the Beer-Lambert equation it can be concluded that the number of detected photons depends on the distance traveled exponentially. The longer the distance is the more photons are attenuated resulting in higher shot noise, thus lower SNR. This relation directly affects the noise in the reconstructed images – the noise will vary spatially across a volume. The non-stationarity of the noise is a typical characteristic of the CT images [19].

Each of the described aspects can be used to decrease the noise in the captured projection images, but it is important to say, that there is always a certain trade-off. For example, a higher voltage is used to reduce the noise, but with that, the image contrast will be lower. Higher exposure time leads to images with a higher signal – higher SNR and lower shot noise, but the probability of the sample's movement or structural changes due to radiation is increased. So the limits and trade-offs should be acknowledged and understood to achieve images with good quality [2].

1.5.2. Measurement strategy

The system operator can affect the final quality of the measurement, simply by determining the right placement and orientation of the scanned object or choosing the overall strategy of the measurement – a sufficient number of projections, or averaging of the projections. These influences will be discussed in detail:

- *Object placement:* Object's position relative to the source and detector and its orientation should be also taken into consideration during measurement. A system operator should try to find an optimal sample orientation, where the maximum thickness of the object to be penetrated is minimized. In the ideal case, the thickness of the sample would be constant during the whole measurement – from each angle. Otherwise, it can lead to saturation of pixels in the projection, where the object is the thinnest. The sample should be oriented that way so that no sharp edges are parallel to the X-ray beam avoiding beam scattering and instabilities in 3D reconstruction – for example, partial volume effects. The object placement is also connected to the geometry of the beam. With a cone beam, placing the object closer to the detector within the range of the beam results in a higher magnification of the object due to the geometry, known as geometric magnification (see section 1.3) [4].

- *Number of projections:* It is obvious, that the number of captured projections has a serious impact on the final reconstructed slices, especially when the analytical methods are used. It was demonstrated, that the SNR is proportional to the squared number of projections N_p [20]:

$$\text{SNR} \propto \sqrt{N_p}. \tag{1.22}$$

Therefore, with more data, the reconstruction using traditional reconstruction algorithms is more accurate and less noisy. In contrast, an insufficient number N_p can generate artifacts – dark streaks or noise-like distortions (fig. 1.7). However, the trend nowadays is to perform faster measurements – to take less projection. Iterative techniques with prior information can reduce the N_p significantly, but other techniques to reduce the number of projections needed were developed [20]. These attempts are focused in the projection domain, i.e. interpolating between sparse projections, in the reconstruction domain – reconstruction algorithms based on compressed sensing [21] or in the post-processing in the tomogram domain. Neural networks and machine learning are widely used in all of these approaches reaching great results [22].

(a) (b) (c)

Figure 1.7: Reconstruction of Shepp-Logan phantom from (a) 180 projections, (b) 60 projections, (c) 36 projections. With a lower number of projections, artifacts such as dark streaks of noise-like distortions are generated.

- *Averaging of projection images:* In some CT systems, there can be implemented the option to set the number of images captured from each angle under the same conditions – temperature, current, voltage, etc. These images are then averaged, and only one resulting image is used for further processing. The idea behind this procedure is based on the random spatial distribution of photon shot noise across the detector pixels. By averaging multiple images taken under the same conditions, these random fluctuations can be reduced by the square root of the number of images. In general, this technique can improve the quality of the images but results in much higher measurement times, and the reduction of noise is usually not so efficient [23].

1.5.3. Detector

As stated before, the detector plays a crucial role in the CT system. It affects not only the shot noise but also contributes to the final noise with electronic noise. The previous section described the factors that determine the number of photons reaching the sample or leaving it. In this section, also the relation between the incoming photons and generated signal in the detector will be discussed. Only the case of scintillation-type detectors is considered.

The inside structure of the detector itself adds noise to the image. This noise is not related to the number of detected photons – it is signal-independent. This noise, known as dark current noise, arises from fluctuations in the number of photons generated thermally within the detector. These fluctuations are inevitable at any temperature above absolute zero and result in a background noise, which is present even when there are no incident photons [7]. The noise level is dependent only on the temperature of the device, meaning it can be significantly reduced by cooling the detector. In the process of converting the measured charge to a voltage signal, the readout noise is introduced. Readout noise comes usually from the on-chip preamplifier. This noise is signal-independent and follows the Gaussian distribution. Eventually, before the analog-to-digital converter, the signal is usually amplified resulting in further noise [7].

Some detectors have the option to use the pixel binning function as a strategy how to increase the SNR. But with pixel binning, the spatial resolution is compromised and the dark current noise becomes more powerful in the image [24].

The effectiveness of a detector can be measured using quantum detection efficiency (QDC). The QDC represents the detector's ability to produce high SNR output images for a given number of incident photons. In other words, the QDC can be expressed as a fraction of incident photons, that are converted to signal, since the detector doesn't detect every photon. Every detector can be described using QDC in percentages. The ideal detector would have the QDC 100% at all spatial frequencies, meaning that all energy is absorbed and contributes to the image signal. High QDC corresponds to high contrast in the final image and the detectability of low-contrast objects is improved [23], [2].

1.5.4. Tomographic reconstruction

Just from the mathematical basics discussed in section 1.4 it is obvious, that the algorithm used for the reconstruction can affect the noise significantly. The principle of analytical reconstructing algorithms relies on theorems derived from many simplifications and approximations regarding the CT system and continuity of the data – for example, an infinitely small point-like X-ray source, monochromatic X-ray beam or an infinite number of noise-free projections were considered [15]. Due to the fact, that these conditions are never met in practice, the final noise has a strong impact on the reconstructed slices. The assumption of infinite projections implies that a larger number of projections will result in better quality and less noise. However, since the number of projections is always finite, some noise is inevitable. If the number of projections is insufficient, the noise will increase significantly, new artifacts will be created and the quality will downgrade (fig. 1.7). Overall, the FBP algorithm is very robust, fast, and useful, but it is not suitable for non-ideal conditions during the measurement, especially when it comes to low dose measurement or sparse or irregularly spaced projections [15].

The iterative algorithms follow a totally different approach based on linear algebra. They consider the data to be discrete from the start, so no assumption of continuity is involved. They also enable a powerful regularisation step and a high level of modeling of the CT system and the whole acquisition process. Thus, they offer an effective reduction of noise in the final reconstruction and suppression of generated artifacts. The strengths of the iterative algorithms include a very high potential for low-dose reconstruction and preserving the quality and spatial resolution using only a fraction of the standard number of projections. So, the iterative reconstruction can notably shorten the measurement time, but the computational costs are very high, but nowadays a highly efficient GPU-based implementation is possible to speed the reconstruction up [15], [16].

However, by using iterative reconstruction techniques, the noise magnitude, texture, and distribution are changing, so the visual appearance of the reconstructed images is different compared to the FBP reconstruction. Also, some studies have demonstrated, that they can produce images that look over-smoothed and unnatural [25]. Nowadays, machine learning and deep learning reconstruction techniques are widely studied and developed in order to reduce noise without changing the underlying structure of the sample. However, these techniques usually demand a large database of training data. The training stage of the methods is usually very computationally demanding, but once the training is complete, the reconstruction is typically faster than with iterative techniques [26], [25].

It is important to note, that the choice of reconstruction algorithm depends on the quality of the measured dataset, the measurement strategy, and on the amount of time available for the reconstruction itself.

2. Noise in digital images and its reduction

In classical photography, the recording of an image is easily done thanks to a light-sensitive material inside a camera. The image's intensity will be higher where a larger number of photons lands during the exposure and conversely. In digital cameras and detectors, the principle stays the same, but instead of a light-sensitive material, the digital chip is used. The chips are usually rectangular matrices with photo-sensitive elements, such as photodiodes. Using the photoelectric effect, the photo-diodes transform light photons into electric charges. The output image is always in greyscale. To record a color image, a color filter needs to be placed before the photodiodes – the most common filter is a Bayer mask with red, green, and blue filters. When the light travels through the mask, it is absorbed and only a part of the spectrum corresponding to one color reaches the photo-diode [27].

Generally, every real image contains noise. The noise is generated during the acquisition process, during the converting stage, and even during the post-processing of the image in the computer – for example from rounding errors. This chapter will cover the fundamental basics of the digital image, as well as types of noise that can corrupt the image, and a review of the denoising algorithms.

2.1. Digital image

The digital image can be represented by a two-dimensional discrete function I, which is defined in a series of positions $m = 1, \ldots, M$, $n = 1, \ldots, N$. The number N is called the image *width* and M is the image *height*. Each position (m, n) in the function represents one picture element – *pixel*, and function I donates the response of the pixel. This response usually corresponds to the optical intensity. To obtain the digital image, the 2D spatial signal f needs to be converted through a sampling process, also called discretization. In imaging sensors, such as CCD chips, the discretization happens naturally [28].

In a greyscale image, each pixel contains only one numerical value representing the signal (see fig. 2.1 (a)). On the other hand, pixels in color images carry a vector of numbers. I most cases, the vector consists of a triplet of the (R, G, B) components – values for red, green, and blue colors (see fig. 2.1 (b)). The final color of the pixel is the linear combination of the basic colors corresponding to the vector. Another famous color model besides the RGB is the CMYK. The CMYK model contains four colors – cyan, magenta, yellow and black [28].

Each digital image can be described with a characteristic called *bit depth*. It defines, how many intensity values can be used for describing the signal of the pixel. An image has a bit depth of n *bits per pixel* (or the image is called n-bit) when the total number of tones is 2^n. The higher the number n, the more tones are available. The range of possible pixel values is called the *dynamic range* of an image. In practice, 8-bit or 16-bit images are the most common. For a 16-bit image, there is $2^{16} = 65\,536$ intensity values available – the dynamic range is the interval $\langle 0, 65\,535 \rangle$, where the values 0 and 65 535 represent the black and white color. For color images, there is one intensity value for each color according to the model used (fig. 2.1 (b)) [27].

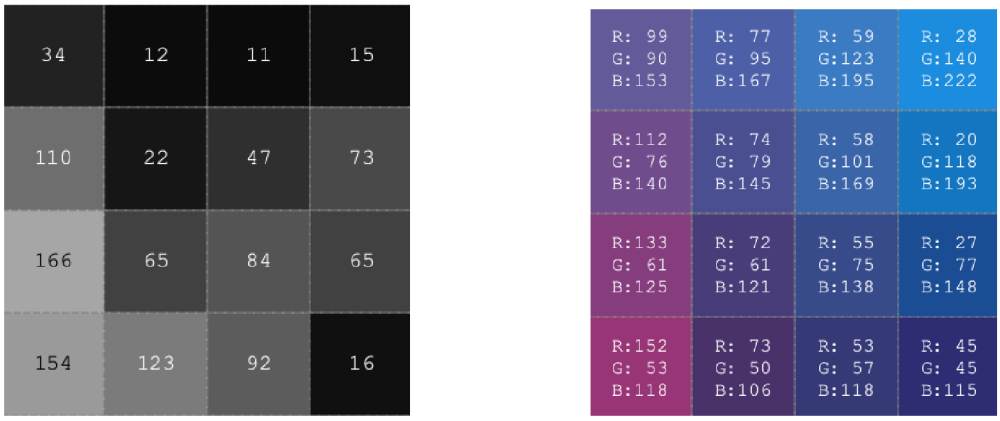

(a) (b)

Figure 2.1: Pixel values of an 8-bit image in (a) gray-scale, (b) RGB color model.

2.2. Types of noise

As stated at the beginning of this chapter, the noise is always present in an actual image as an „unwanted" signal. A higher noise level can lead to degradation of the image quality or lower the detectability of the captured object. To reduce the noise, prior knowledge about the noise type present in the image is required in order to use suitable denoising techniques. Here, the common noise distributions or models will be shortly introduced, such as:

- Gaussian noise,
- impulse noise,
- speckle noise,
- shot noise.

2.2.1. Gaussian noise

The Gaussian noise model is probably the most common type of noise and is often used in practice for various simulations or testing of denoising algorithms. This additive noise has a uniform distribution throughout the image, therefore it is signal-independent at any point, and follows the normal distribution. The probabilistic density function (PDF) of the random variable X representing the noise has a normal Gaussian distribution – $X \sim \mathcal{N}(\mu, \sigma^2)$, which PDF is given by [29]

$$P(X) = \frac{1}{\sigma\sqrt{2\pi}} \mathrm{e}^{\frac{-(X-\mu)^2}{2\sigma^2}}, \tag{2.1}$$

where μ is the mean value of the noise and σ^2 is the variance of the noise. The PDF has a typical bell shape (fig. 2.2) [30]. A Gaussian noise arises from the inside of the detector, such as electronic circuit noise, thermal noise or readout noise.

An important representative of this group is the *additive white Gaussian noise* (AWGN). This noise type assumes to be independent and uncorrelated with the signal, meaning that its value at any given time is not related to its value at any other time, or to the value of the signal (fig. 2.3 (a), (e)). The term "white" refers to the fact that the noise is spread evenly across all frequencies [30].

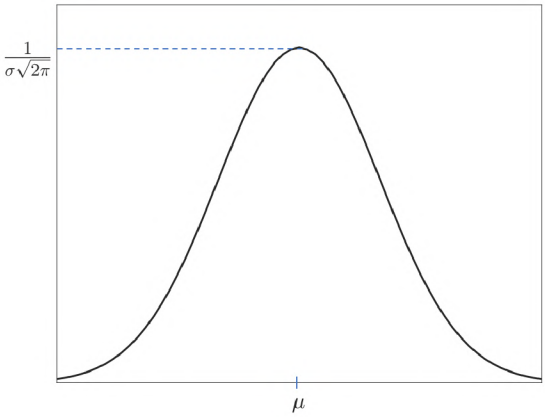

Figure 2.2: The probabilistic density function of the Gaussian distribution with mean value μ and variance σ^2.

2.2.2. Impulse noise

This noise is very easy to identify since it occurs as randomly distributed white and black pixels. Because of its appearance, the noise is also called the *salt and pepper noise* (see fig. 2.3 (b), (f)). Only those values of the affected pixels are changed – either to 0 or 1, and there is a possibility of an unaltered pixel's neighborhood. As a result, there are effective filters for reducing noise pixels based on their surroundings [30].

The impulse noise can have many origins – dead or hot pixels in the detector, the presence of dust particles, cosmic rays, and many more.

2.2.3. Speckle noise

Speckle noise affects the image in a different way. This noise is multiplicative, which means that the noise values are multiplied by the signal. Since it depends on the pixel values, it is signal-dependent (see fig. 2.3 (c), (g)) and thus very challenging to reduce. Usually, the PDF of this noise follows the Gamma distribution [30].

This noise can corrupt coherent imaging systems, such as radar, laser, or ultrasound images, etc.

2.2.4. Shot noise

The shot noise (fig. 2.3 (d), (h)) comes from the quantization of the electromagnetic radiation and is fluctuating with the number of photons emitted. This fluctuation is time-dependent. The noise is characterized by having a variance that is proportional to the signal, which means that as the signal intensity increases, the amount of noise also increases. The random variable X follows a Poisson distribution $X \sim \mathcal{P}o(\mu)$ and the PDF is given as [29]

$$P(X) = \frac{\mu^k \mathrm{e}^{-\mu}}{k!}, \qquad k \in \mathbb{N}_0, \tag{2.2}$$

where k is the number of occurrences during some interval. When this number k is sufficiently high the random variable with Poisson distribution $\mathcal{P}o(\mu)$ can be approximated with normal distribution $\mathcal{N}(\mu, \mu)$ due to the central limit theorem. This theorem states that the sum of a large number of independent, identically distributed random variables

approaches a normal distribution, even if the individual random variables are not normally distributed [31]. This approximation is often used in X-ray images.

Another important property of the Poisson distribution is that the mean value of the noise equals the variance, such as [29]

$$E(X) = \mu, \qquad \sigma^2 = \mu. \tag{2.3}$$

The shot noise and the influences generating the noise were described more in detail in the section 1.5.1.

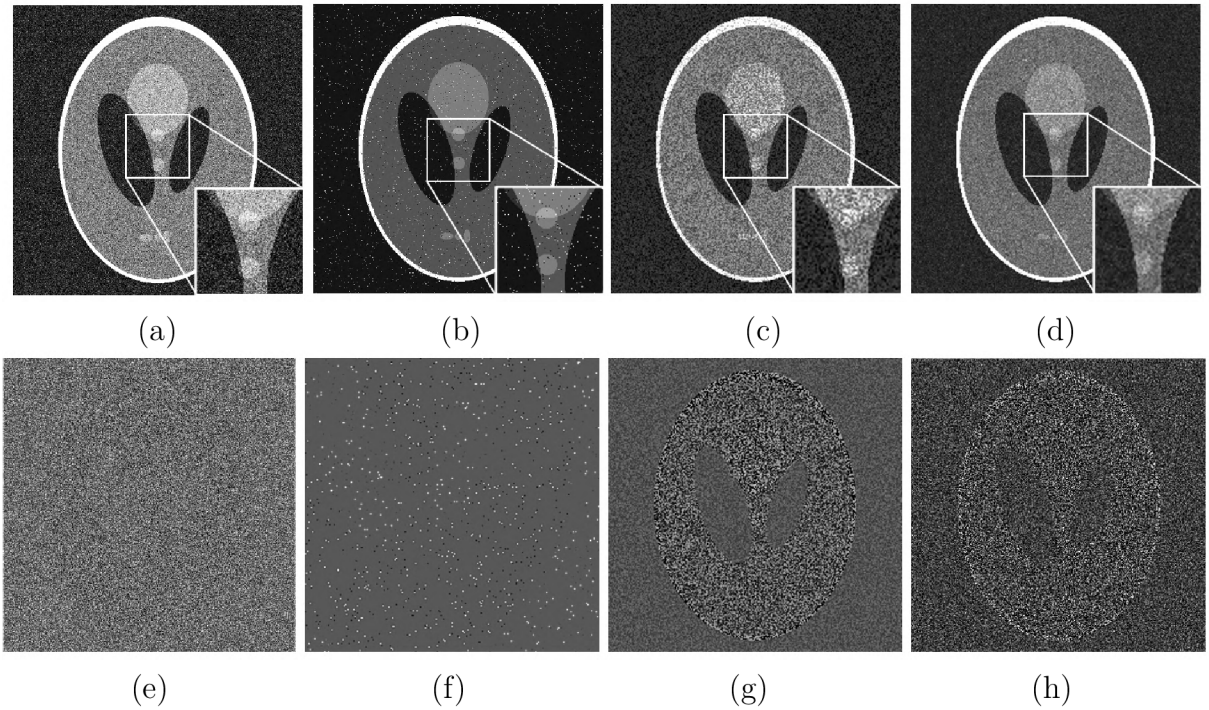

Figure 2.3: The Shepp-Logan head phantom corrupted by (a) Gaussian noise with $\mu = 0$ and $\sigma^2 = 0.01$, (b) impulse noise with density 2% of pixels, (c) speckle noise, (d) Poisson shot noise. Corresponding residual noise images after generating (e) Gaussian noise, (f) impulse noise, (g) speckle noise, and (h) Poisson shot noise.

However, it is important to note, that some level of noise can be also useful. In textured images, a small amount of noise can lead to better perceptual quality and an even sharper appearance. But on the other hand, the quality metrics such as SNR would have worse outcomes.

2.3. Denoising algorithms review

In recent years, with the development of advanced technology for the recording of images the need for adequate software to process these images and enhance their perceptual quality has been increasing. Denoising is a large topic in this field since noise can significantly distort the image. The ideal denoising algorithm would preserve flat regions, edges, texture details, and global contrast and it should not introduce new artifacts into the image [23]. But denoising is generally a challenging task, because from the mathematical point of view, it is an inverse problem, and the solution is not unique. Overall, noise

reduction algorithms can be divided into these groups: spatial domain filtering, transform domain filtering, anisotropic diffusion algorithms, and deep-learning methods. This list is still incomplete and new and more progressive denoising algorithms are being developed each year. In this review, only the most popular ones will be introduced, starting with simple methods, such as averaging pixels, to more sophisticated techniques.

Spatial domain filtering. In filtering in the spatial domain, the operation is done directly on the image matrix. Spatial filters can be divided into linear and non-linear filters. Traditionally, linear filters are successful in reducing noise, but cannot preserve edges, lines, fine details, or texture. A typical example in this group of filters is a mean filter or Gaussian smoothing. The mean filter is the simplest method, the pixel intensity is simply replaced by the mean value of the pixels in its neighborhood in a given window. The gaussian filter is an exemplar of a low-pass filter. These filters reduce higher frequencies in the image, thus noise, but also detail, edges, and texture. A Wiener filter [32] has been developed to improve the over-smoothing, but the blurring of the edges is still present. Non-linear filters are slightly more complex; the pixel's value is based on a weighting of the intensity of the pixels in its neighborhood. The best-known filter in this category is the median filter. It simply replaces the center value with the median value of the intensities in a certain neighborhood of the pixel. The median filter can be useful, especially in the case of impulse noise and a big advantage is its minimum time costs. Other two important filters, that are applied in the spatial domain, are bilateral filter [33] and non-local means filter [34]. In these methods, both grey-level similarity and spatial closeness are calculated. The bilateral filter can reduce the noise well while preserving edges and fine details but can fail with high levels of noise in the image or with fast changes in the noise variance. Advanced filters based on bilateral filtering, such as fast adaptive bilateral filter [35], and statistical nearest neighbor bilateral filter [36] have been developed. In the non-local means filter method, the set size of the window around the pixel is searched and the pixels, that are the most similar to the examined pixel are found, and this pixel is replaced by the weighted average of all similar pixels. This approach is more computationally demanding than the bilateral filter, especially when the search window is large or the image has few similar areas, but the preservation of edges and texture is very good. For non-local means were also developed some improvements, for example, statistical nearest neighbor non-local means filter [36] or probabilistic non-local means [37]. In [38] also the extension for volumetric datasets was introduced, called the optimized blockwise NL-means, and was specially designed for denoising of MRI data. It has shown very good results and was able to outperform the classical implementation of non-local means. Based on this algorithm, the Collaborative Approach for eNhanced Denoising under Low-light Excitation – CANDLE [39], was developed. It was first designed to deal with the inhomogeneous noise present in laser scanning fluorescence microscopy images but the method was validated also on synthetic data and in vivo images. Variance-stabilization transform is present in this process to transform the signal-dependent noise into quasi-stationary Gaussian noise to improve the noise statistics for better noise reduction, but the overall time costs of this method are very high.

Anisotropic diffusion and total variation methods. Methods in this group work also in the spatial domain, but the approach they are based on is very specific. The first model was proposed by Perona and Malik [40], where the problem is formulated using a nonlinear

partial differential equation. For the first time, the heat diffusion equation was used in image denoising, and this approach was able to smooth the image and at the same time preserve edges quite effectively, but stair-casing artifacts are present near edges. Higher-order anisotropic diffusion models were tested for removing the artifact [41]. Another important model was proposed by Rudin, Osher, and Fetami in 1992. Their approach is based on the idea, that the denoised image can be estimated as a solution to a minimization problem – ROF problem [42], with the use of total variation based on the L_2 norm. The Split Bregman algorithm is a flexible method for solving the problem with L_1 or TV regularization. Nowadays many methods based on the Split Bregman method have been proposed. But usually, the blocking artifacts are seen near the edges. Recently methods based on total variation were improved to generate artifacts-free denoised images, such as nonnegativity constrained based TV [43], Split Bregman using exponential TV function [44], and coefficients-driven based total variation [45].

Transform domain filtering. As the name suggests, algorithms in this group are working on the representation of the image in the transform domain. Initially, transform domain methods were developed from the Fourier transform, but more and more transforms are introduced to the image denoising, such as wavelet transform, discrete cosine transform (DCT), curvelet transform, etc. These approaches are based on the property, that in the transform domain, the image can be represented by fewer numbers of non-zero coefficients. That way the noise and signal coefficients can be separated more easily, and that way the noise reduction can be more efficient. Wavelet transform is probably the most famous and most investigated transform domain denoising method. It can reduce noise very well while preserving fine details, but the result heavily depends on the wavelet selection. In the work [46], the algorithm based was introduced based on the SURE method (Stein's Unbiased Risk Estimator) combined with Linear Expansion of Thresholds (LET) – SURELET. The algorithms proposed in the paper are based on discrete wavelet transform and showed big potential. An example of discrete cosine transform denoising is the shape-adaptive DCT method (SA-DCT) [47]. Thanks to the shape-adaptive feature it has been able to preserve edges well but resulting in large time costs. In 2007, the method Block Matching and 3D Transform-Domain Collaborative Filtering (BM3D) was introduced [48], and it became the state-of-the-art image denoising method. This algorithm, motivated by the idea of non-local means, showed a very high level of preserving fine details and edges but can be ineffective with a higher level of noise. Hence improvements have been investigated, such as bounded BM3D [49]. Another approach was to incorporate the principal component analysis (PCA) in BM3D resulting in BM3D-SAPCA [50] or to use deep learning [51] for self-adjustment of the algorithm to the noise level in the image. Also, an extension for the volumetric datasets BM4D [52] was done and reached state-of-the-art denoising performance for noise reduction in 3D datasets.

Deep-learning and CNN-based methods. In 1989, the first attempts were made to use a neural network in denoising [53]. Since then, neural networks became larger and more complex. Nowadays, neural networks in image processing are a big trend and can be used in a variety of fields – image recognition, segmentation, robotics, self-driving, facial recognition, etc. The research in denoising is continuing, and since the number of developed methods is very high, only a few will be introduced. A large advantage of methods in this group over the traditional" ones is, that they don't need manually chosen parame-

ters. The very base for the usage of convolutional neural networks in image denoising is introduced in [54] and its architecture is still used. In [55], the denoising convolutional neural network (DnCNN) is described. The main idea of this denoising approach is that it doesn't predict the clean image, but rather the residual image, i.e. the difference between the noisy observation and the clean image. Recently, DnCNN2 was proposed and improves some drawbacks of the DnCNN as well as the noise reduction effect [56], but the computational costs are still high. The disadvantage of these approaches is that the networks are trained on images with a certain noise level and are not suitable for denoising other noise levels. Another method is called NN3D [57], which combines local multiscale denoising by a CNN and non-local denoising based on the non-local filter. It has shown a great ability to exceed the results obtained from each of its components. The fast and flexible denoising convolutional neural network – FFDNet, incorporates also a noise level map, so it provides a flexible way to handle different noise levels and inhomogeneous noise with the use of a single network [58]. This method is very effective and runs fast, but the time costs for training are very high. To generalize the CNN denoising, the convolutional blind denoising network CBDNet was developed to denoise a more sophisticated noise model present in real-world noisy photographs [59] and has great results. The method Noise2Noise [60] proved, that it is possible to recover a signal without observing clean signals, so the recovery is only based on the corrupted image. Additionally, this is done without any further knowledge about noise distribution and other statistics. This is very beneficial in applications, where clean targets are not so easy to create – such as microscope images. Noise2Void [61] takes this even further and can train directly on a single noisy image, so it does not require pairs of noisy images or ground truths. But for successful denoising, the assumption of a predictable signal and pixel-wise independent noise should be met, otherwise the network will fail and generate artifacts.

3. Estimation of the noise model in the projection domain

With everything stated about the CT acquisition process, it is obvious, that noise is always present in the projection images. It is one of the important influences, that can significantly downgrade the perceptual quality of the final reconstructed images, affecting their clarity and overall reliability.

Since the noise in the projection images is a mixture of all noise contributors – photon shot noise, readout noise, dark current noise, and other influences, the distribution of the noise in the projection domain is unknown. The first goal of this thesis is to determine the noise model. By understanding the characteristics and distribution of the noise, it becomes possible to select effective denoising strategies.

3.1. Statistical analysis of noise in bright frames

For estimation of the noise model in the projection domain, the set of bright field images taken by the high-resolution CT system Rigaku nano3DX equipped with a CCD camera was analyzed.

Rigaku nano3DX is an X-ray microscope that operates in quasi-parallel beam geometry, which means that the sample is placed very close to the detector. This microscope allows a very high resolution due to a high-resolution detector, an X-ray source with large stability of the output intensity, and a high-precision sample stage. The spatial resolution in 2D can reach up to 0.27 μm and in 3D the resolution of 0.8 μm is achieved. The Rigaku nano3DX also performs high-contrast imaging with an ultra-wide field of view [62].

Bright-field image refers to an image without any sample present. For analysis of the noise, nine sets of bright field images were captured under different exposure times – from 1 second to 40 seconds. Each set is consisting of 10 frames sized 1 250 px[1] $\times$1 648 px. The material of the target was copper. The analysis was performed in MATLAB [63].

The workflow for statistical analysis of the noise in bright fields is following:

1. loading of the bright frames for certain exposure time (fig. 3.1 (a)),
2. normalizing the data range to interval $\langle 0, 1 \rangle$,
3. removing of outliers and hot and cold pixels from the frames,
4. calculating the average frame from the set (fig. 3.1 (b)),
5. subtracting this average frame from the set for obtaining noise data (fig. 3.1 (c)),
6. calculating the statistical moments from the subtracted noise and displaying statistical plots.

Since the original images are 16-bit, the normalization is done simply by converting the images to double precision (divide the values by 2^{16}). The outliers in the frames are present in the images in the form of impulse noise. This noise is caused mainly by the dead and hot pixels in the camera, scattered radiation, dust particles, or cosmic rays. For

[1] px = pixels

detecting the outliers in this analysis, the method using percentiles is performed. This method detects a pixel value as an outlier if the value is below some given lower percentile or above the given higher percentile. By this method, about 3% of pixels in each set are detected and replaced with the nearest non-outlier value. After this procedure, simply by averaging the frames in each set, the mean frame is calculated and subtracted and only the pixel values corresponding to noise are left (fig. 3.1 (c)).

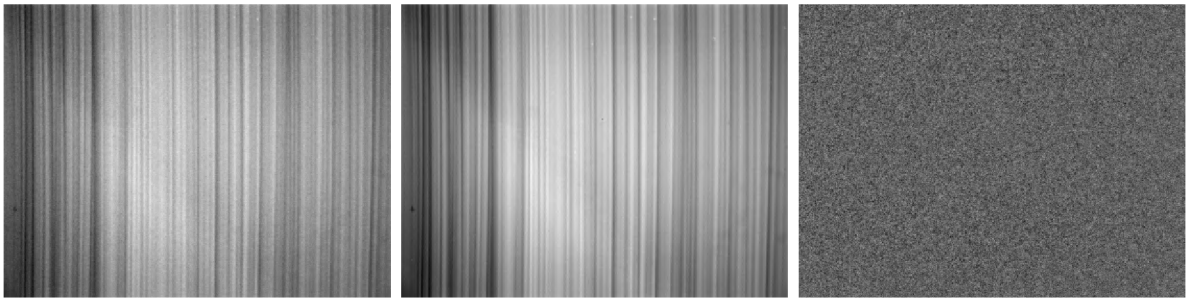

(a) (b) (c)

Figure 3.1: An example of a bright field image taken under exposure time of 15 s (a) and a mean frame calculated from the set of 10 frames for 15 s (b). For statistical analysis, the mean frame is subtracted from the set to obtain the noise data (c).

Now, the statistical analysis of the noise values can be performed. The first thing, that can be analyzed is the normality of the data. Since the data is very large for performing statistical tests ($1\,250 \times 16\,480$ of values for each set), only the statistical plots will be visualized. Also, the statistical moments will be calculated.

The normality of the data will be analyzed using two plots – a Q-Q plot and a histogram. A Q-Q plot (quantile-quantile plot) is a graph used to determine whether a set of values follows a particular probability distribution. The quantiles of the observed data are plotted against the quantiles of a theoretical distribution, typically the normal distribution. For the construction of a Q-Q plot, the observed data is first sorted in ascending order, and then the quantiles are calculated. The theoretical quantiles of the selected distribution are plotted on the x-axis and the observed quantiles are plotted on the y-axis. If the observed data is normally distributed, the points on the Q-Q plot are expected to lay in a roughly straight line. A histogram is another graph representing the distribution of the data. On the x-axis of a histogram, there is the range of values for the variable which is divided into intervals, called bins. The y-axis represents the count of observations falling within each bin. The bins are regularly spaced. Histograms are commonly used in data analysis to examine the shape, center, and spread of the data. The shape of the histogram can provide insights into the underlying distribution of the data. A symmetrical, bell-shaped histogram suggests that the data may be normally distributed.

Based on the theoretical introduction to both of these statistical plots, it is possible to evaluate the outcomes. In figure 3.2 the Q-Q plot of noise data for each exposure time is shown. It is obvious, that with exposure times higher than 10 seconds, the points nicely follow the straight line corresponding to the normal distribution. For lower exposure times – 1 s, 5 s, and 10 s, the deviation from the straight line is larger. The biggest deviation is for 1 second exposure time but is decreasing with higher exposure time. To support this assumption, the mean square error[2] (MSE) of the quantiles of normal distribution and the

[2] $\mathrm{MSE} = \frac{1}{n}\sum_{i=1}^{n}(Y_i - X_i)^2$

quantiles of observed data is calculated. The results are listed in table 3.1. The histograms are shown in figure 3.3 with fitted normal distribution. The same outcomes as for Q-Q plots can be stated for histograms – the largest difference between the histogram of normal distribution and the histogram of observed data can be seen for a 1-second exposure. The higher the exposure, the closer is the experimental histogram to the theoretical one.

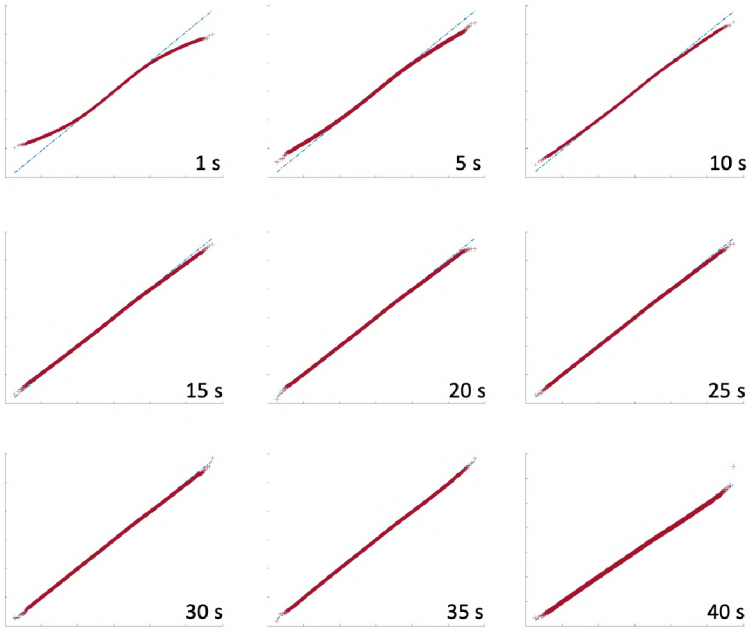

Figure 3.2: Q-Q plots of noise data for each exposure time versus normal distribution. If the data is normally distributed, the points are expected to follow a dashed straight line corresponding to the normal distribution.

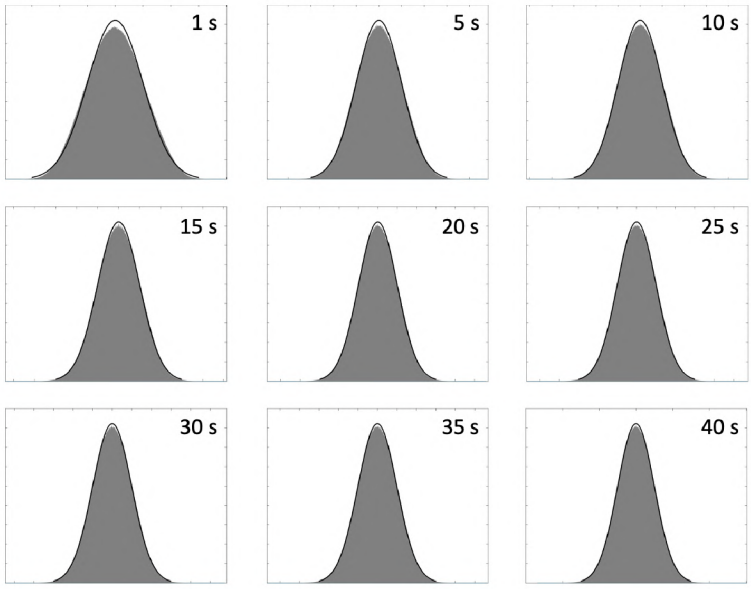

Figure 3.3: Histograms for each exposure time and fitted histograms for normal distribution – a symmetrical, bell-shaped histogram.

Next, the statistical moments of the noise data are calculated – the mean value, variance, and kurtosis. Also, the mean value of the signal in each set is calculated. The results are listed in table 3.1.

Table 3.1: Results from statistical analysis of the bright field images.

	Noise mean value	Noise variance	Kurtosis	MSE of QQ plot	Mean value of the signal
1 s	$-7.114 \cdot 10^{-22}$	$8.307 \cdot 10^{-7}$	2.631	0.00190	0.0823
5 s	$-2.113 \cdot 10^{-20}$	$3.028 \cdot 10^{-6}$	2.757	0.00078	0.1536
10 s	$6.295 \cdot 10^{-20}$	$5.833 \cdot 10^{-6}$	2.828	0.00045	0.2433
15 s	$-6.366 \cdot 10^{-20}$	$8.663 \cdot 10^{-6}$	2.869	0.00028	0.3328
20 s	$-1.897e \cdot 10^{-21}$	$1.151 \cdot 10^{-5}$	2.896	0.00021	0.4223
25 s	$3.898 \cdot 10^{-20}$	$1.436 \cdot 10^{-5}$	2.913	0.00020	0.5116
30 s	$-7.976 \cdot 10^{-20}$	$1.721 \cdot 10^{-5}$	2.927	0.00016	0.6007
35 s	$5.700 \cdot 10^{-20}$	$2.006 \cdot 10^{-5}$	2.939	0.00015	0.6897
40 s	$-4.087 \cdot 10^{-20}$	$2.289 \cdot 10^{-5}$	2.946	0.00012	0.7786

The mean values of the noise for each exposure time can be assumed to be zero since the numbers are small. Several other things can be observed from the statistical moments listed in table 3.1. The kurtosis of noise in each frame is close to the number 3, which is the kurtosis for the normal distribution. The biggest deviation from 3 is for 1-second and 5-second frames and is decreasing with higher exposure time. The closest kurtosis to the ideal value of 3 is in a 40-second bright frame. The MSE of the two quantiles is decreasing. These results are in agreement with the conclusions based on the Q-Q plots and histograms. Another critical remark is, that the variance depends on the signal values and is increasing. These relations will be shown graphically in figure 3.4.

The graphs in figure 3.4 validate the assumptions made – the higher the exposure time, the higher the signal, and the closer the distribution of the noise to the normal distribution. From the plot 3.4 (a), it is clear that the noise variance is linearly dependent on the exposure time. To determine this dependence based on the signal value and not on the exposure time, the relation between the noise variance and the mean value of the signal will be shown (fig. 3.5). The correlation coefficient R between the mean values of the signal and noise variance was calculated, and the value is $R = 1$. Thus, this relation is perfect positive linear and can be expressed with a formula

$$\sigma^2(y(x)) = 3.17 \cdot 10^{-5} y(x) - 1.85 \cdot 10^{-6}. \tag{3.1}$$

An important thing to notice is, that the straight line in the plot 3.5 doesn't cross the origin. Theoretically, if the signal is zero, the variance would be negative, which doesn't make sense from a mathematical point of view. This problem will be discussed in the next section.

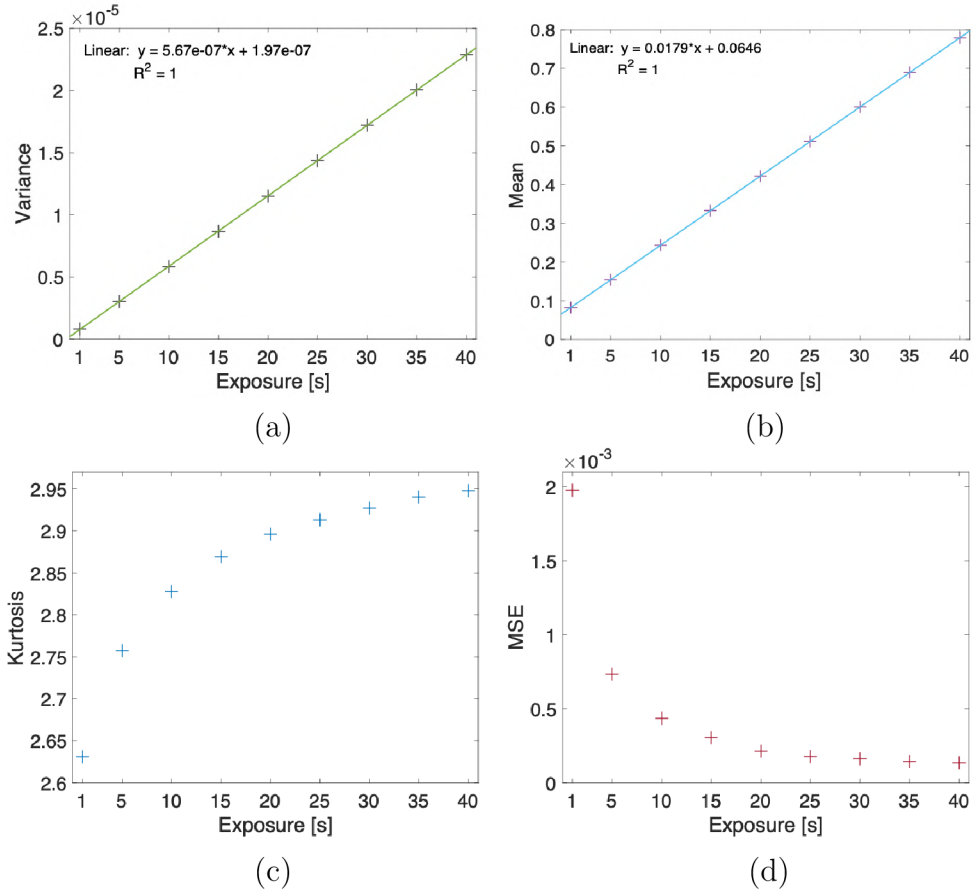

Figure 3.4: Results from table 3.1 shown graphically. The relations are between (a) exposure time and variance of the noise – linear dependence, (b) exposure time and the mean value of the signal in the bright frames – linear dependence, (c) the kurtosis of the noise data and the exposure time – the deviation from the value 3 corresponding to the normal distribution is decreasing with higher exposure times, (d) mean square error (MSE) of the Q-Q plot and exposure time – the MSE is decreasing with higher exposure time.

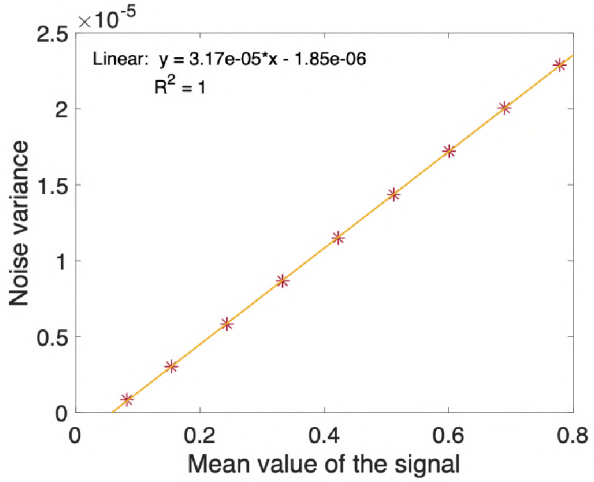

Figure 3.5: The relation between the mean signal value of frames and the noise variance – linear dependency.

Based on the stated outcomes the assumption can be made, that in the range of analyzed exposure times the noise in each bright frame can be assumed as *zero mean Gaussian noise*. However, the noise is signal dependent – the variance of the noise varies with the signal. Based on the theory discussed further in this chapter it is clear, that this behavior is typical for *mixed Poisson-Gaussian distribution*. The Poisson part of the noise represents the influence of the number of detected photons – the signal-dependent photon shot noise and the Gaussian part of the noise corresponds to the signal-independent readout noise, darkcurrent noise, etc.

The same procedure has been done also for molybdenum target bright frames (voltage 50 kV). The statistical analysis validated the outcomes stated for copper target bright frames. For more information about the outcomes see appendix A. However, it should be noted that the noise variance is generally higher in the bright frames obtained using a molybdenum target. As a result, with similar measured signal to the copper target projections, the molybdenum target ones will appear noisier.

3.2. Theoretical model

The image with signal-dependent noise can be modeled as [64]

$$z(x) = y(x) + \sigma(y(x))\xi(x), \tag{3.2}$$

where $x \in X$ is the pixel position in the domain X, $z : X \to \mathbb{R}$ represents the observed signal, $y : X \to \mathbb{R}$ is the noise-free signal, $\xi : X \to \mathbb{R}$ is independent random noise with zero mean and standard deviation of one, and finally $\sigma : \mathbb{R} \to \mathbb{R}^+$ is dependent on the signal y and influences the standard deviation of the whole noise component.

From the experimental results, the assumption was made, that the noise in analyzed images can be modeled as a mixture of two mutually independent parts: a Poissonian noise η_p, which is signal dependent, and signal independent Gaussian noise η_G. With Poisson distribution, the photon shot noise can be modeled (see section 2.2.4) and on the other hand, the readout noise and dark current noise are described with Gaussian distribution (see section 2.2.1). Thus, the second part of the equation 3.2 can be rewritten as [64]

$$\sigma(y(x))\xi(x) = \eta_p(y(x)) + \eta_G(x), \tag{3.3}$$

where

$$\eta_G(x) \sim \mathcal{N}(0, b), \qquad \frac{1}{a}(y(x) + \eta_p(y(x))) \sim \mathcal{P}o(\frac{1}{a}y(x)). \tag{3.4}$$

The $a > 0$ and $b \geq 0$ are real scalar parameters. The term a stands for the photon shot noise parameter as per the quantum efficiency of the sensor. The larger the parameter a, the higher the number of incident photons to generate a signal. With larger b the Gaussian noise has a bigger impact on the image [65].

As stated before, the mean value and variance of the Poisson distribution are equal, so it can be obtained

$$E\left(\frac{1}{a}(y(x) + \eta_p(y(x)))\right) = \text{var}\left(\frac{1}{a}(y(x) + \eta_p(y(x)))\right) = \frac{1}{a}y(x). \tag{3.5}$$

This equation can be rewritten using the relations for mean values and variance[3]. So, the left side of the equation (3.5) can be rewritten as [65]

$$E\left(\frac{1}{a}(y(x)+\eta_p(y(x)))\right)=\frac{1}{a}y(x)+\frac{1}{a}E\left(\eta_p(y(x))\right)=\frac{1}{a}y(x), \tag{3.6}$$

and the right side of the equation (3.5) can be expressed as [65]

$$\mathrm{var}\left(\frac{1}{a}(y(x)+\eta_p(y(x)))\right)=\frac{1}{a^2}\mathrm{var}(\eta_p(y(x)))=\frac{1}{a}y(x). \tag{3.7}$$

Therefore, these relations can be obtained

$$E\left(\eta_p(y(x))\right)=0, \qquad \mathrm{var}(\eta_p(y(x)))=ay(x). \tag{3.8}$$

The equation for variance proved, that η_p has varying variance depending on the value of $y(x)$. Therefore, the overall variance of z can be written as [64]

$$\sigma^2(y(x))=ay(x)+b. \tag{3.9}$$

This is a very straightforward formula. From the theoretical point of view, this formula gives the behavior of the noise depending on the signal. For example, when the signal is zero, the variance is $\sigma^2(0)=b$, so only the signal-independent noise caused by the detector and hardware is present. On the other hand, when the signal approaches the value 1 as the largest value of a pixel, the variance is $\sigma^2(1)=a+b$, so these pixels are affected by both noises.

From the practical point of view, the Poisson distribution can be approximated with the Gaussian distribution (see section 2.2.4). This approximation is accurate for a large number of detected photons [64]. In the previous section there is shown, that with exposure times higher than 1 second, the approximation can be used. So overall the noise in the images can be modeled with normal distribution, such as

$$\eta_h(x)\sim\mathcal{N}(0,ay(x)+b). \tag{3.10}$$

When comparing the variance of the obtained distribution $\sigma^2=ay(x)+b$ and the variance 3.1 derived from statistical description, there are certain dissimilarities. In the estimated variance the b is negative, which means that based on the earlier statements, the variance in a dark frame (an image captured in complete darkness, where $y(x)=0$) would be also negative. Since the variance is always positive, this result would not make any sense. However, in real life, the model in equation (3.10) is not accurate and the digital imaging sensor's hardware must be taken into consideration – especially the so-called *pedestal parameter*. The charge, that is collected by the sensor is not processed as it is but is always added to some „pedestal" level $p_0\in\mathbb{R}^+$. This characteristic can be mathematically expressed as a shift representing an offset-from-zero in the argument of the signal-dependent part of the noise [64]

$$z(x)=y(x)+\sigma(y(x)-p_0)\xi(x)=y(x)+\eta_p(y(x)-p_0)+\eta_G. \tag{3.11}$$

[3] $E(X+Y)=E(X)+E(Y), \quad E(a)=a, \quad \mathrm{var}(a+bY)=b^2\,\mathrm{var}(Y), \; a,b\in\mathbb{R}$

With the definition of the pedestal parameter in place, the variance can be rewritten (in a simplified way) to

$$\sigma^2(y(x)) = ay(x) + b - ap_0. \tag{3.12}$$

Note that the signal-independent part can be negative when there is a big pedestal p_0.

For evaluation of the lowest captured signal possible, therefore for validating the existence of pedestal parameter, the dark frames will be analyzed. The mean value of the signal in the dark frame for the Cu target is 0.0649 and in the dark frame for the Mo target it is 0.0648. Therefore, the mean values in dark frames are independent of the target material. Practically, this value corresponds to the pedestal parameter itself – the lowest signal that can be captured.

Since the noise according to the noise model will be simulated in artificial images, the pedestal value should be added to the pixel values in the images to prevent the negative variance for some pixels. So overall, the noise variance can be modeled as

$$\sigma^2(y(x)) = (3.17 \cdot 10^{-5} y(x) + 0.06) - 1.85 \cdot 10^{-6}, \tag{3.13}$$

corresponding to the signal-dependent mixed Poisson-Gaussian distribution. The appearance of the noise is shown in figure 3.6.

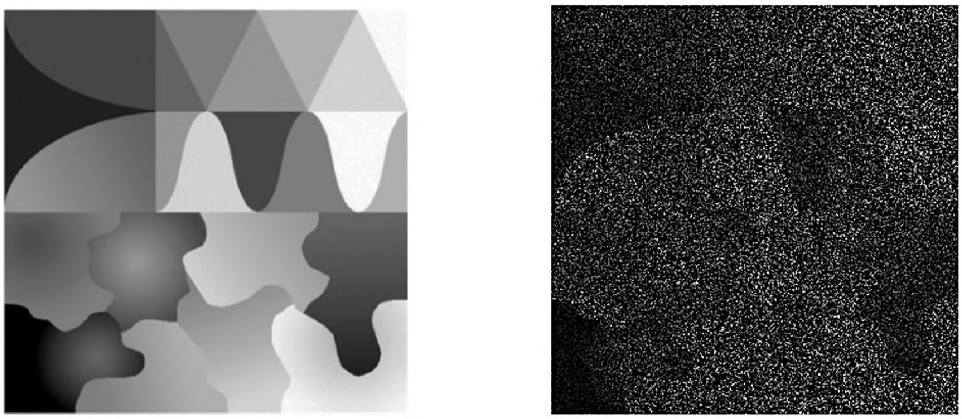

(a) (b)

Figure 3.6: An example of an image with simulated noise according to the noise variance model (a) and the noise added to the image (b). The noise-free image is adapted from [64].

Noise model validation

For validation of the determined noise model, the comparison between the real noise present in the bright field images and simulated noise according to the noise variance model will be performed. For that purpose, in each mean frame (in which the noise is considered to be reduced) the artificial noise was simulated using the formula (3.1). Afterward, the mean frame was subtracted for obtaining only the simulated noise values and variance was calculated. The differences between the noise variance of the artificial noise and the noise variance determined in the statistical analysis are very small – the largest difference is $7.46 \cdot 10^{-8}$.

For comparing the appearance of the simulated and measured noise, a vertical stripe from the middle of each noise matrix was taken and placed in the final noise image. These

stripes were arranged in the image according to the exposure time – from lower to higher. This way a noise image, which contains contributors for each exposure time was generated. One image was generated for simulated noise (fig. 3.7 (b)) and one for measured noise (fig. 3.7 (a)). These two noise images were compared in line-profile plots (fig. 3.7 (c)) going through the middle of both images.

Upon closer inspection of the measured noise in figure 3.7 (a) and simulated noise in 3.7 (b) it can be concluded that the measured noise is slightly stronger although the variances are similar. Subjectively in the measured noise data, clusters of brighter and darker pixels appear creating a pattern. This indicates potential detector sensitivity or hardware imperfections. The artificial noise has a perfect normal distribution and these influences are neglected. Since the noise is randomly distributed, the profile plots in the figure 3.7 (c) are not identical, but simultaneous changes are visible in the noise standard deviations.

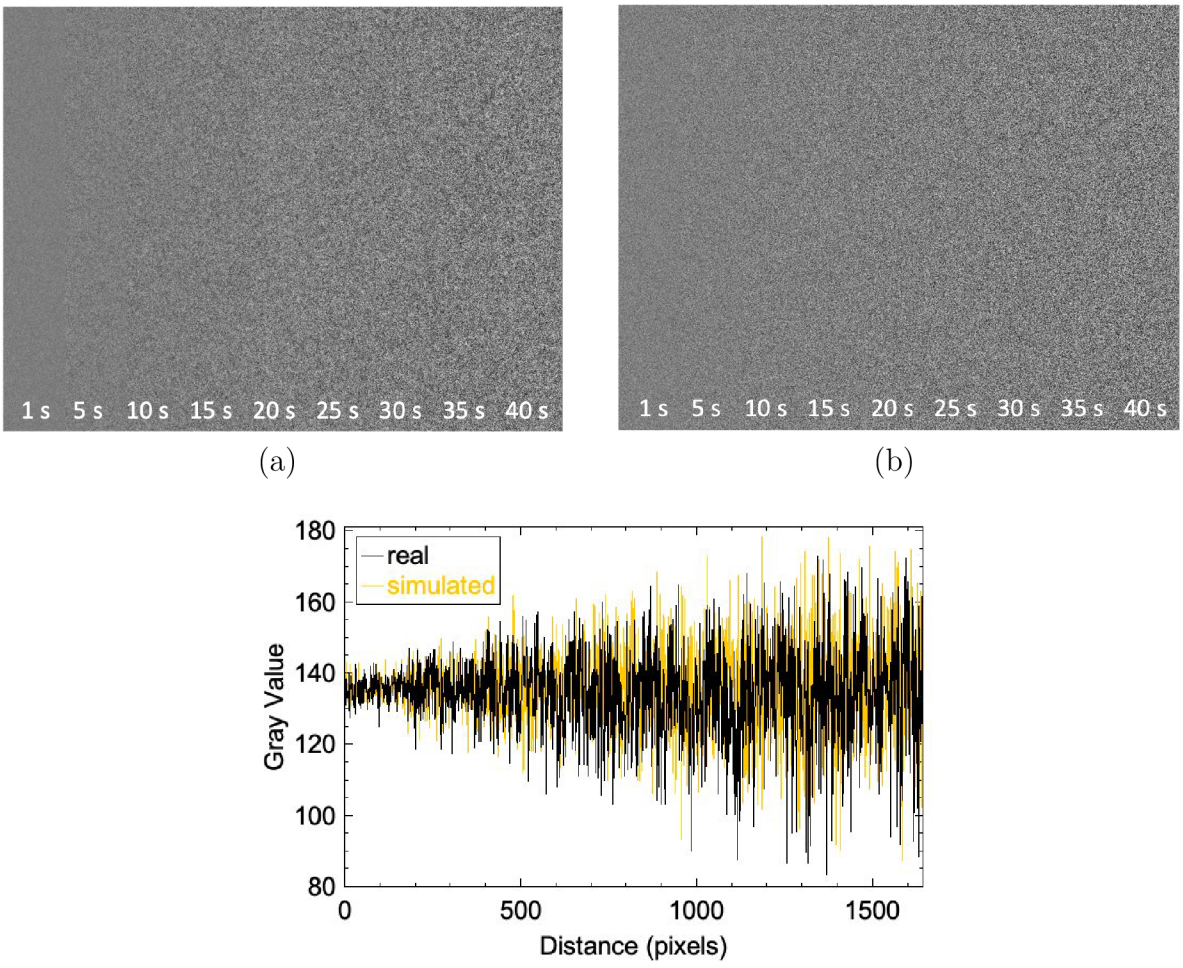

Figure 3.7: A noise image generated using noise data from measured bright frames (a) and noise image of simulated noise (b) for each exposure time, (c) profile plot of lines going through the middle of the images (a) and (b).

4. Noise reduction approaches in computed tomography

As mentioned earlier, noise is a constant factor in every measurement and can introduce challenges in interpreting reconstructed images. Hence, it becomes essential to employ effective techniques and strategies for noise reduction in CT imaging. These methods are crucial for improving image quality, and clarity of details, and enabling further processing such as segmentation.

The denoising methods used in the computed tomography process can be divided into three large groups [66]:

- projection-based methods,
- reconstruction-based methods,
- tomogram-based methods.

The projection domain-based methods are performed on the raw projection data or sinogram, so the denoised images enter the reconstruction process. This approach can be beneficial since the noise variance model is known and the denoising algorithms adapt according to it. However, in projections, there is usually not very high contrast, especially when low-attenuating samples are measured (see figure 4.1). With a lack of sharp transitions between different materials and soft tissues, the algorithms may produce images with blurred edges and details.

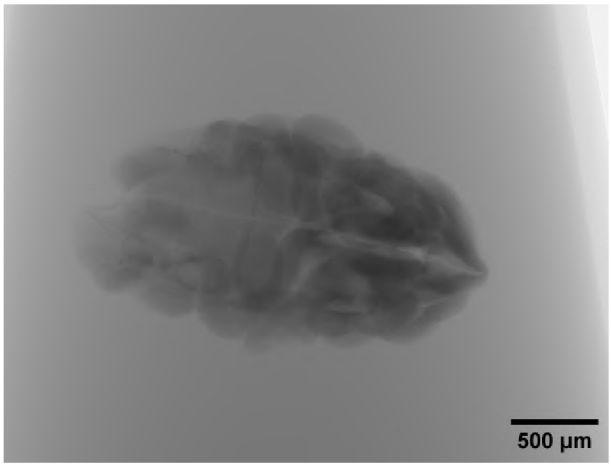

Figure 4.1: An example of a projection image of a mouse embryo sample from Rigaku nano3DX.

The methods in the second group mainly refer to the regularised iterative reconstruction techniques. The use of noise statistics directly in projections throughout the reconstruction process is a benefit of these approaches, however, the cost of computing is a serious drawback.

Tomogram domain denoising methods operate directly on the final reconstructed slices. Some of these methods can reduce the noise effectively while preserving edges and spatial resolution and improving the overall image quality. But on the other hand, they can lead to the enhancement of artifacts (such as ring artifacts) and to introducing blocking artifacts and further imperfections due to the non-stationarity of the noise [66], [67].

Authors are usually focusing on just one domain, where they perform denoising, but no comprehensive study on comparison of these approaches has been done and this is another goal of the thesis. The focus is on the comparison of projection-based denoising and tomogram-based denoising.

The experiment consists of several stages. First, selected algorithms are tested on simulated projections of an artificial phantom. The same algorithms are then used for denoising in the tomogram domain of the phantom. All results are compared after reconstruction in the tomogram domain, both subjectively and objectively, through visual inspection and image quality metrics. From each domain, the best approaches are selected and tested on the measured submicron CT datasets from Rigaku nano3DX.

The algorithms, that are used in this experiment, were selected based on the literature review in the section 2.3. From each group, a representative/representatives were chosen, mainly based on their popularity or potential for noise reduction while preserving edges, details, and spatial resolution. In high-resolution CT data, the preservation of these characteristics is crucial. The tested algorithms, that work with two-dimensional data are the wiener filter, median filter, non-local means filter, Split Bregman-ROF method [68], wavelet filter, SA-DCT method [69], and BM3D [70]. Also, algorithms for three-dimensional datasets are tested – median for 3D data, non-local means for volumetric data [38], CANDLE method [39], and BM4D [70]. The wiener filter, median filter, non-local means method, and wavelet filter are implemented directly in MATLAB. Additionally, this chapter covers short introductions to the selected algorithms, software packages for CT reconstruction, and metrics, that are used for objective evaluation of the algorithms' performances.

4.1. Introduction to selected denoising algorithms

In this section, the basic ideas behind each selected algorithm are discussed. A short introduction can be found in the section 2.3, but here the principles are described in more detail to understand the differences between the algorithms.

The Wiener filter is the first algorithm, that belongs to the spatial domain filtering – the method works directly with the image matrix. The Wiener filter is an adaptive linear filter minimizing the mean square error (MSE) between the estimated image and the input image in a least-squares sense. It takes into account both the statistical properties of the signal and the noise and it estimates the denoised image as a linear combination of these properties satisfying the minimal MSE [71].

Another filter, that works in the spatial domain, is the median filter. The basic principle of this filter is described in the section 2.3. This algorithm can be easily extended to the third dimension – the window is considered to be a cube.

The next method is the non-local means filter. This method is more complex. A window of a certain size is centered on each pixel in the image. Then, the pixel values within an examined window are compared to the pixel values in other windows located elsewhere in the image. The similarity between the windows is computed using a distance metric, such as the Euclidean distance. The most similar windows are used for calculating the weighted average, with weights according to the level of similarity. Finally, the filter replaces the center pixel within the examined window with the averaged value [34].

The extension of the non-local means algorithm for the 3D datasets is included in the testing. This method uses 3D windows – voxels to compute the weights. Because the datasets for processing are usually very large, some simplifications needed to be adapted in the filter. These simplifications mainly relate to the approximation of the Euclidean distance, preselection of the voxels for computation of weights, or blockwise computation [38].

The CANDLE algorithm is the last one from the spatial domain denoising group. The first step in this method is to perform Anscombe variance stabilization on two images – the original input image and the input image after median denoising. The main procedure of the method is based on the non-local means for 3D datasets, but it uses the denoised image by median filtering for computing the similarity between the patches instead of the noisy image. After processing each pixel, the inverse Anscombe transform is performed to get the result [39].

The only representative from the group of methods based on the total variation is the Split Bregman ROF method. It is a variation of the Rudin-Osher-Fatemi (ROF) model, which is based on total variation (TV) regularization. The Split Bregman-ROF method works by minimizing an objective function containing the denoised image, the noisy image, the total variation of the denoised image, and the regularization parameter that controls the trade-off between the data fidelity term and the total variation term. The TV term in the minimization suppresses the oscillations of the solution, but it does allow the solution to have discontinuities. Split Bregman is one of the efficient solutions to this minimization problem with the total variation. The solution is based on the iterative Bregman method [68].

Next are the transform-based methods, and the first representative is the wavelet filter. The wavelet filter works by first decomposing the image into different frequency sub-bands using a wavelet transform through the use of the basis function. The wavelet transform is a mathematical operation (similar to the Fourier transform) that breaks down an image into different frequency components at different scales. The high-frequency sub-bands correspond to image details, while the low-frequency sub-bands correspond to the overall image structure. The noise components are identified, thresholding to the coefficients in each sub-band to remove the noise is performed to suppress the noise, and the signal is reconstructed [72].

The Shape-Adaptive DCT (SA-DCT) method uses another famous operation – the discrete cosine transform. This transform is used for computing a sparse representation of image blocks and can be used for denoising, but usually fails to restore image edges and details. The method SA-DCT was developed as a solution to this problem. The algorithm works by first dividing the noisy image into overlapping patches. However, unlike the traditional DCT denoising method, the SA-DCT method uses a different set of basis functions for each block based on the local image structure. The basis is obtained by analyzing the gradient of the image in a window surrounding the patch. Once the shape-adaptive DCT is computed for each patch, a thresholding operation is applied to the coefficients in the spectra to remove the noise. The threshold is adaptively chosen for each coefficient based on a noise estimate derived from the noisy image. The denoised image is obtained by taking the inverse shape-adaptive DCT of the thresholded coefficients for each patch and merging the patches to form the final image [47].

Another transform-based method is the BM3D – Block Matching and 3D Filtering. The first stage of the process is similar to the non-local means algorithm. The image is

divided into small overlapping blocks, which are then compared to each other using some similarity metrics, usually the mean squared error or Euclidean distance. After identifying the group of similar blocks, the 3D transform is applied. The transform results in a 3D signal, that contains information about both the spatial and inter-block similarities. The spectrum is highly sparse, allowing clear separation between the noise and the signal. A thresholding operation (soft and hard thresholding, or Wiener filtering) is performed on the spectrum to suppress the noise, and the modified signal is transformed back by inverse 3D transform [48].

In the method BM4D, the principle stays the same, but the overlapping blocks are cubes of voxels. These cubes are stacked in a 4D group and the 4D transform is applied. The transformation leads to a highly sparse spectrum, where the noise and the signal can be separated, either by thresholding or Wiener filtering. Then the 4D inverse transform is performed to get the denoised dataset [52].

4.2. Software packages for tomographic reconstruction

Although the mathematical basics for both analytical and iterative reconstruction methods are very straightforward (see section 1.4), their computer implementation brings many challenges and is not always easy. Fortunately, numerous commercially available software packages are developed providing a wide range of implemented algorithms from which a user can select. The user only sets the parameters of these algorithms, which carry out the computation internally [73].

Maybe one of the most popular packages is the *All Scale Tomographic Reconstruction Antwerp (ASTRA) Toolbox*. It is a platform developed jointly at the University of Antwerp in Belgium and the Centrum Wiskunde Informatica (CWI) in Amsterdam. The majority of the package is written in C++ and the CUDA language is used to offload the most computationally demanding tasks to the GPU (Graphic Processing Units) card. The GPU provides acceleration of the calculations. The user has access to the package easily through MATLAB and a Python interface [73]. For all reconstruction in this work, only the ASTRA Toolbox in MATLAB is used.

ASTRA Toolbox is flexible, efficient, and easy to use. It is mainly developed for research purposes – it supports various non-conventional beam geometries, modeling misalignments, or multi-directional tilt series. The projections or volume data need to be stored in data objects within the toolbox in order to perform calculations on this data. First, the memory needs to be allocated for the input dataset and then it is copied from the user layer to lower layers within the toolbox. Every such procedure returns a special identifier or handler, that refers to the data. The information about the corresponding scanning geometry of the system is linked to these data objects. The volume geometry sets the voxel grid for the reconstruction. The projection geometry represents the positions of the X-ray source and detector relative to the volume geometry. In the projection geometry, the information about the size and number of pixels in the detector are involved, as well as the geometry of the beam. Standard geometries implemented in the Toolbox are the parallel beam and fan beam for 2D geometry, and the parallel beam and cone beam for 3D (see section 1.3). However, flexible geometries are available in the Toolbox. The user can specify an unusual geometry using a series of vectors – this is called vector-based geometry [73], [74].

A wide range of reconstruction algorithms is available within the Toolbox. It offers analytical reconstruction methods – FBP for parallel and fan-beam geometry, FDK for cone geometry, and some iterative reconstruction techniques – ART, SART, SIRT, and CGLS. The configuration of the algorithms can be done by linking the identifiers of the geometries and data, and by the configuration of the algorithm's specific parameters (filter for FBP and FDK, number of iterations for iterative techniques) [73], [74].

ASTRA Toolbox can be also coupled to other software packages. An example of this inclusion is the TomoPy software package. It combines a powerful reconstruction using ASTRA Toolbox with the complex and user-friendly pre-processing and post-processing methods [75].

4.3. Metrics used for evaluation

To get relevant and comparable results from the testing of denoising algorithms, some quality assessment of the final images is needed. The quality assessment methods can be divided into two groups: subjective and objective methods. The first group requires human observers in the evaluation process and since they are the final users, this image quality assessment is the most reliable and accurate. On the other hand, it is very slow, expensive, impractical, and highly dependent on the observer. Therefore, it is beneficial to develop objective methods – usually mathematical models, that can substitute the human factor in the process but predicts the evaluation in agreement with the subjective method. The objective methods can be further divided based on the availability of a reference image (an image without any distortions) into three groups:

- full-reference metrics,
- reduced-reference metrics,
- no-reference metrics.

For the full-reference quality assessment, the whole reference image is needed. For the reduced-reference metrics, only partial information about the reference image is available and as the name suggests, the third category refers to methods, where the reference image is not accessible. These methods are highly useful in practice since the distortion-free image doesn't always exist in many real-life applications [76], [77].

In this section, some metrics relevant to the assessment of the final images are introduced as well as their usage, advantages, and drawbacks. From the group of FR metrics, it is – structural similarity index (SSIM), mean squared error (MSE), and peak-signal-to-noise ratio (PSNR). In addition to these three metrics, the metric for assessment of segmentation – the Dice similarity coefficient will be introduced.

4.3.1. Full-reference metrics

As stated before, the methods in this group are based on the comparison between the perfect distortion-free reference image and the evaluated image. These methods usually use mathematical models and formulas, that are fast and easy to understand, compute and implement. The three metrics discussed here - SSIM, MSE, and PSNR, are well-known and well-established in the topic of image processing. MSE and PSNR operate

only with the intensities of the pixels, on the other hand, SSIM is a higher-level metric, which compares the overall similarity between the images. Therefore, each metric captures different aspects of image accuracy and perceptual similarity. By combining these metrics, the evaluation of noise reduction techniques can be made from different perspectives.

Mean squared error (MSE)

The mean square error is a simple metric, that estimates, how different is the test image from the reference one – it provides a measure of overall pixel-level distortion. The formula is very easy – it is averaged squared difference between the test image $\hat{f}$ and the reference image f, both sized $M \times N$ and can be expressed as [76]

$$\mathrm{MSE} = \frac{1}{MN} \sum_{y=1}^{y=M} \sum_{x=1}^{x=N} \left(\hat{f}(x,y) - f(x,y) \right)^2 . \tag{4.1}$$

The lower the MSE value, the closer is the test image to the reference one. The ideal value would be zero.

Even though the MSE is a popular and well-established metric, it has some disadvantages, that need to be acknowledged. Since it is a metric based on pixel-wise differences, it can lead to a lack of perceptual relevance. Also, it is very sensitive to outliers, meaning that a few pixels that have a much larger difference than the others can have a disproportionate impact on the MSE, making it less useful as a measure of overall image quality [76]. However, the MSE value is very simple to interpret but usually, other metrics are needed in addition to MSE to fully evaluate image quality.

Peak-signal-to-noise ratio (PSNR)

The PSNR is another commonly used metric for evaluating the quality of degraded images and quantifying the amount of noise present. It measures the ratio between the maximum possible power of a signal (the "peak signal") and the power of the signal's noise (the difference between the original and the compressed or degraded signal). It can be expressed mathematically as [76]

$$\mathrm{PSNR} = 10 \log \left(\frac{P^2}{\mathrm{MSE}} \right) , \tag{4.2}$$

where P is the maximum possible pixel value of the distorted image. It is calculated in decibels. The higher the PSNR, the better the quality of the distorted image.

Unlike the MSE, the PSNR doesn't depend on the intensity range of the image. It is a relative metric – it can be compared across different datasets. The disadvantages of PSNR are similar to the ones discussed in the case of MSE, but PSNR is considered to be a better indicator of the perceived quality of an image [77].

Structural similarity index (SSIM)

This metric is much more complex than the MSE and PSNR. SSIM is a perceptual-based metric considering the structural changes in the distorted image. It is designed to measure the structural similarity between two images, taking into account both the

luminance (brightness) and contrast of the images, as well as their structure (edges and texture). The formula is given as [78]

$$\mathrm{SSIM}(\hat{f}, f) = \frac{(2\mu_{\hat{f}}\mu_f + C_1)(2\sigma_{\hat{f}f} + C_2)}{(\mu_{\hat{f}}^2 + \mu_f^2 + C_1)(\sigma_{\hat{f}}^2 + \sigma_f^2 + C_2)}, \tag{4.3}$$

where the $\mu_{\hat{f}}, \mu_f$ are mean values of signals $\hat{f}$ and f, $\sigma_{\hat{f}}, \sigma_f$ are standard deviation and $\sigma_{\hat{f}f}$ is a covariance of the pixel values of the signals. The constants C_1 and C_2 are small positive numbers for stabilization. The SSIM index is bounded and the maximum value 1 is achieved only if $\hat{f} = f$.

The SSIM is more sensitive to human perception of image quality than metrics such as MSE and PSNR, and can better evaluate subtle differences in image structure and texture, but can be computationally demanding when large datasets are compared [76], [77].

Dice similarity coefficient

The Dice similarity coefficient is a statistical method used to compare the similarity or dissimilarity between two sets of data. Usually, the performance of segmentation algorithms can be evaluated – the similarity of two binary images is being compared. The Dice similarity coefficient (DSC) measures the spatial overlap and the formula can be expressed as [79]

$$\mathrm{DSC}(\hat{F}, F) = \frac{2(\hat{F} \cap F)}{\hat{F} + F}, \tag{4.4}$$

where $\hat{F}, F$ are two binary images being compared. The coefficient ranges from 0 to 1, where 0 means no similarity and 1 means a perfect match. A value of 0.5 indicates a 50% overlap between the two sets [79].

4.4. Phantom denoising

The first stage of this experiment is focused on the artificial phantom dataset - foam phantom [80]. The phantom dataset consists of a cylinder made of a single material with many non-overlapping spheres inside made of other materials. This dataset was chosen, because it offers many advantages. One of the advantages is that the phantom consists of many features, which makes the dataset challenging for obtaining exact reconstruction and can be a good representative of real-life samples (see fig. 4.2). The phantom dataset can be modified according to the user's needs – a custom number of projections, width, and height of the projections, or the difficulty of the phantom in terms of the number of spheres generated inside of the cylinder [80].

Using a simulated dataset offers the advantage of evaluating the tested denoising algorithms on simulated noise and comparing the results to ground truth using full-reference metrics. This allows a proper comparison of approaches for noise reduction in both projection and tomogram domains.

For this task, a foam phantom dataset of 360 projections sized 512 px × 512 px was generated. A slice of the ground truth volume of the cylinder is shown in figure 4.3 (a). The generated noise-free projections were reconstructed using the FBP reconstruction algorithm from the ASTRA Toolbox with the Ram-Lak filter and the corresponding slice

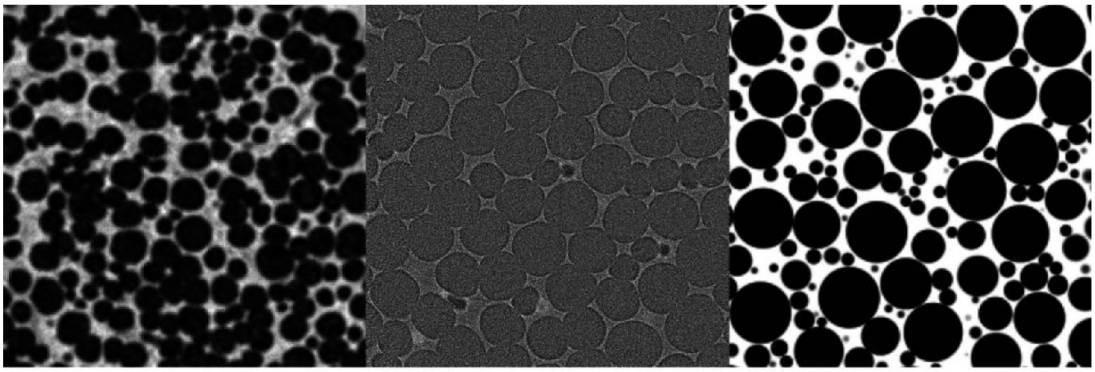

Figure 4.2: Examples of tomograms of foam-like real samples on the left and middle image, the generated foam phantom on the right image. Adapted from [80].

is shown in figure 4.3 (b). The reconstruction itself changed the appearance of the slice – the contrast is decreased, and some features (red arrows in the figure 4.3 (a), (b)) are lost. There are also visible typical artifacts from analytical reconstruction, such as streak-like artifacts on the edges of the image and noise.

For testing of the denoising algorithms, artificial noise was generated in the projection domain in two levels – a lower level of noise, which was generated according to the noise variance model (3.13) described in the previous chapter, and a higher level of noise, where the noise variance was additionally multiplied 10 times. The higher level of noise corresponds to a non-ideal measurement or the influence of the molybdenum target. By denoising of the higher level noise, the robustness and complexity of the algorithms and the range of their usage can be tested. The reconstructed slices from both sets of noisy projections using the FBP algorithm are shown in figure 4.3 (c), (d).

As stated in the introduction to this chapter, first, the denoising algorithms are tested on the projections of both noisy datasets. The algorithms are evaluated based on full-reference metrics, time duration, subjective evaluation, and line-profile plots. The metrics used for the comparison are SSIM, PSNR, MSE and Dice similarity coefficient (DSC). The same procedure is repeated in the tomogram domain. In both domains, the metrics are evaluated in the tomograms with the ground truth volume as a reference to get comparable results.

4.4.1. Denoising in the projection domain

The denoising in the projection domain is straightforward because the noise distribution and variance model are known, making it easy to set the algorithms' parameters. Although the noise is signal-dependent, and the variance changes throughout each projection, the changes are not significant in the region of interest (ROI) of the sample. Therefore, algorithms should work efficiently without requiring additional pre-processing.

Each of the selected algorithms has various parameters that can be adjusted to maximize their performance. The following methods have the noise variance or standard deviation as part of their settings: Wiener filter, non-local means (nlm), SA-DCT, BM3D, BM4D, CANDLE, and non-local means 3D (NLM3D). The universal optimal parameters for both noise levels were determined so that the full reference metrics would produce the best results with noise-free projections as a reference. These parameters are presented

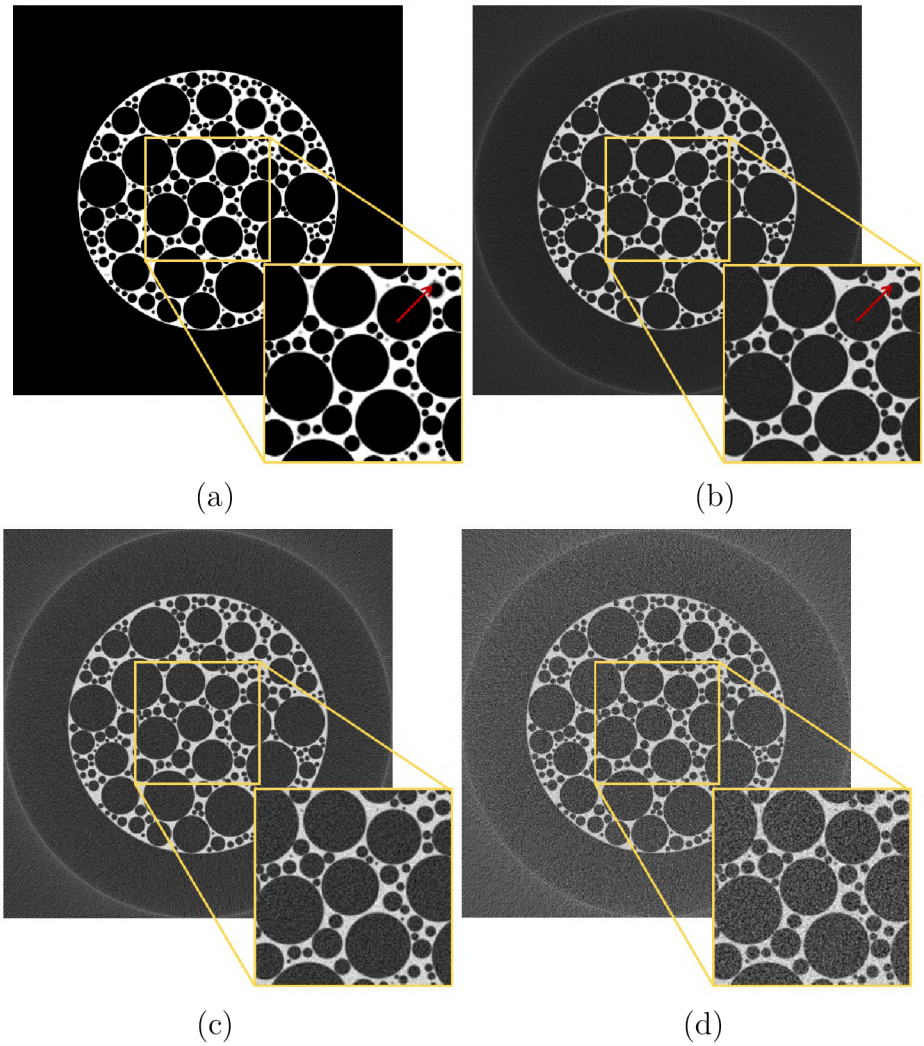

Figure 4.3: A slice of the ground truth volume of the foam phantom dataset (a), a corresponding reconstructed slice using FBP reconstruction algorithm from noise-free projections (b), a reconstructed slice using FBP algorithm from projections with generated artificial noise according to the noise variance model (c), a reconstructed slice using FBP algorithm from projections with generated noise according to the noise model multiplied by 10 (d). Central regions of the images are zoomed in.

in Appendix B. The parameters remain the same for both noisy datasets, with only the noise variance/standard deviation changing, as the sample itself is the same.

Once the most suitable parameters were found, the range of projections (generally the angle range) to be processed at once was established for the 3D algorithms. This was done similarly – the results were compared to the noise-free projections. The angle range for median filter was set to $\langle 0°, 60° \rangle$ and for the BM4D method it was $\langle 0°, 36° \rangle$. For CANDLE filtering, the whole dataset can be processed, since the algorithm has its internal function to divide the input 3D data into batches of 64 projections. The non-local means 3D method was applied to the full 180° angle range of projections, but it should be noted that memory issues may appear with larger datasets.

After applying denoising to each set of projections, the datasets were reconstructed using the FBP algorithm from the ASTRA Toolbox. The Ram-Lak filter was used in the reconstruction, so the noise in the reconstructed slices is not modified by the filter

in any way. Then, the reconstructed volume was compared to the ground-truth volume. The results of full-reference metrics are listed in Table 4.1. Furthermore, the outcomes of these metrics for the noisy datasets and the reconstruction from noise-free projections are also included in the table.

Section 1.5.2 describes how averaging of projections can be used in the projection domain to suppress noise. This approach is also employed in the testing to assess whether the software-based methods perform better in metrics or time duration. Two datasets of projections with different noise values were generated and averaged to create a final dataset. After averaging, this dataset was reconstructed and the slices were compared to the ground-truth volume. This was done for both noise levels. Additionally, the same procedure was done for three projections. The results of full-reference metrics are listed in the table 4.1 (2 proj., 3 proj.).

Table 4.1: Outcomes of full-reference metrics for denoising in the projection domain. The best results are highlighted in the table – blue for the lower noise level, and yellow for the higher noise level.

	SSIM		MSE		PSNR		DSC	
	Lower noise	Higher noise	Lower noise	Higher noise	Lower noise	Higher noise	Lower noise	Higher noise
noise-free	0.6133		0.0348		20.6044		0.9844	
noisy	0.5286	0.3942	0.0498	0.0939	19.0492	16.2950	0.9814	0.9626
2 proj.	0.5548	0.4417	0.0456	0.0758	19.4326	17.2220	0.9817	0.9679
3 proj.	0.5706	0.4714	0.0421	0.0657	19.7751	17.8452	0.9830	0.9748
wiener	0.5638	0.4213	0.0429	0.0820	19.6959	16.8809	0.9815	0.9631
median	0.5053	0.4255	0.0570	0.0809	18.4630	16.9410	0.9737	0.9573
nlm	0.5362	0.5080	0.0482	0.0558	19.1942	18.5551	0.9815	0.9625
SBROF	0.6262	0.4579	0.0334	0.0692	20.7804	17.6197	0.9743	0.9659
wavelet	0.6344	0.5799	0.0318	0.0413	20.9964	19.8593	0.9768	0.9540
SA-DCT	0.6449	0.5608	0.0301	0.0452	21.2350	19.4723	0.9805	0.9277
BM3D	0.5826	0.5771	0.0395	0.0414	20.0593	19.8462	0.9824	0.9620
median 3D	0.5357	0.3974	0.0489	0.0921	19.1281	16.3780	0.9749	0.9569
CANDLE	0.5589	0.4408	0.0442	0.0751	19.5607	17.2658	0.9805	0.9598
NLM3D	0.6029	0.5406	0.0369	0.0503	20.3515	19.0076	0.9778	0.9652
BM4D	0.5921	0.5912	0.0379	0.0406	20.2383	19.9314	0.9826	0.9646

In an ideal case, the metrics would have close or even better results than those obtained for reconstruction from noise-free projections. The best outcomes are highlighted in the table 4.1 – blue for lower noise, and yellow for higher noise. For each metric, the 4 best outcomes are highlighted. An important thing to notice is that with better metrics values, the Dice coefficient is lower and the other way around. This relationship is linked to the degree of noise suppression, where higher noise reduction tends to result in less sharp

edges. Thus, finding a compromise between the metrics and the Dice coefficient is crucial. Additionally, it is worth mentioning that the metrics align well with each other. That means, that each result image is consistent in all evaluated features – similarity, noise and distortions.

From the highlighted outcomes for lower noise it can be inferred that although the SBROF, wavelet, SA-DCT, and NLM3D methods yield excellent results, the edges appear blurred according to the Dice coefficient. The same observation can be made for the higher noise level – the wavelet filter and SA-DCT perform very well in terms of metrics, but the edges are blurred. For both datasets, the BM3D and BM4D methods are the best compromise between the metrics and Dice coefficient outcomes.

Another important thing to notice is, how the outcomes of the metrics for each algorithm changed with the higher noise. The smaller the differences, the more adaptable the algorithm is to various noise levels. The BM4D and BM3D methods have the smallest differences suggesting their capability to adapt to different measurements.

Even though the averaging of projections was able to improve the metrics' values, the software-based denoising results in better noise suppression according to the metrics. On the other hand, the averaging was able to increase the Dice coefficient, especially the averaging of 3 projections have superior outcomes compared to the software-based denoising. In conclusion, with higher noise in the projection domain, the averaging of three projections can be beneficial, especially when the sample's small features, edges, and details cannot be compromised in any way. However, the reconstructed slices may still be noisy as the improvement in metrics was not substantial.

The subjective evaluation of the reconstructed volumes after denoising is based on one slice from each dataset, in particular, zoomed regions of the slice are shown – the lower noise level denoising in figure 4.5, and higher noise denoising in figure 4.6. The selected regions for comparison are illustrated in figure 4.4. The sharpness of the edges is compared in line-profile plots in figures 4.7 (a), 4.7 (b). The line-profile plots are drawn along the green line in figure 4.4.

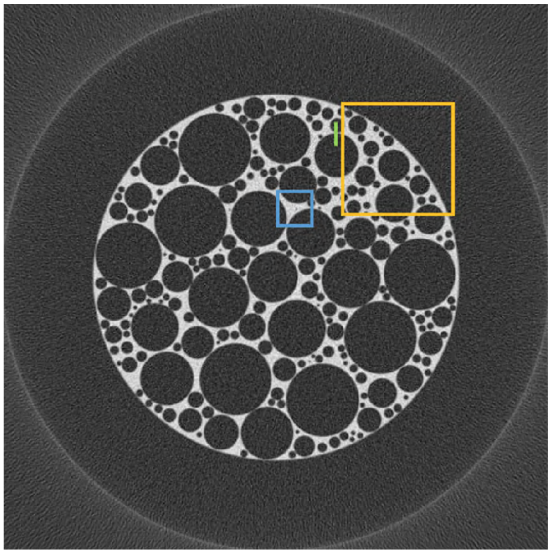

Figure 4.4: A noisy reconstructed slice with highlighted regions for analysis of algorithms' performances. The yellow and blue squares are used for subjective evaluation, the green line is used for line-profile comparison.

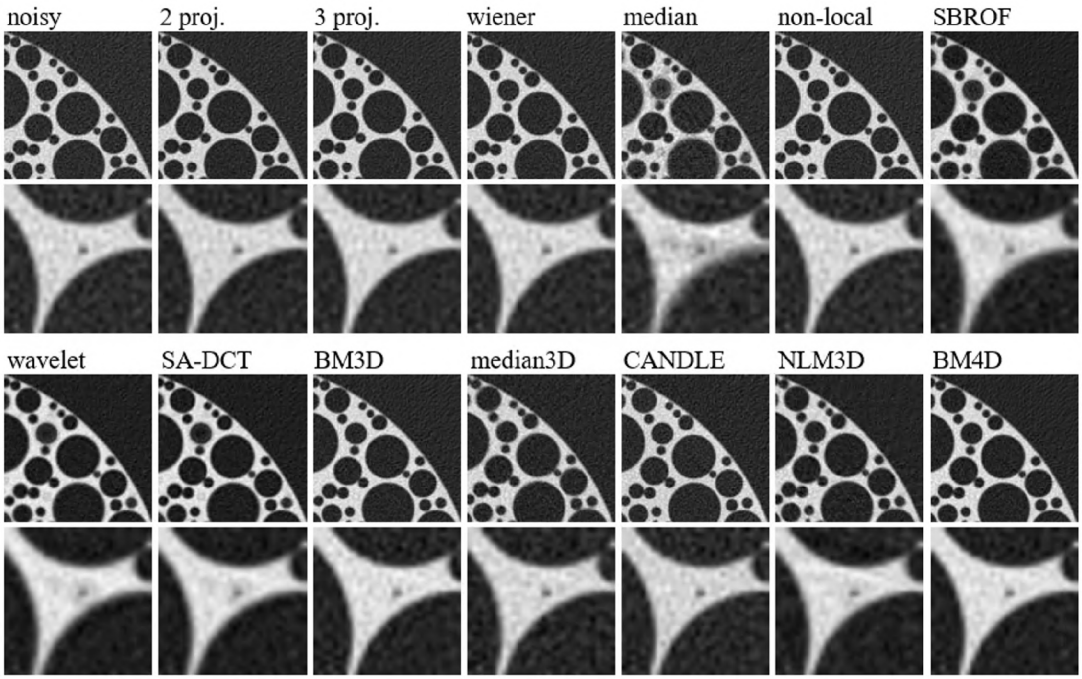

Figure 4.5: Zoomed selected regions from the reconstructed slices after denoising using tested algorithms in the projection domain with *lower* noise level. The regions are depicted in the figure 4.4.

First, the subjective evaluation of results in figure 4.5 for lower noise denoising is done. Upon closer inspection of the details in the second and fourth row, it can be stated that median, SBROF, wavelet, and SA-DCT filtering lead to the blurring of the dot. This blurriness can also be seen in the top row, where the edges of the circles are visibly blurred. The median filter is not suitable for denoising in the projection domain, since it generates new artifacts. Another thing that can be noticed is that median3D and NLM3D can preserve the dot detail very nicely, but the circles at the edge of the cylinder become slightly more blurred. Based on subjective evaluation, the BM3D and BM4D methods produce the best appearance in the zoomed regions. Wiener filter, non-local means filter and CANDLE also show good results.

The averaging of projections outcomes has a similar appearance to the noisy regions. For the outcome from averaging three projections, a small improvement in noise reduction can be observed.

The same discussion can be made also for the line-profile plot in figure 4.7 (a). The lines for the median, SBROF, SA-DCT, and wavelet filters don't reach high peaks indicating a reduced distinction between the circles. Other filters follow the line in the noisy slice, but BM3D and BM4D improved the contrast – the lines at the beginning and the end of the plot reach lower values. The NLM3D method exhibits the highest peak, indicating sharp transitions.

Figure 4.6 shows the same regions of the reconstructed slices after denoising of the higher noise level in the projection domain. It is apparent that the quality of the regions and details significantly decreased for all algorithms. The details of the dot in the second and fourth rows are mostly blurry, making it unrecognizable. However, the best distinguishment of the dot can be seen for the CANDLE, NLM3D, and BM4D methods. But for higher noise level denoising, the typical behavior of the 3D algorithms can be noticed

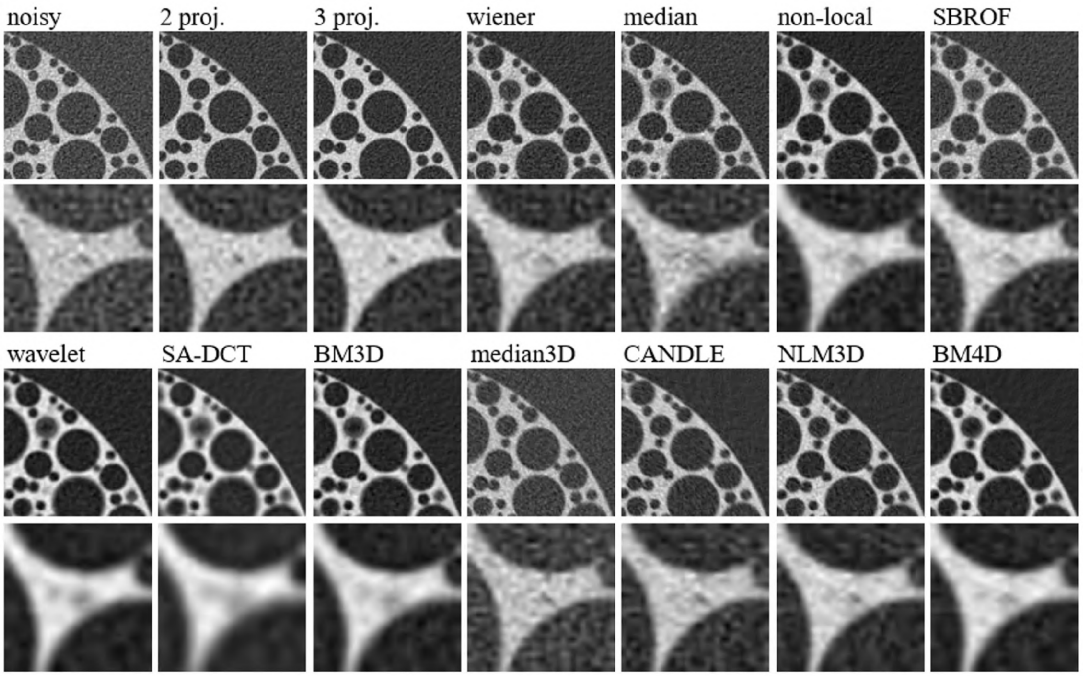

Figure 4.6: Zoomed selected regions from the reconstructed slices after denoising using tested algorithms in the projection domain with *higher* noise level. The regions are depicted in the figure 4.4.

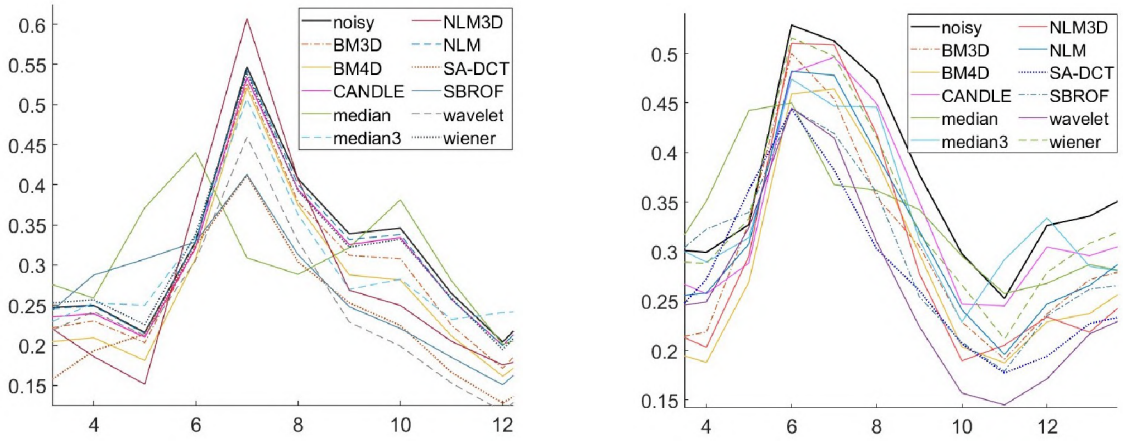

Figure 4.7: A line-profile plots comparing the edge sharpness in each reconstructed slice after denoising of the (a) *lower* noise level and (b) *higher* noise level in the projection domain. The profile plots are drawn along the green line in figure 4.4.

– the distance from the center of the ROI is connected to its blurriness. At the edges of the cylinder, the circles become notably more blurred, and streak-like artifacts can appear. None of the 2D algorithms was able to perform denoising without damaging the slice. The shape of the circles is compromised and the edges are blurred. The SBROF method preserves sharp edges the most, but the noise suppression is not satisfactory. The non-local means algorithm was able to suppress the noise quite effectively and the blurriness is not as significant as in other slices. The BM3D method can be considered a viable

option for denoising of higher-level noise, due to its effective noise suppression. However, the method may introduce some blurriness.

The best results from the subjective evaluation of the higher noise level denoising are for the averaging of projections. Here, the improvement of both the dot details and the noise suppression in the zoomed regions is significant compared to software-based denoising.

The line-profiles comparison in figure 4.7 (b) is not as straightforward as for the lower noise level, since the edges are more blurred. The worst in this comparison is the median filter and median 3D filter. The BM3D, non-local means filter (NLM), BM4D, and NLM3D have probably the best edge enhancement and contrast.

4.4.2. Denoising in the tomogram domain

As demonstrated, the noise in the projection images can be well described and its model can be estimated making it easy to simulate in the test projections. The same statements cannot be made for the noise in the tomogram domain. The noise model in the tomogram domain is very complex and hard to describe. After the FBP analytical reconstruction, the noise is generally non-stationary because the attenuation coefficient is varying along the line integrals [81]. This effect results in typical noise appearance in the reconstructed slices – in the center, the noise has an isotropic grain structure, and closer to the edges of the ROI the noise variance decreases and the noise becomes more oriented. This behavior of the noise is visible also in the simulated datasets (see figure 4.8). Although a variance stabilization transform could solve this issue, it is unnecessary since the noise remains approximately consistent and homogenous within the ROI. Therefore, denoising algorithms will be tested without any additional pre-processing.

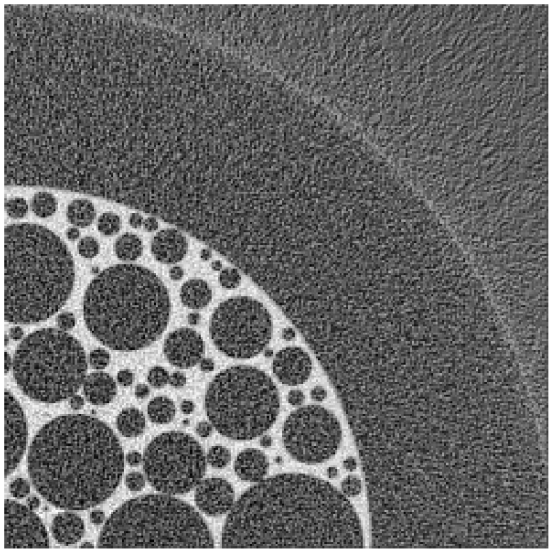

Figure 4.8: A slice of the higher noise level dataset demonstrating the typical behavior of the noise in the tomogram domain. The noise is non-stationary – the variance is decreasing with a higher distance from the center.

In this section, the selected denoising algorithms are directly used on the reconstructed slices of both noisy datasets – lower noise level and higher noise level. The noise estimation function introduced in [82] was adapted for the calculation of the noise standard deviation

in the ROI for setting this parameter to the methods. The search for universal optimal parameters for each algorithm and the range of projections for 3D algorithms was carried out in the same way as for the projection domain, with the ground-truth slices taken as a reference. For median filtering in the 3D and CANDLE method, the whole batch of 512 slices can be processed and for the BM4D method and non-local means in 3D, the dataset was divided into 4 batches of 128 slices. The optimal parameters used for denoising can be found in Appendix B.

After determining the optimal parameters, denoising was performed, and the entire volume was evaluated using full-reference metrics with the ground-truth volume as a reference. The evaluation of metrics for each method can be found in table 4.2.

Table 4.2: Metrics outcomes for denoising in the tomogram domain. The best results are highlighted in the table – blue for the lower noise level, and yellow for the higher noise level.

	SSIM		MSE		PSNR		DSC	
	Lower noise	Higher noise	Lower noise	Higher noise	Lower noise	Higher noise	Lower noise	Higher noise
noise-free	0.6133		0.0348		20.6044		0.9844	
noisy	0.5286	0.3942	0.0498	0.0939	19.0492	16.2950	0.9814	0.9626
wiener	0.5876	0.4187	0.0384	0.0830	20.1750	16.8314	0.9815	0.9658
median	0.6299	0.4703	0.0321	0.0664	20.9525	17.7961	0.9758	0.9603
nlm	0.5590	0.4517	0.0430	0.0710	19.6819	17.5066	0.9890	0.9704
SBROF	0.9552	0.6093	0.0040	0.0365	29.9633	20.4041	0.9734	0.9635
wavelet	0.6423	0.4856	0.0304	0.0615	21.1990	18.1311	0.9827	0.9693
SA-DCT	0.9699	0.9680	0.0055	0.0091	28.6099	26.4282	0.9814	0.9670
BM3D	0.6468	0.5282	0.0295	0.0499	21.3253	19.0411	0.9841	0.9708
median 3D	0.6074	0.4430	0.0356	0.0743	20.5041	17.3136	0.9766	0.9626
CANDLE	0.9520	0.9504	0.0185	0.0236	23.3576	22.2919	0.9813	0.9614
NLM3D	0.5286	0.3945	0.0498	0.0937	19.0491	16.3014	0.9814	0.9627
BM4D	0.6968	0.5887	0.0229	0.0382	22.4160	20.2058	0.9848	0.9754

The 4 best outcomes in the table are highlighted in the same way as in the previous section – blue color for the lower level of noise and yellow for the higher level of noise. It's important to note that the metrics outcomes are overall higher than for the denoising in the projection domain. This is because the methods suppress also the noise that arises during the reconstruction process, resulting in smoother regions. The trade-off between the full-reference metrics and the Dice coefficient must be considered – the higher noise suppression results in higher blurring of the edges and thus more uncertain segmentation. The same conclusion can be made regarding the alignment of methods for these outcomes, as for the projection domain. This suggest, that the amount of evaluated metrics could be reduced for future experiments with this phantom.

Methods SBROF, SA-DCT, CANDLE, and BM4D have the best outcomes in the table. The values are excellent, especially the SSIM results are very high. But on the other hand, only the BM4D was able to improve the values of the Dice coefficient significantly, suggesting the highest sharpness of the edges and shapes. Even though the metrics outcomes for the BM3D method are not as good as for the highlighted methods, it can also be considered a good compromise between the full-reference metrics and the Dice coefficient. The NLM3D method wasn't able to improve the metrics outcomes for the lower noise level dataset. There is only a slight improvement of the higher noise level dataset, suggesting that the NLM3D is not suitable for denoising in the tomogram domain.

Similarly, as in the previous section, the subjective evaluation of the outcomes will be done on the selected regions in figure 4.4. Only regions of one slice from each denoised dataset will be shown – the lower noise level denoising in figure 4.9 and the higher noise level in figure 4.10. The sharpness of the edges and edge enhancement will be compared in a line-profile plot in figures 4.11 (a) and (b). The line-profile plots are drawn along the green line in figure 4.4.

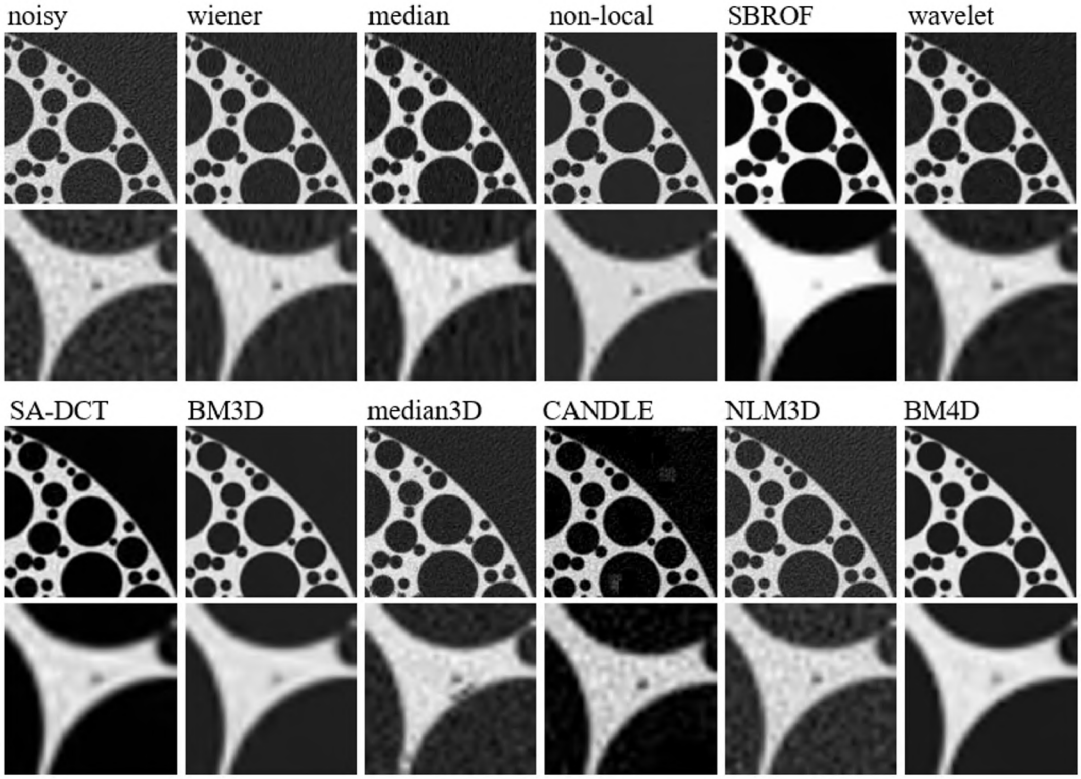

Figure 4.9: Zoomed selected regions from the reconstructed slices after denoising using tested algorithms in the tomograms with *lower* noise level. The regions are depicted in the figure 4.4.

At first sight at the results in figure 4.9, the difference between the tomogram domain and projection domain denoising is apparent. As previously mentioned, the algorithms in the tomogram domain tend to suppress the noise originating from the reconstruction process too, which results in images with overall lower noise levels. On the other hand, it should be noted that the algorithms can introduce new artifacts, such as visible blocks of pixels in the CANDLE slice.

The non-local means, SBROF, SA-DCT, BM3D, and BM4D methods show the highest noise suppression ability, while the wiener, median, and median 3D filters only slightly reduce the noise. The NLM3D method fails to change the slice significantly corresponding to the conclusions made based on metrics. The algorithms SBROF and SA-DCT improved the contrast significantly and the appearance of the slice is similar to the ground-truth slice (see figure 4.3 (a)) but in the SA-DCT slice an effect of blockiness can be noticed. The same effect is present also in the non-local means image, but here the blocks are mainly around the edges. Subjectively, the BM3D slice seems to be slightly blurred. The BM4D method performs the best in terms of noise reduction, artifacts, sharpness, and detail maintenance.

In the line-profile plot in figure 4.11 (a) the overlap of NLM3D and the noisy line is evident validating its poor performance. The SA-DCT and SBROF methods also suppress the grey level inside the spheres to the value of 0 and provide significant edge enhancement, with a difference of 0.4 between the lowest and highest point. The BM4D and BM3D methods can suppress the noise while maintaining sharp peaks. On the other hand, the median filter, median filter for 3D data, wiener filter, and non-local means (NLM) methods do not perform as well, with less sharp peaks and poorer noise suppression.

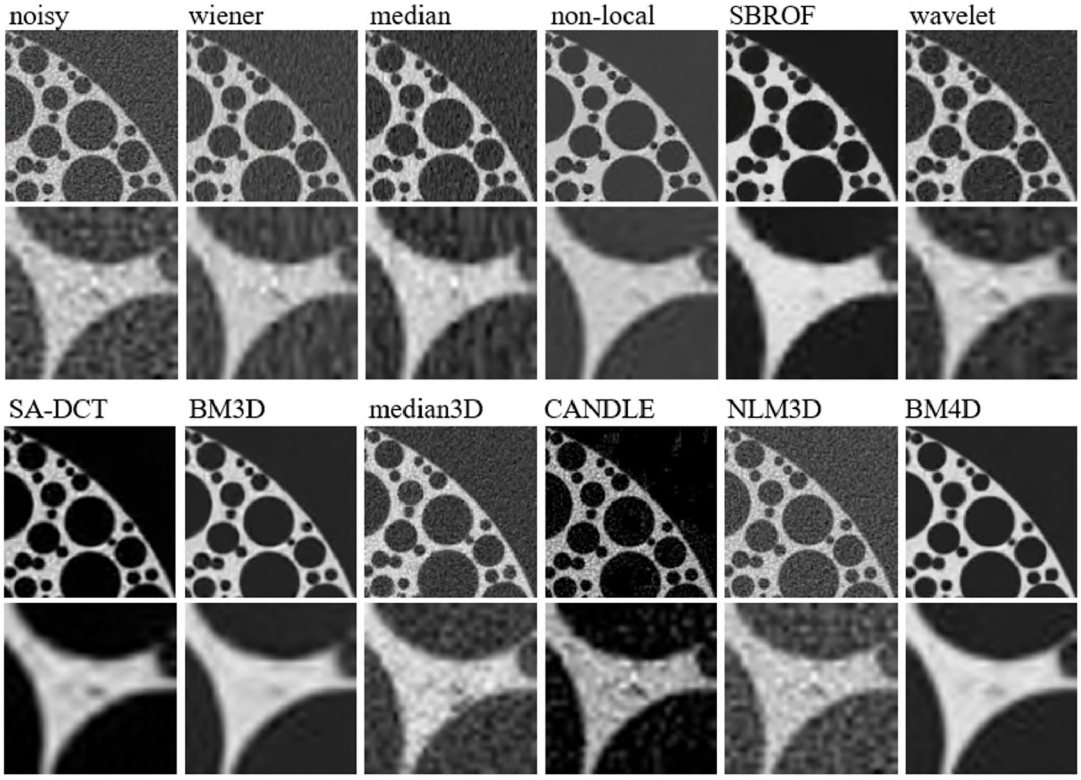

Figure 4.10: Zoomed selected regions from the reconstructed slices after denoising using tested algorithms in the tomograms with *higher* noise level. The regions are depicted in the figure 4.4.

As the noise level increases (fig. 4.10), the imperfections of the denoising algorithms become more visible, particularly in terms of blockiness and generation of new artifacts. The effect of blockiness is remarkably worse in the slices after denoising with CANDLE, SA-DCT, and non-local means methods. Also, some inconsistencies and flaws can be

noticed in the BM3D and SBROF slices. With the higher noise level, the quality of the BM4D slice decreased too, but the smoothness of the edges is superior to other methods.

Figure 4.11 (b) shows the comparison of edge enhancement in slices after denoising of the higher level of noise. The overlap between the line for the noisy slice and the NLM3D slice is visible again. The decrease of edge enhancement for SA-DCT and SBROF methods can be noticed, but still, the contrast and noise suppression are very good. The BM3D and BM4D lines exhibit similar performance. The median filter and median filter for 3D data fail to maintain the sharpness of the edge. The non-local means method was also able to suppress the noise quite well, but the contrast is decreased. The best edge enhancement from this comparison can be seen in the SA-DCT, BM3D, and BM4D slices.

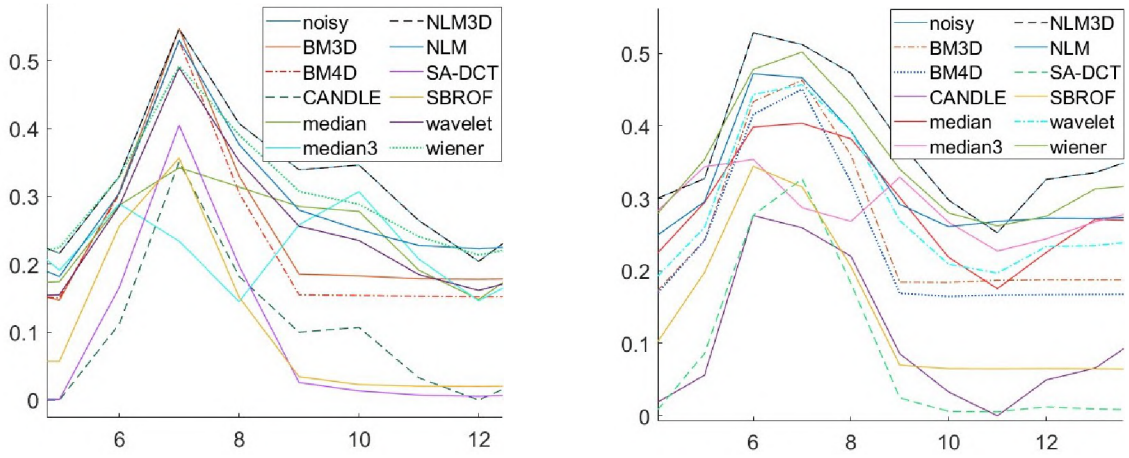

(a) (b)

Figure 4.11: A line-profile plots comparing the edge sharpness in each reconstructed slice after denoising of the (a) *lower* noise level and (b) *higher* noise level in the projection domain. The profile plots are drawn along the green line in figure 4.4.

4.4.3. Time duration

The time taken for denoising is an important factor to consider in the comparison of algorithms, especially in computed tomography where the datasets are usually large. To make denoising feasible, the processing time for each projection or slice must be as low as possible.

Table 4.3 shows the time required by each algorithm to process one image (either a projection or a slice) in the dataset. Whole datasets were processed – 360 projections and 512 tomograms. The time consumption of the algorithms is dependent on the size of the processed image and the chosen parameters. The images in the projection domain and the tomogram domain are of equal size (512 px × 512 px), but the parameters can significantly impact the processing time. This is especially true for the algorithms like non-local means, CANDLE, or NLM3D, where the sizes of windows for searching and comparison can affect the time notably. However, in the case of images sized 512 px × 512 px, the differences between domains in the case of non-local means and NLM3D are only fractions of a second and one second for the CANDLE method. Therefore, only the higher time from the domains is listed in the table. The computer used for this evaluation has a processor Intel i7 with 128 GB RAM. The most time-efficient algorithms are those implemented in MATLAB and have simple principles – wiener filter, median

Table 4.3: Time duration of each algorithm for processing one image.

algorithm	time per image [s]
wiener	0.006
median	0.005
nlm	0.551
SBROF	0.101
wavelet	1.244
SA-DCT	11.49
BM3D	11.30
median 3D	0.008
CANDLE	51.84
NLM3D	1.872
BM4D	10.67

filter, and median 3D. The non-local means filter is also not very time-consuming. Among the non-MATLAB algorithms, the SBROF method is the fastest. The processing time of one image for SA-DCT, BM3D, and BM4D filtering is nearly the same. However, when considering the number of images for processing (360 projections, 512 slices), the time required by these algorithms extends to over an hour. The worst in terms of time consumption is the CANDLE method making it impractical for denoising of CT data.

The averaging of projections cannot be included in table 4.3, since the time consumption of this approach is connected to the exposure time. But generally, the averaging of 2 projections increases the measurement time twice, and the 3 projections three times.

It is important to note, that the typical datasets from Rigaku Nano3DX are sized 1648 px × 1250 px × 800 projections, therefore, the processing times for real datasets will be significantly higher.

4.4.4. Discussion of the phantom denoising results

The reduction of noise in the projection domain can be very beneficial and has many advantages. The denoising is very subtle – the appearance and nature of the reconstructed slice are not changing dramatically, but the contrast can be improved. However, it is not effective in suppressing artifacts from reconstruction, such as noise and streak-like artifacts. So there will always be some residual noise left. The software-based denoising in the projections can lead to improvement in quality and good noise suppression with detail preservation, but only with a lower noise level. When the noise level is higher, the algorithms tend to blur the edges of objects and suppress details. The 3D algorithms, especially the NLM3D and BM4D methods have overall superior performance over most of the 2D algorithms. Still, with the higher noise level, the effect of blurriness of features further from the center of the sample appears and is a serious drawback.

Subjective evaluation and metrics should both be considered when deciding on the best approach for noise reduction. From the metrics comparison, the BM3D and BM4D are chosen as the best compromise between the metrics values and the Dice coefficient.

However, when dealing with the higher level of noise, the metrics outcomes are not accurate, since both the BM3D and BM4D slices are blurred. This indicates, that relying only on metrics outcomes is insufficient for evaluation of image quality. The non-local means algorithm could be a compromise between the subjective evaluation and metrics outcomes. But it is important to note, that the software-based denoising of the higher noise level in the projections is not ideal, and some information would probably get lost during the process.

The technique of averaging three projections has many benefits, especially when dealing with high levels of noise. It can reasonably suppress the noise and enhance the details in the reconstructed slices. Nevertheless, it is important to note that this method needs triple the measurement time, making it impractical in many situations. Additionally, it is a pre-measurement consideration and cannot be applied to previously obtained datasets. In summary, software-based denoising is a more universal approach with better outcomes.

The nature of denoising in the tomogram domain is completely different. The noise reduction is more efficient since it reduces the noise both from the measurement and reconstruction process. It increases the contrast of the slice and the results are closer to the ground-truth volume. The reduction of the higher level of noise is more effective. However, the technique can create new artifacts and flaws, such as blockiness, which can make the slice appear unnatural. Nevertheless, the denoising in this domain tends not to blur the edges of circles as much as in the projection domain, resulting in sharper transitions between spheres and the cylinder volume.

The metrics outcomes in the tomogram domain align more with subjective evaluations but don't take into consideration the blockiness, newly generated artifacts, or inconsistencies in the pixel values. The outcomes of the Dice coefficient are overall higher in the tomogram domain than in the projection domain, suggesting a larger potential for more reliable segmentation. Overall, the BM4D algorithm has superior performance in the tomogram domain denoising at both noise levels. It demonstrates great performance in terms of metrics, Dice coefficients, and subjective evaluation. The usage of the 3D method also resolves pixel inconsistencies and blockiness that may occur along the z axis between the slices. The SBROF algorithm can be considered as a viable option, but with higher noise levels the blockiness and pixel inconsistencies are significant.

A wide range of reconstruction algorithms is available within the Toolbox. It offers analytical reconstruction methods – FBP for parallel and fan-beam geometry, FDK for cone geometry, and some iterative reconstruction techniques – ART, SART, SIRT, and CGLS. The configuration of the algorithms can be done by linking the identifiers of the geometries and data, and by the configuration of the algorithm's specific parameters (filter for FBP and FDK, number of iterations for iterative techniques) [73], [74].

ASTRA Toolbox can be also coupled to other software packages. An example of this inclusion is the TomoPy software package. It combines a powerful reconstruction using ASTRA Toolbox with the complex and user-friendly pre-processing and post-processing methods [75].

In conclusion, in the projection domain, the BM3D and BM4D methods were selected as the best, but only for denoising of the lower level of noise. Their abilities to effectively reduce noise in the projections, improve contrast, and simultaneously preserve details and sharpness of edges were described. With the higher level of noise, the user needs to be aware of a certain amount of blur by using these methods. By reduction of noise in the projection domain, the slice will have a natural appearance, and increased contrast,

but some noise will be still present. In the tomogram domain, the BM4D method is considered to be the compromise between the performance in terms of metrics, blurriness, and generation of new artifacts.

However, the processing times of both the BM3D and BM4D methods listed in table 4.3 are quite high and with large datasets, the time consumption will increase. Such a slow noise reduction can be inconvenient in some industrial applications so a faster solution would be beneficial. In theory, the combination of noise reduction in both the projection and tomogram domains has the potential to produce high-quality results and potentially even up the performance of the best individual methods. In the projection domain, the non-local means filter is a suitable choice, as it effectively reduces noise while preserving the clarity of details. Once the denoised dataset is reconstructed, the non-local means algorithm can be applied again to further reduce residual noise. While it doesn't perform that well in the tomogram domain, it remains one of the best options in terms of processing speed and maintaining edge sharpness, as indicated by the Dice coefficient.

4.5. Measured dataset denoising

Based on the discussion made in the previous chapter, the algorithms that were selected as the best, are tested also on the measured submicron CT datasets. This way, the advantages and disadvantages of the algorithms stated for the phantom denoising can be validated or disproved. From the projection domain denoising, the BM3D and BM4D methods are tested. In contrast, the non-local means filter is applied in both the projection and tomogram domains to determine if it can achieve comparable quality to the other advanced methods but with significantly reduced processing time. There is the possibility to use the advanced techniques in both of the domains, but the computational time of processing one measured dataset would be extensive (see section 4.5.1).

Three samples are used for denoising – a toothpick, a polyethylene (PE) rod with carbon fibers, and a mouse embryo. The parameters of the measurement are listed in table 4.4. Each of the samples is different in terms of morphology, contrast, and noise level. The toothpick dataset [83] (see figure 4.12 (a)) has a very characteristic structure consisting of wooden cells. The sample is larger than the detector, so the ROI is the center of the toothpick. The noise in the dataset has a strong pattern probably caused during the reconstruction process by the large amount of cells and sharp transitions. However, the dataset has a very good contrast. The second dataset consists of a polyethylene (PE) rod with carbon fibers with a density of fibers of 15-20%. One slice of the sample is shown in figure 4.12 (b). The white dots are carbon fibers. The measurement was performed using a molybdenum target resulting in higher noise variance. From a subjective evaluation, the dataset is much noisier than the toothpick and the contrast is low. The third sample is the mouse embryo. In the slice in figure 4.12 (c) there are visible fine features and details, that need to be preserved during the processing. A molybdenum target was also used for this measurement.

The assessment is performed using two measures – signal-to-noise ratio and contrast-to-noise ratio, along with subjective evaluation, line-profile comparison, and time consumption.

The denoising approaches were performed on the three samples. The optimal parameters for the methods were found experimentally by subjective evaluation and can be

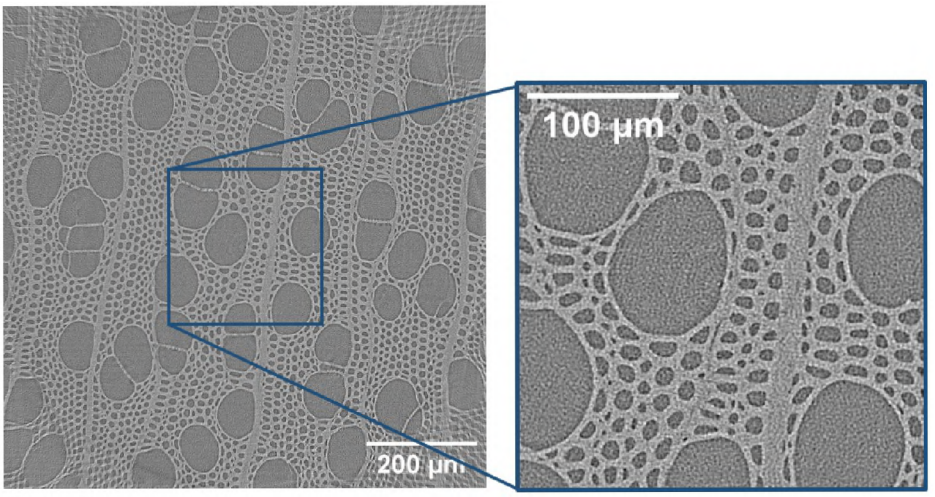

(a)

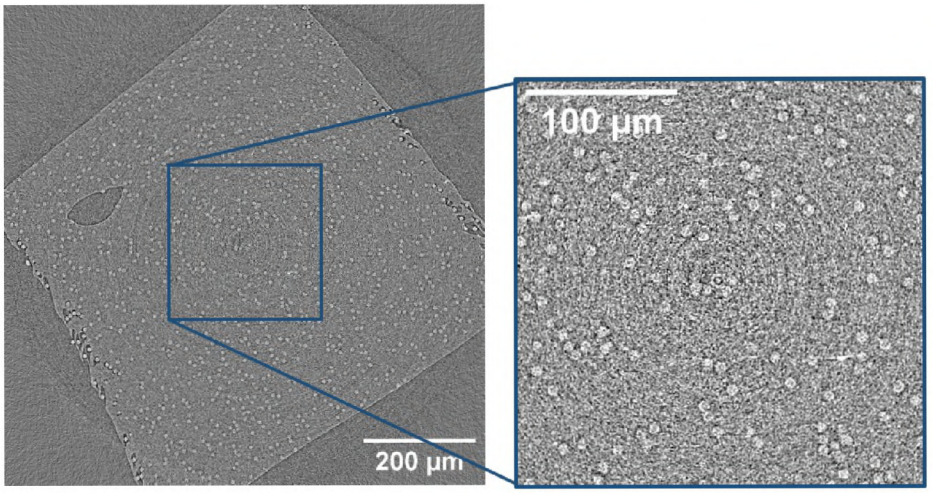

(b)

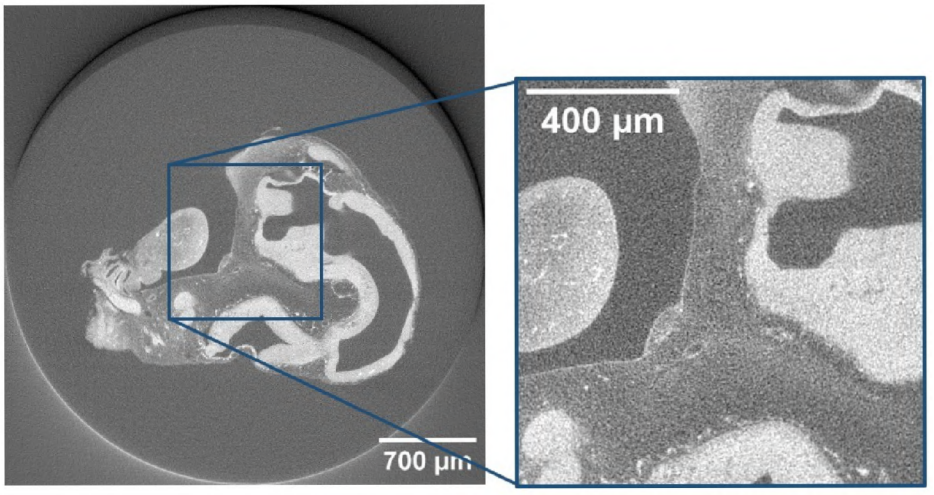

(c)

Figure 4.12: A slice of each sample with zoomed central regions – (a) a slice from the toothpick sample, (b) a slice from the polyethylene sample with carbon fibers, and (c) a slice from the mouse embryo sample.

found in Appendix C. All datasets were reconstructed using CTRec software developed in the CEITEC CTLAB. This software is based on MATLAB implementation of ASTRA Toolbox. The FDK filter was used for the reconstruction with a cosine filter with a cut-off frequency of 0.85, which is taken as an ideal solution for measured samples.

Table 4.4: Parameters for the measurement of analyzed samples.

Sample	Target material	Exposure time	Voltage	Current	Binning	Optics
Toothpick	Cu	23 s	40 kV	30 mA	2	L0270
PE	Mo	5 s	50 kV	24 mA	2	L0270
Mouse embryo	Mo	5 s	50 kV	24 mA	2	L1080

The outcomes are compared using two metrics – signal-to-noise ratio (SNR) and contrast-to-noise ratio (CNR). The formula 1.21 defined earlier was used for computing the SNR. The CNR can be calculated with a formula

$$\mathrm{CNR} = \frac{|\mu_o - \mu_b|}{\sigma_b}, \tag{4.5}$$

where μ_o is the mean signal value in the ROI, μ_b is the mean value, and σ_b is the standard deviation of the signal in the background. The regions used for calculation of the values are illustrated in figure 4.13 – blue regions represent the object, and the green squares illustrate the backgrounds. The regions were selected to be homogeneous. The results of the metrics are listed in table 4.5 with the best outcomes highlighted in bold.

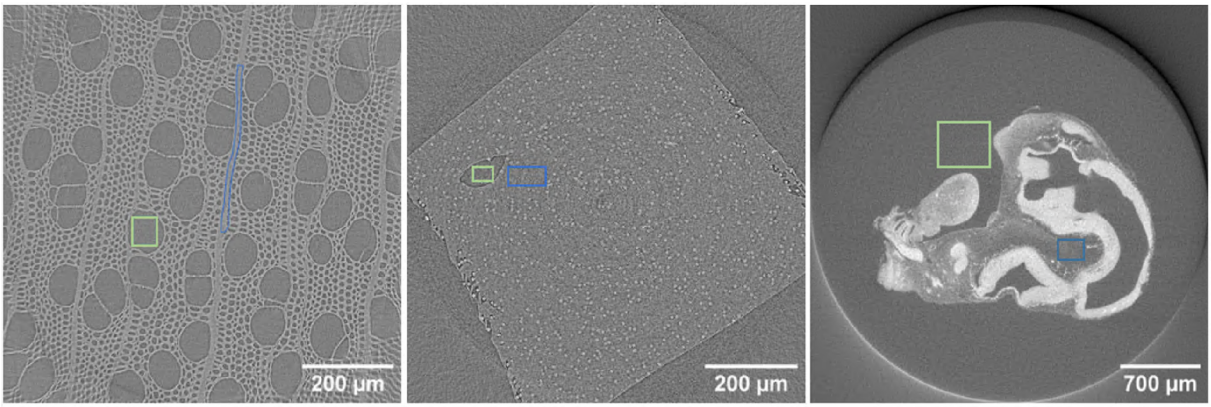

Figure 4.13: Regions used for computing of SNR and CNR. The blue shapes and the green squares illustrate the object region and the background, respectively.

Several observations can be made from the results presented in table 4.5. The important thing is, that all of the approaches improved the SNR and CNR values compared to the unprocessed measurements. In most cases, the BM4D algorithm applied to the tomograms produces the best results. However, the BM4D and BM3D in the projections also notably improved the values, especially for the PE and embryo samples. The double non-local means approach also achieved relatively high values. The most significant improvement in metrics for the double non-local means was observed in the toothpick

Table 4.5: Signal-to-noise ration and contrast-to-noise ratio calculated from one slice for each denoised dataset. Figure 4.13 depicts the regions used in the formulas. The best results are in bold.

	SNR			CNR		
	Toothpick	PE	Embryo	Toothpick	PE	Embryo
measured	7.25	7.29	6.66	1.05	0.24	0.91
BM3D – proj	7.59	17.1	18.8	1.44	0.94	5.52
BM4D – proj	8.65	17.7	**19.8**	2.04	**1.09**	5.62
BM4D – tomo	**14.2**	**22.8**	19.4	**5.74**	0.91	**6.65**
double nlm	13.0	10.1	13.4	5.68	0.82	2.46

sample, while lower values were obtained for the embryo and PE samples, probably due to less effective noise suppression.

Figure 4.14 shows zoomed regions of the denoised slices. All images for each sample are shown in the same intensity range enabling the evaluation of contrast improvement.

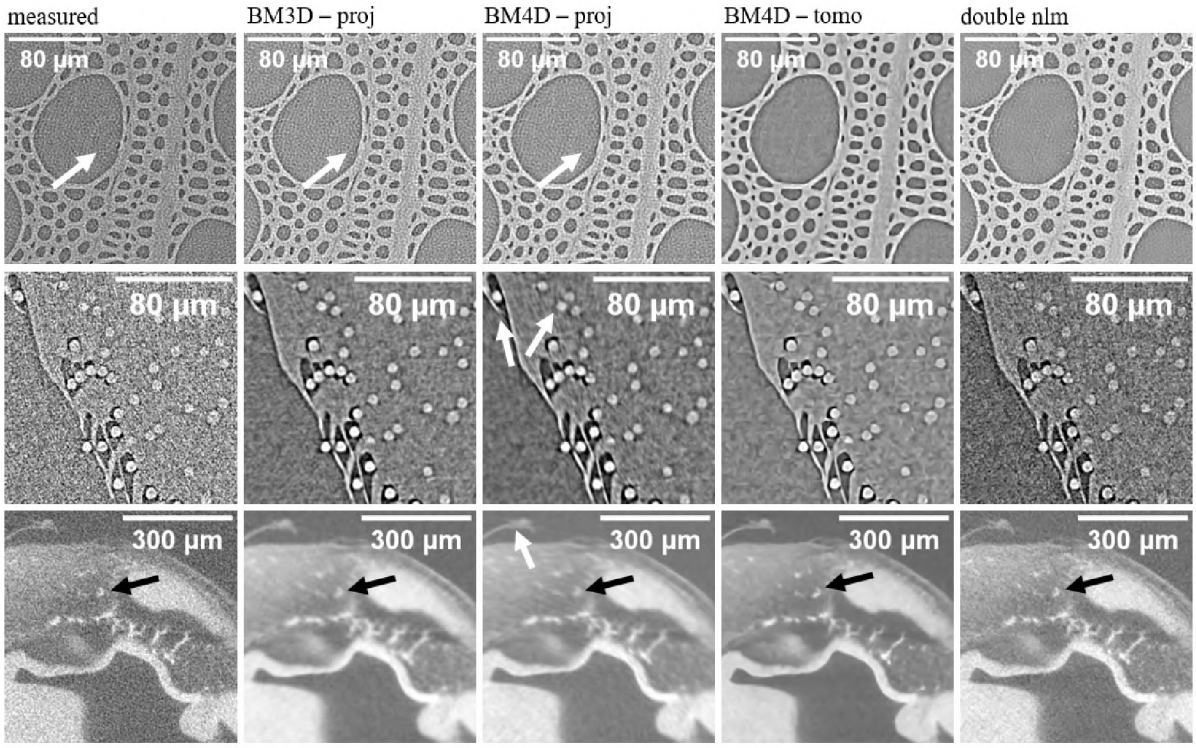

Figure 4.14: Comparison of zoomed regions of one slice after denoising using selected algorithms. Top row: the toothpick sample, middle row: the polyethylene with carbon fibres sample and bottom row: mouse embryo sample. All images for each sample are shown in the same intensity range.

The subjective evaluation is made based on the images in figure 4.14. Overall, there is a noticeable improvement in the quality of all denoised images, but certain observations should be highlighted.

First of all, the structured noise is still visible in the toothpick images after the reduction of noise in the projection domain. This suggests, that this noise truly has its foundations in the reconstruction process and cannot be effectively reduced by denoising in the projection domain. However, the contrast is improved, especially for the BM4D image. Denoising in the projection domain reduces the ring artifacts, which can be observed in the toothpick images indicated by white arrows. On the other hand, the tomogram domain denoising was able to partially suppress the noise pattern while maintaining the features and details. The contrast is also improved, but both the approaches – the BM4D in the tomograms and the double non-local means generated new artifacts. There is visible the effect of blockiness and residuals of the noise pattern.

In the images of the PE sample, the noise is well suppressed even by denoising in the projection domain. The dots and structures are clearer and sharper than in the measured image. The dots and structures appear clearer and sharper compared to the measured image. However, the image resulting from BM4D in the projection domain shows higher blurriness, especially of the features at the edge of the ROI – focus on the features with white arrows. This corresponds to the statements made in the section 4.4.1 for the simulated dataset. The double non-local means filter managed to suppress a certain amount of noise and improve the image quality and definition of the dots, but the noise reduction is not perfect. In the image after BM4D denoising in the tomogram domain, the artifacts and side effects of the noise reduction are noticeable.

For the mouse embryo images, it can be observed that the BM3D method applied to the projections leads to the blurring of features and details. The features are still recognizable, but the sharpness of the shapes is compromised. The same can be stated for the BM4D method in the projection domain but here also the blurriness at the edge of the sample can be noticed – focus on the white arrow at the slice. However, BM4D in the tomogram domain improves the visibility and detectability of features while effectively suppressing the noise. Among all images of this sample, the features and shapes are the clearest. As in the case of other samples, the double non-local means method leads to some noise suppression, but the slice still appears noisy. Nevertheless, the details are more clearly detectable compared to the measured image. The black arrows in the images highlight a detail where the differences between the approaches can be observed.

Now, the line-profile plots are visualized for comparison of edge enhancement and sharpness.

The comparison of the edges of the toothpick slice is shown in figure 4.15. The profiles are drawn along the white line illustrated in the slice. The profile plots are a result of averaging 5 lines. It is evident that all denoising approaches enhance the edges. In this comparison, the BM3D in the projections seems to be affected by the noise the most. The BM4D method in the projections results in smaller peaks in the line-profile plot suggesting better noise suppression. The BM4D in the tomograms smooths the edges of the boundaries, but the differences between the highest and lowest points are still high. The double non-local means filter (NLM in the legend) offers a compromise between denoising in the tomogram and projection domains. It is not as smooth as the BM4D in the tomograms, but it preserves better edge sharpness.

Figure 4.16 illustrates the edge enhancement of the polyethylene and air pore borderline. The focus of this comparison is on the two peaks of the edge, which can be easily observed in the plot. The BM4D method in the tomograms is effective in suppressing the noise, but it also smooths the edge, resulting in a lesser difference between the highest

and lowest points of the line. The double non-local means (NLM) line shows many secondary peaks suggesting a noisy appearance. The best in this comparison is the BM3D and BM4D projection domain outcomes. The results are independent of the noisy profile, making the edge enhancement more apparent. Both BM3D and BM4D in the projection domain successfully suppress the noise and smooth the line outside the edge.

For the line-profile comparison for the mouse embryo sample (see fig. 4.17), the region, where there are quick changes in the grey value is selected. Ideally, the methods should preserve sharp transitions and maintain the differences between the grey values. The highest peak in the brightest region is observed in the BM4D method in the projection domain. However, the transition between the region and the background appears less sharp, suggesting possible blurring. The BM3D method in the projections and the BM4D in the tomograms on the other hand have very sharp transitions – the decrease of grey values at the edge of the region is apparent. The double non-local means profile plot is noticeably affected by noise.

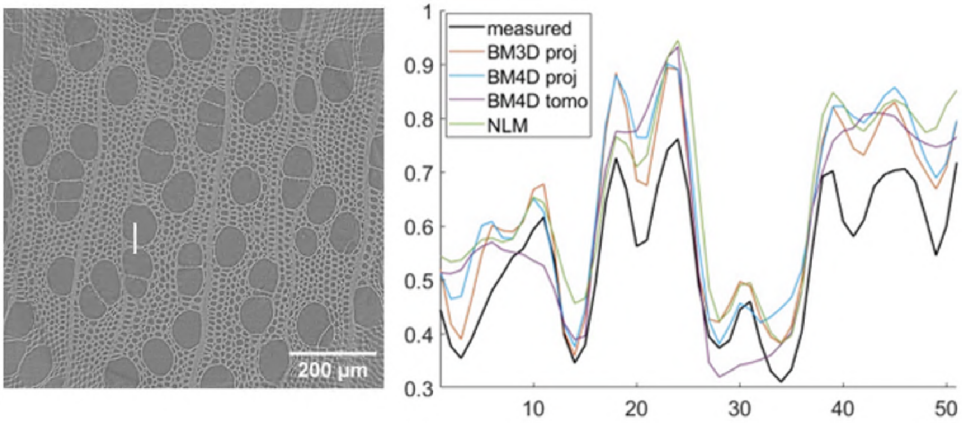

Figure 4.15: Line-profile plots comparing the edge enhancement in the reconstructed slices after denoising with selected approaches. The plots are drawn along the white line in the slice of the toothpick sample on the left.

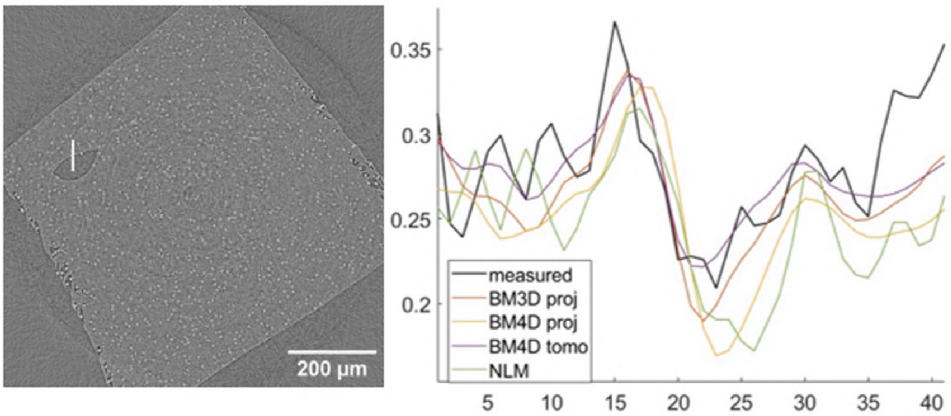

Figure 4.16: Line-profile plots comparing the edge enhancement in the reconstructed slices after denoising with selected approaches. The plots are drawn along the white line in the slice of the PE sample on the left.

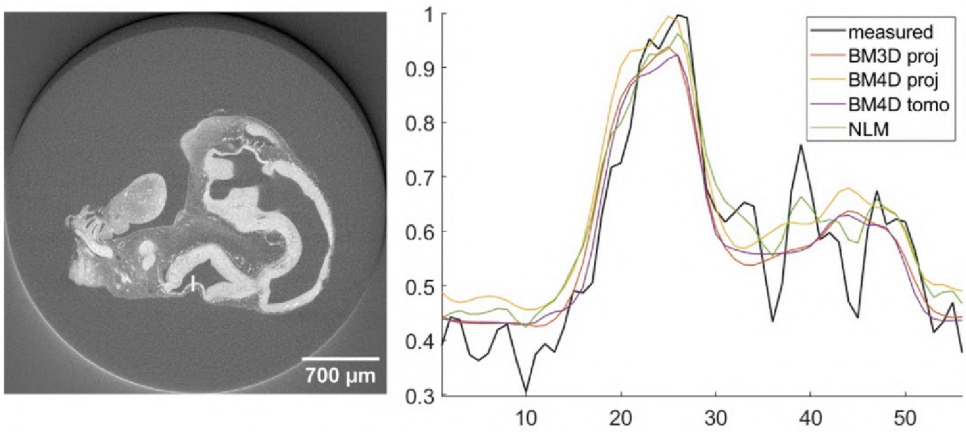

Figure 4.17: Line-profile plots comparing the edge enhancement in the reconstructed slices after denoising with selected approaches. The plots are drawn along the white line in the slice of the mouse embryo sample on the left.

Another thing to consider is the possibility and quality of automatic segmentation of the measured and denoised datasets. For this discussion, only the toothpick sample will be analyzed, as it is well-suited for automatic segmentation. The segmentation is performed using the Otsu method.

Figure 4.18 shows the central regions of the segmented slices for each method. There are also shown histograms of the denoised slices used for the segmentation.

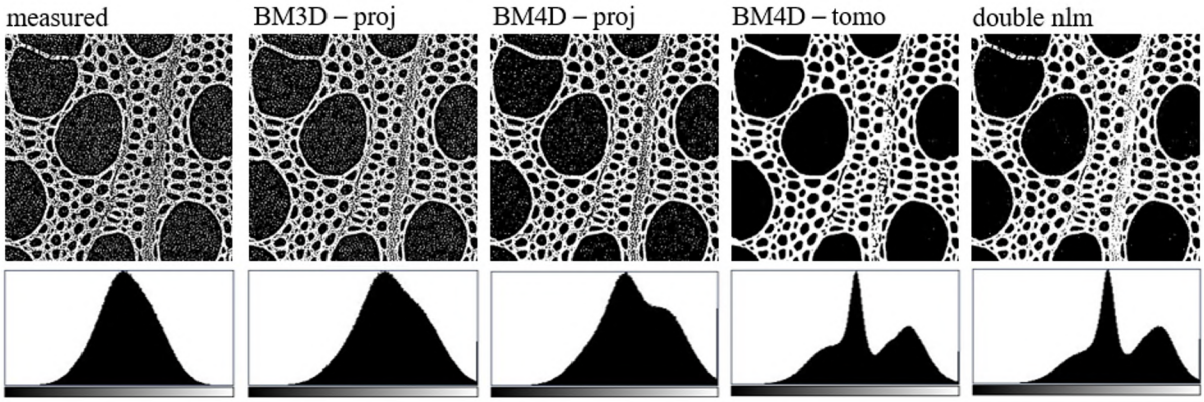

Figure 4.18: Automatic segmentation using the Otsu method of one slice from each dataset of the toothpick sample. The zoomed central region of each segmented slice and histograms of denoised slices before segmentation are shown.

The histograms in the bottom row of figure 4.18 provide insights into the segmentation outcomes. In the histogram for the BM3D method in the projection domain, there is not much difference from the histogram of the measured slice. The distribution of grey values appears uniform, indicating a connection between the signal and the noise. This can be seen in the segmented image – the noise cannot be effectively separated without the loss of some information. In the histogram for the BM4D method in the projections, almost two peaks are visible. This suggests that the noise separation is more effective than the BM3D method in the projections, although some residual noise still affects the segmentation. The last two histograms correspond to the BM4D method in the tomogram domain and the double non-local means filter. In both cases, the peaks of the grey values are separated, indicating successful separation of the noise and the signal. The segmented slice after

BM4D denoising in the tomogram domain has smoother regions with fewer voids than the non-local means, but in this case, it is up to the user to decide, what outcome is closer to the reality.

4.5.1. Time duration

For real datasets, the time duration is even more important. The images for processing are larger in size (1648 px × 1250 px × 800 projections and 1648 px × 1648 px × 1250 tomograms) so the time needed for reduction of noise is a major contributor to the whole processing time.

Table 4.6: Time consumption of tested approaches for processing of one image from the real dataset.

algorithm	time per image [s]	time per dataset [h]
BM3D – projections	65	14.4
BM4D – projections	61	13.6
BM4D – tomograms	77	26.7
double non-local means	3.6 + 1.5	1.32

The number of seconds needed for processing one image and the time for processing the whole dataset in hours is listed in table 4.6. It is important to note that these times are approximate and can vary depending on the dataset, but for simplicity, an average value is provided. The double non-local means filter shows the largest variation in the processing time of the datasets, as the parameter can affect the duration. However, for all three datasets, the processing time for one projection and one tomogram was in the range of 4-6 seconds. The time consumption of the whole dataset was computed by multiplying the time per image by the corresponding number of images – 800 for projections, and 1250 for tomograms.

The table clearly shows that the processing times of both the algorithms BM3D and BM4D are very long. Specifically, the BM4D method in the tomogram domain takes almost twice as long as the methods in the projections due to the bigger sizes of the images and the fact, that over 400 images more need to be processed. The fastest in this comparison is the non-local means filter, even though the processing is in both of the domains.

4.5.2. Discussion of the results of measured datasets denoising

It is obvious that all of the proposed approaches have significantly improved the quality of the three datasets. This improvement is supported by the calculated metrics such as SNR and CNR, as well as the line-profile plots. However, there are notable differences among the outcomes of the different methods.

When it comes to determining the optimal parameters for the methods, the BM3D method offers a significant advantage over the BM4D approaches for 3D data. This is because the parameters can be tested on a sub-region of the 2D image, making the process much faster compared to the 3D methods that require processing a batch of images.

The BM3D method in the projection domain has greatly enhanced contrast, edges, detectability, and differentiation of details. It can be used for every sample, since it improved the quality significantly without generating new artifacts. However, in the case of low-attenuation samples, such as the mouse embryo sample, finer details appear blurred. Similar outcomes can be observed for the BM4D method in the projection domain. In the reconstructed slices of the PE sample and the mouse embryo, the blurring effect on features located farther away from the center is noticeable. This suggests that the BM4D method in the projection domain is not well-suited for denoising samples that are fully within the field of view. This behaviour can be also partially caused by the higher amount of noise in the molybdenum measurements.

In summary, the projection domain approaches are not very optimal for denoising of low-attenuation biological samples. Soft tissues in these samples are typically not very contrasting (see figure 4.1), and the differences in attenuation coefficients are not very high, leading to blurred edges and fine details. On the other hand, the BM4D method in the tomogram domain improved the clarity of the fine details in the biological sample significantly. In the other two samples, the results are also satisfactory, but the method can lead to slight smoothing of the edges. The noise is effectively suppressed, although some blockiness from the algorithm itself may be observed. The double non-local means filtering managed to improve the quality notably, but the noise suppression is only mediocre. However, the performance is optimal for the computational time needed for the processing. The comparison of automatic segmentation for the toothpick sample suggests, that the tomogram domain denoising is more suitable for this task delivering better results.

4.6. Proposed denoising strategies

Based on the discussion and testing of the selected approaches, certain rules and limitations have been identified. This section will provide a quick summary of the advantages and disadvantages and guidelines for better understanding the capabilities, constraints, and possible usage of the denoising methods. Multiple criteria will be considered, mainly regarding the user's expectations and the sample for processing.

General advantages and characteristics observed from the testing are summarized in the table 4.7.

For **segmentation**, either automatic or manual, the tomogram domain denoising with BM4D is the optimal approach. Manual segmentation is relevant mostly for biological samples, and there the definition and clarity of the fine details and features are the best. For the segmentation, the possible artifacts from the reconstruction are not relevant.

When the user wants to improve the quality, but has **limited time for processing**, the double non-local means filter can be used. Some residual noise can be left in the reconstructed slices, but the contrast and the clarity of the fine details improve.

For a generation of **state-of-the art images**, the selection of appropriate denoising is dependent on the sample. For **low-attenuation samples**, the denoising in the projection domain can lead to the blurring of fine details, so the tomogram domain approach – BM4D should be used. For **high-attenuation samples**, the projection domain denoising is a safer option. It cannot affect the slices as much as the tomogram domain denoising. Mostly, the BM3D in the projections is the better and more universal approach. This

approach can be used for both copper target and molybdenum target measurements. The BM4D method can be used only with samples, that are larger than the field of view and only for Cu target. In the tomogram domain, the user needs to be aware of the artifacts that the denoising can bring. But with the right parameters, it can be minimized.

In conclusion, the choice between denoising in the projection domain and tomogram domain depends on the specific requirements of the dataset and the expectations of the user. Understanding the advantages and disadvantages described in this section can help determine the most suitable approach for denoising different types of samples.

Table 4.7: Summary of the denoising approaches in the projection and tomogram domain.

Projection domain denoising	Tomogram domain denoising
• subtle denoising • ring artifacts suppression • contrast enhancement • no artifacts from the denoising • not suitable for low-attenuation samples • residual noise present	• better definition of fine details and features • better noise suppression • contrast enhancement • slight smoothing of the edges • generation of new artifacts from the denoising • better suitable for segmentation

Conclusion

The X-ray computed tomography (CT) is a very powerful non-destructive diagnostic technique. It is used in a wide range of applications, including medical diagnosis, industrial inspection, materials analysis, and archaeological research. However, during each measurement and reconstruction process, noise is generated in the images. Images with high levels of noise can be difficult to interpret, as the noise can obscure important details and structures. Therefore, the amount of noise should be minimized in CT images to improve their accuracy.

Since the captured noise in the projection images is a mixture of many influences, its distribution is unknown. Therefore, the statistical analysis of the noise in bright field images captured using the high-resolution CT system Rigaku nano3DX was performed. The noise can be described with *mixed Gaussian-Poisson distribution*. For practical purposes, the Poisson part of the noise was approximated by Gaussian distribution. Therefore, the noise can be modeled with Gaussian distribution with zero mean and signal-dependent variance. The exact model of the noise variance was determined and validated by comparison to the actual noise present in the bright field images.

Based on the estimated noise variance model, the artificial noise could be generated in the projection images of a simulated phantom. Seven methods for noise reduction for 2D images and four denoising methods for volumetric datasets were tested on the projections. The evaluation was made on the reconstructed slices both objectively and subjectively. The same methods were tested in the tomogram domain and the evaluation process was repeated. The results from both domains were discussed and promising approaches were selected for testing on real datasets. The selected approaches were the BM3D and BM4D methods in the projections and the BM4D method in the tomogram domain. In the tomogram domain, this 3D method has superior performance over the 2D methods. Additionally, the non-local means filter in both the projection domain and the tomogram domain was chosen as a fast alternative for noise reduction.

All of the proposed strategies were able to improve the quality of the measured submicron CT datasets. The outcomes were compared objectively by image quality metrics and subjectively by visual inspection. The possibility of automatic segmentation was also discussed. Based on this comparison, the optimal usage of each denoising strategy was proposed considering multiple criteria, and the advantages and disadvantages of both denoising in the projection and tomogram domain were summarized. The BM3D in the projection domain was selected to be the safest and the most universal strategy. It can be used for both molybdenum and copper measurements. However, the possible blur with low-attenuation slices should be taken into consideration. The time consumption is high, but the quality of the reconstructed slices is significantly improved without creating artifacts from the denoising. For the task of segmentation, the BM4D method in the tomogram domain is the best option independent of the target material. When fast denoising is required, the non-local means filtering both in the projection domain and the tomogram domain can be performed. Some residual noise will be left in the reconstructed slices, but the contrast and the clarity of details and features will improve. However, the user needs to be aware, that by denoising in the tomogram domain, the artifacts from the algorithms could be generated.

This thesis gave a comprehensive comparison of the advantages and disadvantages of denoising in the projection and tomogram domain and can lead to a better understanding

and awareness of the usage and limitations of the approaches. However, the search for new, better, and faster noise reduction strategies should continue.

Bibliography

[1] HESSENBRUCH, A.: A brief history of x-rays. *Endeavour*. 2002, vol. 26, no. 4, pp. 137–141. ISSN 0160-9327. Available from DOI: https://doi.org/10.1016/S0160-9327(02)01465-5.

[2] HSIEH, J.: *Computed Tomography: Principles, Design, Artifacts, and Recent Advances, Second Edition*. WA: SPIE, 2009.

[3] TESAŘOVÁ, M.: *Quantitative 3D characterization of biological structures by X-ray computed microtomography*. 2022. PhD thesis. Vysoké učení technické v Brně, Středoevropský technologický institut VUT.

[4] KRUTH, J. et al.: Computed tomography for dimensional metrology. *CIRP Annals*. 2011, vol. 60, no. 2, pp. 821–842. ISSN 0007-8506. Available from DOI: https://doi.org/10.1016/j.cirp.2011.05.006.

[5] KHARFI, F.: Mathematics and Physics of Computed Tomography (CT): Demonstrations and Practical Examples. In: *Imaging and Radioanalytical Techniques in Interdisciplinary Research*. Rijeka: IntechOpen, 2013, chap. 4. Available from DOI: 10.5772/52351.

[6] LENG, S. et al.: Photon-counting Detector CT: System Design and Clinical Applications of an Emerging Technology. *RadioGraphics*. 2019, vol. 39, no. 3, pp. 729–743. Available from DOI: 10.1148/rg.2019180115. PMID: 31059394.

[7] AZZARI, L.; BORGES, L., and FOI, A.: Modeling and Estimation of Signal-Dependent and Correlated Noise. In: *Denoising of Photographic Images and Video*. 2018, pp. 1–36. ISBN 978-3-319-96028-9. Available from DOI: 10.1007/978-3-319-96029-6_1.

[8] ŠALPLACHTA, J. et al.: CCD and scientific-CMOS detectors for submicron laboratory based X-ray Computed Tomography. *e-Journal of Nondestructive Testing*. 2019, pp. 1–8.

[9] CUNNINGHAM, I. and JUDY, P.: Computed Tomography. 2012. ISBN 978-1-4398-7102-7. Available from DOI: 10.1201/b12939-3.

[10] BERGMANN, R.; BESSLER, F., and BAUER, W.: Non-Destructive Testing in the Automotive Supply Industry - Requirements, Trends and Examples Using X-ray CT. 2006.

[11] GRIGORYAN, A.: Solution of the Problem on Image Reconstruction in Computed Tomography. *Journal of Mathematical Imaging and Vision*. 2015, vol. 54. Available from DOI: 10.1007/s10851-015-0588-6.

[12] KAK, A. C.; SLANEY, M., and WANG, G.: Principles of Computerized Tomographic Imaging. *Medical Physics*. 2002, vol. 29, no. 1, pp. 107–107. Available from DOI: https://doi.org/10.1118/1.1455742.

[13] SEUNG-WAN, L. et al.: Effects of Reconstruction Parameters on Image Noise and Spatial Resolution in Cone-beam Computed Tomography. *Journal of the Korean Physical Society*. 2011, vol. 59, p. 2825. Available from DOI: 10.3938/jkps.59.2825.

[14] RODET, T.; NOO, F., and DEFRISE, M.: The cone-beam algorithm of Feldkamp, Davis, and Kress preserves oblique line integrals. *Medical physics*. 2004, vol. 31, pp. 1972–5. Available from DOI: 10.1118/1.1759828.

[15] STILLER, W.: Basics of Iterative Reconstruction Methods in Computed Tomography: A Vendor-independent Overview. *European Journal of Radiology*. 2018, vol. 109. Available from DOI: 10.1016/j.ejrad.2018.10.025.

[16] BEISTER, M.; KOLDITZ, D., and KALENDER, W. A.: Iterative reconstruction methods in X-ray CT. *Physica Medica*. 2012, vol. 28, no. 2, pp. 94–108. ISSN 1120-1797. Available from DOI: https://doi.org/10.1016/j.ejmp.2012.01.003.

[17] KRÄMER, A.; KOVACHEVA, E., and LANZA, G.: Projection based evaluation of CT image quality in dimensional metrology. *e-Journal of Nondestructive Testing*. 2015, vol. 20.

[18] HSIEH, S. et al.: A minimum SNR criterion for computed tomography object detection in the projection domain. *Medical Physics*. 2022, vol. 49, no. 8, pp. 4988–4998. ISSN 0094-2405. Available from DOI: 10.1002/mp.15832.

[19] RODRÍGUEZ SÁNCHEZ, A. et al.: Review of the influence of noise in X-ray computed tomography measurement uncertainty. *Precision Engineering*. 2020, vol. 66. Available from DOI: 10.1016/j.precisioneng.2020.08.004.

[20] VILLARRAGA-GÓMEZ, H. and SMITH, S. T.: Effect of the number of projections on dimensional measurements with X-ray computed tomography. *Precision Engineering*. 2020, vol. 66, pp. 445–456. ISSN 0141-6359. Available from DOI: https://doi.org/10.1016/j.precisioneng.2020.08.006.

[21] LI, X. and LUO, S.: A compressed sensing-based iterative algorithm for CT reconstruction and its possible application to phase contrast imaging. *Biomedical engineering online*. 2011, vol. 10, p. 73. Available from DOI: 10.1186/1475-925X-10-73.

[22] ZHANG, Z. et al.: A Sparse-View CT Reconstruction Method Based on Combination of DenseNet and Deconvolution. *IEEE Transactions on Medical Imaging*. 2018, vol. 37, no. 6, pp. 1407–1417. Available from DOI: 10.1109/TMI.2018.2823338.

[23] DIWAKAR, M. and KUMAR, M.: A review on CT image noise and its denoising. *Biomedical Signal Processing and Control*. 2018, vol. 42, pp. 73–88. Available from DOI: 10.1016/j.bspc.2018.01.010.

[24] FELLERS, T. J.; VOGT, K. M., and DAVIDSON, M. W.: *CCD signal-to-noise ratio*. 2023. Available also from: https://www.microscopyu.com/tutorials/ccd-signal-to-noise-ratio.

[25] GREFFIER, J. et al.: Image quality and dose reduction opportunity of deep learning image reconstruction algorithm for CT: a phantom study. *European Radiology*. 2020, vol. 30. Available from DOI: 10.1007/s00330-020-06724-w.

[26] SZCZYKUTOWICZ, T. et al.: A Review of Deep Learning CT Reconstruction: Concepts, Limitations, and Promise in Clinical Practice. *Current Radiology Reports*. 2022, vol. 10. Available from DOI: 10.1007/s40134-022-00399-5.

[27] DANNHOFEROVÁ, J.: *Velká kniha barev: Kompletní průvodce pro grafiky, fotografy a designéry*. Praha: Computer Press, 2012. ISBN 978-80-251-3785-7.

[28] SOLOMON, C. and BRECKON, T.: *Fundamentals of Digital Image Processing: A Practical Approach with Examples in Matlab*. 1st. Wiley Publishing, 2011. ISBN 0470844736.

[29] FORBES, C. et al.: *Statistical distributions, Fourth Edition*. John Wiley & Sons, Inc., Hoboken, New Jersey., 2011. ISBN 978-0-470-39063-4.

[30] BOYAT, A. K. and JOSHI, B. K.: A Review Paper: Noise Models in Digital Image Processing. 2015. Available from DOI: 10.48550/ARXIV.1505.03489.

[31] LONGNECKER, M. and LYMAN, R.: *An Introduction to Statistical Methods and Data Analysis, Seventh Edition*. Cengage Learning, 2001. ISBN 978-1305269477.

[32] BENESTY, J.; CHEN, J., and HUANG, Y.: Study of the widely linear Wiener filter for noise reduction. *Proceedings of the IEEE International Conference on Acoustics, Speech, and Signal Processing, ICASSP*. 2010, pp. 205–208. Available from DOI: 10.1109/ICASSP.2010.5496033.

[33] TOMASI, C. and MANDUCHI, R.: Bilateral filtering for gray and color images. In: *Sixth International Conference on Computer Vision*. 1998, pp. 839–846. Available from DOI: 10.1109/ICCV.1998.710815.

[34] COLL, B. and MOREL, J.-M.: A non-local algorithm for image denoising. In: 2005, vol. 2, 60–65 vol. 2. ISBN 0-7695-2372-2. Available from DOI: 10.1109/CVPR.2005.38.

[35] ZHANG, B. and ALLEBACH, J. P.: Adaptive Bilateral Filter for Sharpness Enhancement and Noise Removal. *IEEE Transactions on Image Processing*. 2008, vol. 17, no. 5, pp. 664–678. Available from DOI: 10.1109/TIP.2008.919949.

[36] FROSIO, I. and KAUTZ, J.: Statistical Nearest Neighbors for Image Denoising. *IEEE Transactions on Image Processing*. 2018, vol. 28, pp. 1–1. Available from DOI: 10.1109/TIP.2018.2869685.

[37] WU, Y. et al.: Probabilistic Non-Local Means. *IEEE Signal Processing Letters*. 2013, vol. 20. Available from DOI: 10.1109/LSP.2013.2263135.

[38] COUPÉ, P. et al.: An Optimized Blockwise Nonlocal Means Denoising Filter for 3-D Magnetic Resonance Images. *IEEE Transactions on Medical Imaging*. 2008, vol. 27. Available from DOI: 10.1109/TMI.2007.906087.

[39] COUPÉ, P. et al.: A CANDLE for a deeper in vivo insight. *IMedical image analysis*. 2012, pp. 849–864. Available from DOI: 10.1016/j.media.2012.01.002.

[40] PERONA, P. and MALIK, J.: Scale-space and edge detection using anisotropic diffusion. *IEEE Transactions on Pattern Analysis and Machine Intelligence*. 1990, vol. 12, no. 7, pp. 629–639. Available from DOI: 10.1109/34.56205.

[41] RUHELA, R.; BHUPENDRA, G., and LAMBA, S.: An efficient anisotropic diffusion model for image denoising with edge preservation. *Computers & Mathematics with Applications*. 2021, vol. 93, pp. 106–119. Available from DOI: 10.1016/j.camwa.2021.03.029.

[42] GETREUER, P.: Rudin-Osher-Fatemi Total Variation Denoising using Split Bregman. *Image Processing On Line*. 2012, vol. 2, pp. 74–95. Available from DOI: 10.5201/ipol.2012.g-tvd.

[43] LANDI, G. and PICCOLOMINI, E.: An efficient method for nonnegatively constrained Total Variation-based denoising of medical images corrupted by Poisson noise. *Computerized medical imaging and graphics : the official journal of the Computerized Medical Imaging Society*. 2011, vol. 36, pp. 38–46. Available from DOI: 10.1016/j.compmedimag.2011.07.002.

[44] SUN, C. et al.: Exponential total variation model for noise removal, its numerical algorithms and applications. *AEU - International Journal of Electronics and Communications*. 2015, vol. 69. Available from DOI: 10.1016/j.aeue.2014.12.006.

[45] AL-AMEEN, Z. and SULONG, G.: Attenuating Noise from Computed Tomography Medical Images using a Coefficients-Driven Total Variation Denoising Algorithm. *International Journal of Imaging Systems and Technology*. 2014, vol. 24. Available from DOI: 10.1002/ima.22112.

[46] BLU, T. and LUISIER, F.: The SURE-LET approach to image denoising. *IEEE transactions on image processing : a publication of the IEEE Signal Processing Society*. 2007, vol. 16, pp. 2778–86. Available from DOI: 10.1109/TIP.2007.906002.

[47] FOI, A.: *Pointwise shape-adaptive DCT image filtering and signal-dependent noise estimation*. 2007. ISBN 978-952-15-1922-2. PhD thesis. Tampere University of Technology.

[48] DABOV, K. et al.: Image Denoising by Sparse 3-D Transform-Domain Collaborative Filtering. *IEEE transactions on image processing : a publication of the IEEE Signal Processing Society*. 2007, vol. 16, pp. 2080–95. Available from DOI: 10.1109/TIP.2007.901238.

[49] CHEN, Q. and WU, D.: Wu, D.: Image Denoising By Bounded Block Matching and 3d Filtering. Signal Processing 90, 2778-2783. *Signal Processing*. 2010, vol. 90, pp. 2778–2783. Available from DOI: 10.1016/j.sigpro.2010.03.016.

[50] DABOV, K. et al.: BM3D Image Denoising With Shape-Adaptive Principal Component Analysis. *Proc. Workshop on Signal Processing with Adaptive Sparse Structured Representations (SPARS'09)*. 2009.

[51] BASHAR, F. and EL-SAKKA, M.: BM3D Image Denoising using Learning-based Adaptive Hard Thresholding. *International Conference on Computer Vision Theory and Applications*. 2016, pp. 204–214. Available from DOI: 10.5220/0005787202040214.

[52] MAGGIONI, M. et al.: A Nonlocal Transform-Domain Filter for Volumetric Data Denoising and Reconstruction. *IEEE transactions on image processing : a publication of the IEEE Signal Processing Society*. 2012, vol. 22. Available from DOI: 10.1109/TIP.2012.2210725.

[53] CHIANG, Y.-W. and SULLIVAN, B.: Multi-frame image restoration using a neural network. *Proceedings of the 32nd Midwest Symposium on Circuits and Systems*, 1989, 744–747 vol.2. Available from DOI: 10.1109/MWSCAS.1989.101962.

[54] JAIN, V. and SEUNG, H.: Natural Image Denoising with Convolutional Networks. *Advances in Neural Information Processing Systems 21 - Proceedings of the 2008 Conference*. 2008, pp. 769–776.

[55] ZHANG, K. et al.: Beyond a Gaussian Denoiser: Residual Learning of Deep CNN for Image Denoising. *IEEE Transactions on Image Processing*. 2017, vol. 26, no. 7, pp. 3142–3155. Available from DOI: 10.1109/tip.2017.2662206.

[56] WANG, W.: An improved denoising model for convolutional neural network. *Journal of Physics: Conference Series*. 2021, vol. 1982, no. 1, p. 012169. Available from DOI: 10.1088/1742-6596/1982/1/012169.

[57] CRUZ, C. et al.: Nonlocality-Reinforced Convolutional Neural Networks for Image Denoising. *IEEE Signal Processing Letters*. 2018, vol. PP. Available from DOI: 10.1109/LSP.2018.2850222.

[58] ZHANG, K.; ZUO, W., and ZHANG, L.: FFDNet: Toward a Fast and Flexible Solution for CNN-Based Image Denoising. *IEEE Transactions on Image Processing*. 2018, vol. 27, no. 9, pp. 4608–4622. Available from DOI: 10.1109/tip.2018.2839891.

[59] GUO, S. et al.: Toward Convolutional Blind Denoising of Real Photographs. In: 2019, pp. 1712–1722. Available from DOI: 10.1109/CVPR.2019.00181.

[60] LEHTINEN, J. et al.: *Noise2Noise: Learning Image Restoration without Clean Data*. arXiv, 2018. Available from DOI: 10.48550/ARXIV.1803.04189.

[61] KRULL, A.; BUCHHOLZ, T.-O., and JUG, F.: *Noise2Void - Learning Denoising from Single Noisy Images*. arXiv, 2018. Available from DOI: 10.48550/ARXIV.1811.10980.

[62] TAKEDA, Y. and HAMADA, K.: A primer on the use of the nano3DX high-resolution X-ray microscope. *Rigaku journal*. **31**(1),2015.

[63] *The MathWorks Inc.,MATLAB version: 9.13.0 (R2022b)*. Natick, Massachusetts, United States: The MathWorks Inc., 2022. Available also from: https://www.mathworks.com.

[64] FOI, A. et al.: Practical Poissonian-Gaussian Noise Modeling and Fitting for Single-Image Raw-Data. *IEEE Transactions on Image Processing*. 2008, vol. 17, no. 10, pp. 1737–1754. Available from DOI: 10.1109/TIP.2008.2001399.

[65] LI, J. et al.: Parameter Estimation of Poisson–Gaussian Signal-Dependent Noise from Single Image of CMOS/CCD Image Sensor Using Local Binary Cyclic Jumping. *Sensors*. 2021, vol. 21, p. 8330. Available from DOI: 10.3390/s21248330.

[66] KUMAR, M. and DIWAKAR, M.: CT image denoising using locally adaptive shrinkage rule in tetrolet domain. *Journal of King Saud University - Computer and Information Sciences*. 2018, vol. 30, no. 1, pp. 41–50. ISSN 1319-1578. Available from DOI: https://doi.org/10.1016/j.jksuci.2016.03.003.

[67] WANG, J. et al.: Domain-adaptive denoising network for low-dose CT via noise estimation and transfer learning. *Medical Physics*. 2023, vol. 50, no. 1, pp. 74–88. Available from DOI: https://doi.org/10.1002/mp.15952.

[68] GOLDSTEIN, T.: *Split Bregman* [https://www.cs.umd.edu/~tomg/projects/split_bregman/]. 2014.

[69] FOI, A. and DABOV, K.: *Pointwise Shape-Adaptive DCT Demobox* [http://www.cs.tut.fi/~foi/SA-DCT]. 2016.

[70] MÄKINEN, Y.; AZZARI, L., and FOI, A.: *Image and video denoising by sparse 3D transform-domain collaborative filtering* [https://webpages.tuni.fi/foi/GCF-BM3D/]. 2020.

[71] WANG, Y. and LI, T.: Application of Wavelet and Wiener Filtering Algorithm in Image De-Noising. *OALib*. 2016, vol. 03, pp. 1–7. Available from DOI: 10.4236/oalib.1102319.

[72] ZANCHETTIN, C. and LUDERMIR, T.: Wavelet filter for noise reduction and signal compression in an artificial nose. *Applied Soft Computing*. 2007, vol. 7, no. 1, pp. 246–256. ISSN 1568-4946. Available from DOI: https://doi.org/10.1016/j.asoc.2005.06.004.

[73] AARLE, W. et al.: The ASTRA Toolbox: A platform for advanced algorithm development in electron tomography. *Ultramicroscopy*. 2015, vol. 157. Available from DOI: 10.1016/j.ultramic.2015.05.002.

[74] AARLE, W. et al.: Fast and flexible X-ray tomography using the ASTRA toolbox. *Optics Express*. 2016, vol. 24, pp. 25129–25147. Available from DOI: 10.1364/OE.24.025129.

[75] PELT, D. et al.: Integration of TomoPy and the ASTRA toolbox for advanced processing and reconstruction of tomographic synchrotron data. *Journal of Synchrotron Radiation*. 2016, vol. 23, pp. 842–849. Available from DOI: 10.1107/S1600577516005658.

[76] MOHAMMADI, P.; EBRAHIMI-MOGHADAM, A., and SHIRANI, S.: Subjective and Objective Quality Assessment of Image: A Survey. *Majlesi Journal of Electrical Engineering*. 2014, vol. 9.

[77] SARA, U.; AKTER, M., and UDDIN, M.: Image Quality Assessment through FSIM, SSIM, MSE and PSNR—A Comparative Study. *Journal of Computer and Communications*. 2019, vol. 07, pp. 8–18. Available from DOI: 10.4236/jcc.2019.73002.

[78] PEDERSEN, M. and HARDEBERG, J.: Full-Reference Image Quality Metrics: Classification and Evaluation. *Foundations and Trends® in Computer Graphics and Vision*. 2012, vol. 7, pp. 1–80. Available from DOI: 10.1561/0600000037.

[79] ZOU, K. et al.: Statistical Validation of Image Segmentation Quality Based on a Spatial Overlap Index. *Academic radiology*. 2004, vol. 11, pp. 178–89. Available from DOI: 10.1016/S1076-6332(03)00671-8.

[80] PELT, D. M.; HENDRIKSEN, A. A., and BATENBURG, K. J.: Foam-like phantoms for comparing tomography algorithms. *Journal of Synchrotron Radiation*. 2022, vol. 29, no. 1, pp. 254–265. Available from DOI: 10.1107/S1600577521011322.

[81] BORSDORF, A. et al.: Analytic noise propagation for anisotropic denoising of CT images. In: *2008 IEEE Nuclear Science Symposium Conference Record*. 2008, pp. 5335–5338. Available from DOI: 10.1109/NSSMIC.2008.4774438.

[82] IMMERKÆR, J.: Fast Noise Variance Estimation. *Computer Vision and Image Understanding*. 1996, vol. 64, no. 2, pp. 300–302. ISSN 1077-3142. Available from DOI: https://doi.org/10.1006/cviu.1996.0060.

[83] ŠALPLACHTA, J. et al.: *Toothpick CT scan*. 2022. Available from DOI: https://doi.org/10.48700/datst.sn1dn-tmm57.

List of abbreviations and symbols

1D	one-dimensional
2D	two-dimensional
3D	three-dimensional
4D	four-dimensional
$\mathbf{A}$	weight matrix
a	photon shot noise parameter
a_{ij}	weight factor
ART	algebraic reconstruction technique
ASIR	adaptive statistical iterative reconstruction
ASTRA Toolbox	all scale tomographic reconstruction antwerp toolbox
AWGN	additive white Gaussian noise
b	function characterising the filter function, scalar parameter of Gaussian noise
BM3D	block matching and 3D transform domain collaborative filtering
BM3D-SAPCA	block matching and 3D transform domain collaborative filtering with principal component analysis
BM4D	block matching and 4D transform domain collaborative filtering
c	speed of light $[\mathrm{m} \cdot \mathrm{s}^{-1}]$
C_1, C_2	constants
CANDLE	collaborative approach for enhanced denoising under low-light excitation
CBDNet	the convolutional blind denoising network
CCD	charge-coupled device
CGLS	conjugate gradient least square algorithm
CMOS	complementary metaloxide-semiconductor
CMYK	color model containing cyan, magenta, yellow, black
CNN	convolutional neural network
CNR	contrast-to-noise ratio
CT	computed tomography
DCT	discrete cosine transform
DnCNN, DnCNN2	denoising convolutional neural network
DoS	Degree of smoothing
DSC	Dice similarity coefficient
E	energy, expected value
e	Euler's constant
f	the slice, spatial signal, reference image
$\hat{f}$	test image
F	frequency spectrum, binary image
FBP	filtered back-projection
FFDNet	fast and flexible denoising convolutional neural network

FDK	Feldkamp-Davis-Kress method
GPU	graphic processing units
h	Planck's constant
H	filter function
I	intensity exiting the sample, source current, response of the pixel
I_0	entrance intensity
j_0	spectral density
k	number of occurrences
kV	kilovolt
L_1, L_2	norms
M	number of rays in the projection, image height
MRI	magnetic resonance imaging
MSE	the mean square error
n	number of layers, number of bits per pixel
$\mathcal{N}$	Gaussian distribution
N	number of cells, number of detected photons, image width
$\mathbb{N}_0$	the set of natural numbers including 0
N_p	number of projections
NLM3D	non-local means for volumetric data
nlm, NLM	non-local means
NN3D	nonlocality-reinforced convolutional neural networks for image denoising
O	three-dimensional object
p	projection, inverse Fourier transform of a ramp filter
P	probabilistic density function, maximum pixel value
p_o	pedestal parameter
$\mathcal{P}o$	Poisson distribution
px	pixel
P_θ	projection at angle θ
PCA	principal component analysis
PCD	photon-counting detector
PDF	probabilistic density function
PSNR	peak-signal-to- noise ratio
PE	polyethylene
Q_θ	filtered projection
Q-Q plot	quantile-quantile plot
QDC	quantum detection efficiency
$\mathbb{R}$	the set of real numbers
R	correlation coefficient
RAM	random-access memory
ROI	region of interest
ROF	Rudin, Osher, and Fetami problem

RGB	color model containing red, green and blue colors
s	beam's direction
S_θ	Fourier transform of a projection at an angle θ
SA-DCT	shape-adaptive discrete cosine transform
SAFIRE	sinogram-affirmed iterative reconstruction
SART	simultaneous algebraic reconstruction technique
SBROF	Split-Bregman ROF method
|SD|	source-detector distance
SIRT	simultaneous iterative reconstruction technique
SNR	signal-to-noise ratio
|SO|	source-object distance
SSIM	structural similarity index
SURE	Stein's unbiased risk estimator
SURELET	Stein's unbiased risk estimator with linear expansion of threshold
t	polar coordinate, exposure time
TV	total variation
u, v	spatial frequencies
var	variance
X	normal variable
x	spatial coordinate, pixel position
y	spatial coordinate, noise-free signal
z	spatial coordinate, observed signal
Δd	thickness of the material
δ	delta function
η_p	Poissonian noise
η_G	Gaussian noise
θ	angle
λ	wavelength
μ	attenuation coefficient [m^{-1}], mean value
$\mu_o, \mu_f, \mu_{\hat{f}}$	mean value in the region of interest, mean value of a reference image, mean value of a test image
ν	frequency [s^{-1}]
ξ	independent random noise with zero mean and standard deviation of one
σ	standard deviation, signal-dependent part of the noise
σ^2	variance
$\sigma_{f\hat{f}}$	covariance
$\sigma_o, \sigma_f, \sigma_{\hat{f}}$	standard deviation of the region of interest, standard deviation of a reference image, standard deviation of a test image
ω	angular frequency, frequency response

List of Appendices

A Statistical analysis of noise in bright frames with Mo target 79

B Selected parameters for denoising of simulated dataset 82

C Selected parameters for denoising of measured dataset 83

A. Statistical analysis of noise in bright frames with Mo target

The same workflow used for the analysis of copper bright field images has been performed also for the molybdenum target bright field images. Since the molybdenum target operates at a higher voltage – 50 kV, for the same exposure time the mean value of the signal is higher than for the copper target. Therefore, only the exposure times up to 35 seconds will be analyzed. The Q-Q plots and histograms of the noise data will be visualized.

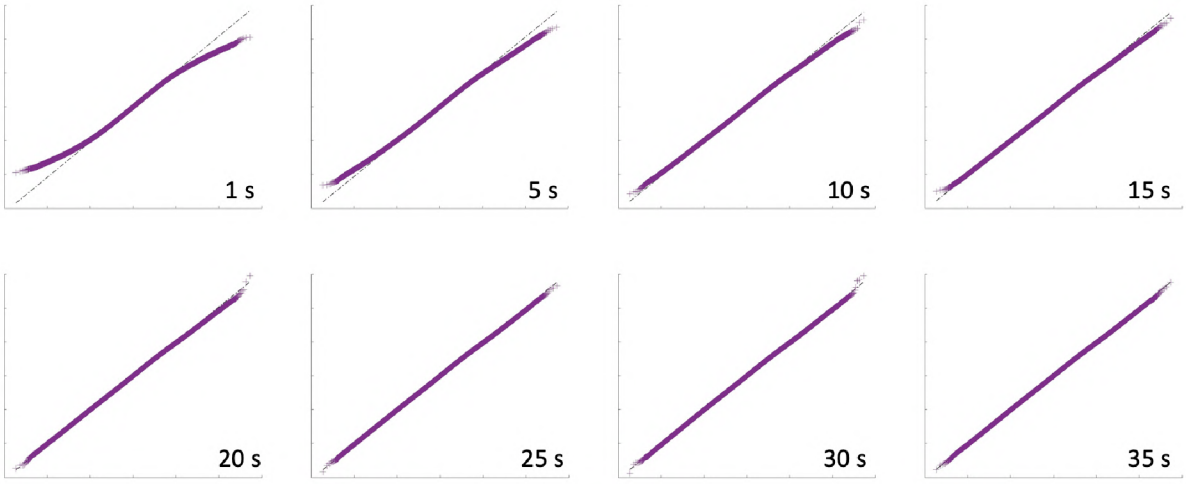

Figure A.1: Q-Q plots of noise data for each exposure time versus normal distribution. If the data is normally distributed, the points are expected to follow a dashed straight line corresponding to the normal distribution.

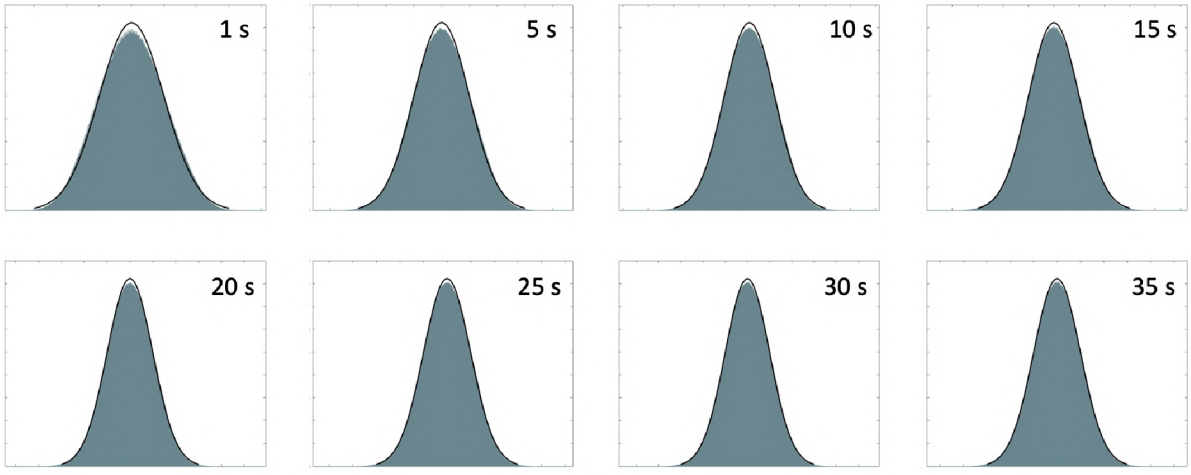

Figure A.2: Histograms for each exposure time and fitted histograms for normal distribution.

It is obvious, that the Q-Q plots in figure A.1 and histograms in figure A.2 look similar to the plots displayed in the section statistical analysis of Cu bright frames – equivalent outcomes can be stated. The largest deviation from the straight line representing a normal distribution in Q-Q plots can be seen for the 1-second and 5-second frames. With higher

exposure time, the deviation gets smaller and the points follow nicely the straight line. This assumption is proved by calculating the MSE of quantiles of normal distribution and the calculated quantiles of observed data. The results are listed in the table A.1. The histograms are displayed with fitted normal distribution – the same conclusions can be formulated as for the Q-Q plots. The higher the exposure, the closer is the experimental histogram to the theoretical one.

Next, the statistical moments of the noise data will be calculated – noise mean value, noise variance, and kurtosis. The outcomes will be listed in the table A.1 with the results of MSE of Q-Q plots and mean values of the signal.

Table A.1: Results from statistical analysis of the bright field images.

	Noise mean value	Noise variance	Kurtosis	MSE of QQ plot	Mean value of the signal
1 s	$-2.057 \cdot 10^{-20}$	$9.962 \cdot 10^{-7}$	2.642	$1.811 \cdot 10^{-3}$	0.086
5 s	$-2.070 \cdot 10^{-20}$	$3.835 \cdot 10^{-6}$	2.779	$6.403 \cdot 10^{-4}$	0.173
10 s	$-4.484 \cdot 10^{-21}$	$7.520 \cdot 10^{-6}$	2.850	$3.678 \cdot 10^{-4}$	0.282
15 s	$3.001 \cdot 10^{-20}$	$1.108 \cdot 10^{-5}$	2.890	$2.520 \cdot 10^{-4}$	0.390
20 s	$1.479 \cdot 10^{-20}$	$1.466 \cdot 10^{-5}$	2.910	$2.205 \cdot 10^{-4}$	0.497
25 s	$-1.080 \cdot 10^{-19}$	$1.829 \cdot 10^{-5}$	2.926	$1.533 \cdot 10^{-4}$	0.602
30 s	$8.364 \cdot 10^{-20}$	$2.188 \cdot 10^{-5}$	2.940	$1.606 \cdot 10^{-4}$	0.709
35 s	$5.100 \cdot 10^{-20}$	$2.538 \cdot 10^{-5}$	2.948	$1.665 \cdot 10^{-4}$	0.814

The results are similar to the ones for Cu frames – the noise mean value can be assumed to be zero, the noise variance is increasing with the exposure time. The kurtosis is reaching the value 3 (the ideal value of normal distribution) and the MSE is decreasing. It is important to note that the mean values of the signal are overall higher than for the Cu frames.

All of the relations described will be shown graphically in plots in figure A.3 to validate the assumptions. With higher exposure time, the deviations from the normal distribution are decreasing. It has been shown in figure A.3 (a), that the variance is dependent on the exposure time – linear dependency. The graph of the relation between the mean value of the signal and the variance will be displayed in figure A.4 – the variance is linearly dependent on the mean value of the signal. The correlation coefficient $R = 1$, which means perfect positive linear dependence, and the relation can be described with formula

$$\sigma^2(y(x)) = 3.36 \cdot 10^{-5} y(x) - 1.95 \cdot 10^{-6}. \tag{A.1}$$

It has been proven, that the conclusions made for Cu bright frames are valid also for the Mo target. In the sets of bright frames in the ranges of analyzed exposure times, the noise can be assumed to be described with *mixed Poisson-Gaussian distribution*.

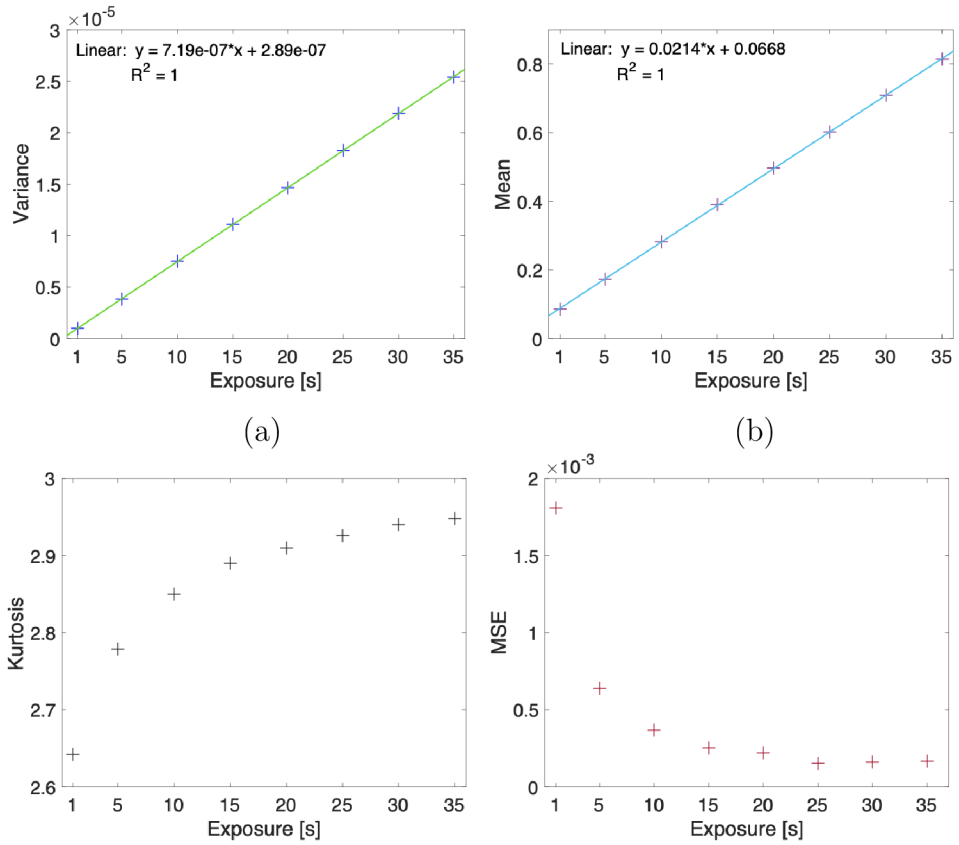

Figure A.3: Results from table A.1 shown graphically. The relations are between (a) exposure time and variance of the noise – linear dependence, (b) exposure time and the mean value of the signal in the bright frames – linear dependence, (c) the kurtosis of the noise data and the exposure time – the deviation from the value 3 corresponding to the normal distribution is decreasing with higher exposure times, (d) mean square error (MSE) of the Q-Q plot and exposure time – the MSE is decreasing with higher exposure time.

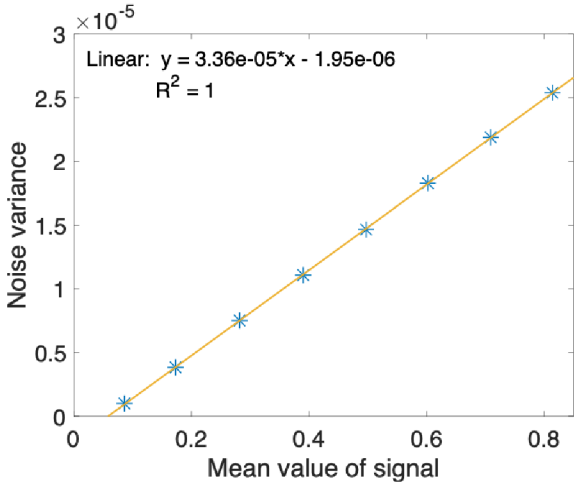

Figure A.4: The relation between the mean signal value of frames and the noise variance – linear dependency.

B. Selected parameters for denoising of simulated dataset

In this section, the parameters chosen for reduction of noise using selected methods are listed in table B.1 for projection domain and in table B.2 for tomogram domain. The value of maximum noise variance/standard deviation is determined from the noise variance matrix, that has been used for generating the noise in the projection domain. In the tomogram domain, the function for noise estimation described in [82] was used. This function estimates the standard deviation of the noise – degree of smoothing (DoS).

Table B.1: Parameters of all tested methods for denoising of simulated dataset in the projection domain.

Method	Parameters
wiener	[5, 3], maximum noise variance
median	[3, 1]
nlm	'DegreeOfSmoothing', maximum noise standard deviation, 'ComparisonWindowSize', 3, 'SearchWindowSize', 25
SBROF	0.6, 10^{-3}
wavelet	2, 'Wavelet', 'rbio5.5', 'DenoisingMethod', 'SURE', 'CycleSpinning', 3
SA-DCT	1.45 × maximum noise standard deviation
BM3D	maximum noise standard deviation, 'refilter'
median 3D	[1, 1, 3]
CANDLE	5, 5, maximum noise standard deviation, 0
NLM3D	3, 2, 0.5 × maximum noise standard deviation
BM4D	'Gauss', 1.1 × maximum noise standard deviation

Table B.2: Parameters of all tested methods for denoising of simulated dataset in the tomogram domain.

Method	Parameters
wiener	[3, 1], 2 × DoS^2
median	[3, 1]
nlm	'DegreeOfSmoothing', 1.5 × DoS, 'ComparisonWindowSize', 5, 'SearchWindowSize', 17
SBROF	4.5, 10^{-3}
wavelet	2, 'Wavelet', 'rbio5.5', 'DenoisingMethod', 'SURE', 'CycleSpinning', 3
SA-DCT	1.5 × DoS
BM3D	2 × DoS, 'refilter'
median 3D	[1, 1, 3]
CANDLE	4, 4, DoS, 0
NLM3D	7, 5, 5 × DoS
BM4D	'Gauss', 2 × DoS

C. Selected parameters for denoising of measured dataset

Table C.1 shows optimal parameters for the selected approaches for all tested real samples. The noise estimation function described in [82] was used for approximation of noise standard deviation. In the table it is expressed as DoS – degree of smoothing.

Table C.1: Parameters of all tested methods for denoising of measured datasets – toothpick sample, PE rod with carbon fibers sample, mouse embryo samle.

	Toothpick
Method	Parameters
BM3D – proj	2 × DoS
BM4D – proj	'Gauss', 5 × DoS
BM4D – tomo	'Gauss', 175 × DoS
nlm – proj	'DegreeOfSmoothing', 1 × DoS, 'ComparisonWindowSize', 3, 'SearchWindowSize', 25
nlm – tomo	'DegreeOfSmoothing', 10 × DoS, 'ComparisonWindowSIze', 3, 'SearchWindowSize', 21
	PE
Method	Parameters
BM3D – proj	1.1 × DoS
BM4D – proj	'Gauss', 1.2 × DoS
BM4D – tomo	'Gauss', 15 × DoS
nlm – proj	'DegreeOfSmoothing', 1 × DoS, 'ComparisonWindowSize', 3, 'SearchWindowSize', 25
nlm – tomo	'DegreeOfSmoothing', 2.2 × DoS, 'ComparisonWindowSIze', 7, 'SearchWindowSize', 29
	Mouse embryo
Method	Parameters
BM3D – proj	1.1 × DoS
BM4D – proj	'Gauss', 1.2 × DoS
BM4D – tomo	'Gauss', 20 × DoS
nlm – proj	'DegreeOfSmoothing', 0.75 × DoS, 'ComparisonWindowSize', 3, 'SearchWindowSize', 25
nlm – tomo	'DegreeOfSmoothing', 2.5 × DoS, 'ComparisonWindowSIze', 5, 'SearchWindowSize', 29